Improved assembly reduction by selection of component eigenmodes using frequency-based substructuring

Kessels, B.M.

Award date:
2020

Improved assembly reduction by selection of component eigenmodes using frequency-based substructuring

Master Thesis

Saturday 7th December, 2019

Author:

B.M. Kessels — Eindhoven University of Technology, Department of Mechanical Engineering, Dynamics & Control
B.M.Kessels@student.tue.nl

Supervisors/committee members:

prof.dr.ir. N. van de Wouw — Eindhoven University of Technology, Department of Mechanical Engineering, Dynamics & Control

dr.ir. R.H.B. Fey — Eindhoven University of Technology, Department of Mechanical Engineering, Dynamics & Control

ir. A.M. Steenhoek — ASML, BM DE MSD D System Dynamics DUV

ir. M.L.J. Verhees — ASML, BM DE MSD E System Dynamics EUV

Additional committee members:

dr.ir. B. Besselink — University of Groningen, Bernoulli Institute for Mathematics, Computer Science and Artificial Intelligence

dr.ir. L. Iapichino — Eindhoven University of Technology, Mathematics and Computer Science, Centre for Analysis, Scientific Computing, and Applications W&I

TUe document number: DC 2020.002

ASML document number: D000807717

Abstract

To predict the dynamical behavior of complex systems, such as the waferscanners built and developed by ASML, finite element modeling is used. Due to the increasing complexity of these systems, the size of their models has been increasing as well. Therefore, there is a demand for the reduction of the number of degrees of freedom of such models. In the dynamic substructuring context, this reduction is performed on component level. Specifically, component mode synthesis techniques are employed which use a truncation of the component eigenmodes to reduce the size of component models. Selecting which eigenmodes should be retained has always been done by using a simple selection criterion. In this MSc. thesis, an improved procedure for selecting the retained component eigenmodes is proposed that aims at finding improved reduced component models that induce more accurate and/or efficient reduced assembly models. Additionally, such a method has the potential to provide valuable insight in the relevance of specific component modes, which can be used to enhance the performance of the full system.

To evaluate the relevance of individual component modes, the propagation of the contributions of these modes through the assembled system is investigated. In this research, three frequency-based methods are explored to achieve this. The first method uses a feedback representation of a (two-component) system to determine a bound on the assembly error by examining the propagation of bounds on the errors of transfer functions of its components. In order to use this bound, the small gain condition needs to hold. Since (among other reasons) it proves difficult to satisfy this condition for mechanical (structural dynamics) systems, this method suffers from a lack of applicability. The second method divides the assembly error in specific contributions. These 'error contributors' show the relative importance of interface transfer errors. For an efficient component mode selection procedure, this method is however computationally too demanding. Therefore, a third method is investigated which determines a first-order Taylor approximation of the assembly error. This method uses the sensitivity of the assembly receptance with respect to the receptances of the uncoupled components in combination with the component reduction errors. For the efficient estimation of these component errors, spectral decomposition is exploited.

The above mentioned Taylor-approximation is used to analyze the assembly errors when component modes are omitted from the component reduction bases. Using a norm-based measure for the approximated reduction errors caused by truncating individual component modes, insight in the relevance of each individual component mode is obtained. By ranking the error measures, an improved selection of component eigenmodes to be used in the reduction bases is determined.

Finally, the component mode selection method is illustrated by an application to an academic example. For this example, it is shown that the proposed selection method enables to decrease the reduction error of transfers (between specific points of interest in a specified frequency range)

with respect to the error obtained by using the conventional eigenmode selection approach. Because of this fact, the established selection procedure enables the user to find more accurate and/or efficient reduced assembly models. Furthermore, insight in the importance of individual component modes for the assembly is realized.

Acknowledgements

The thesis presented to you here, is written for my Master of Science graduation project. I was fortunate enough that I was given the opportunity to do this project at ASML. Writing my thesis here provided me with a pleasant and inspiring working environment, as well as friendly and competent 'colleagues'. I would therefore like to thank Rob Fey, who proposed and introduced me as a graduation student to this company. Also, much appreciation goes out to ASML, for allocating the time, space and resources required for having me around.

I would also like to thank prof. Nathan van de Wouw, who gave me various ideas for different directions I could take my project in. Also, when I encountered difficulties, he was not hesitant to answer my questions clearly such that I could continue my research without too much delay, which is greatly appreciated.

Furthermore, I would like to express my appreciation for the supervision and enthusiasm towards my project of my supervisors at ASML, Alexander Steenhoek and Thijs Verhees. I benefited greatly from our weekly meetings, which kept me on track, gave me new ideas to tackle problems in ways I did not think of before, and safeguarding that the practical application would not get lost in a maze of complex and impractical theories. In particular, I would like to thank Alexander for asking critical open-ended questions which forced me to think about the broader context of the subject of my thesis and how my project would contribute to this field. Especially in the project-forming months, this was very helpful. Furthermore, the very critical comments made by Thijs made sure that the ideas and theories that I had in mind were evaluated thoroughly before and during implementation, which is greatly appreciated. Also, their feedback on this report has been very valuable.

Additionally, I am thankful for the discussions I had with my fellow graduating student at ASML, Jari van Steen. Since Jari and I worked on similar (but yet different) projects, we were able to provide enlightening points of view on each others subjects, which, for me, helped moving the project along and finding the source and solution to problems much faster.

I am also very grateful for the continuous support and interest in the process of writing this MSc. thesis of my parents and brother. And finally, of course, I thank Kiki for her lasting confidence in me, being there for me, her understanding, and providing me with (sometimes much-needed) distraction from the project.

Contents

List of Figures

List of Tables

Nomenclature

Symbols

Below a summary of the general meaning of the symbols used in this report is given. Deviations from these symbol conventions are mentioned in-text:

Greek Symbols:

γ	Bound on transfer function (matrix)
$\boldsymbol{\delta}$	Difference operator
ε	Bound on error of transfer function matrix)
ϵ	Frequency-dependent error measure
ξ	Modal damping factor
$\boldsymbol{\Xi}$	Modal damping factor matrix
ρ	Density
σ	Singular value
Σ	Summation
$\boldsymbol{\Sigma}$	(Sub)system
$\boldsymbol{\phi}$	Eigenvector, vibration mode shape
$\boldsymbol{\Phi}$	Set of eigenvectors, Set of vibration mode shapes
φ	Rotation
ϕ	Error measure
$\boldsymbol{\psi}$	Static deformation shape
$\boldsymbol{\Psi}$	Set of static deformation shapes
ω	Angular (eigen)frequency
$\boldsymbol{\Omega}$	Angular eigenfrequency matrix

Roman Symbols:

A	Area
$\boldsymbol{B}$	Signed boolean mapping matrix
$\boldsymbol{D}$	Structural damping matrix
$\mathcal{D}$	Set of deleted component modes
E	Young's modulus
$\boldsymbol{E}$	Transfer function error matrix
$\boldsymbol{f}$	Vector containing force(s)/moment(s) (time domain)
F	Force (scalar value)
$\boldsymbol{F}$	Vector containing force(s)/moment(s) (frequency domain)
$\boldsymbol{H}$	Transfer function matrix

I	Area moment of inertia
$\boldsymbol{I}$	Identity matrix
j	Imaginary unit
k	Iteration index
$\boldsymbol{K}$	Stiffness matrix
$\mathcal{K}$	Set of kept component modes
l	Length/iteration index
$\boldsymbol{L}$	Boolean localization matrix
M	Moment
$\boldsymbol{M}$	Mass matrix
$\mathcal{M}$	Set of all component modes
n	Number/amount of [some variable]
$\boldsymbol{P}$	Matrix derivative (with respect to an element of the matrix)
$\boldsymbol{q}$	Set of generalized coordinates
$\boldsymbol{S}$	Scaling matrix
t	Time
$\boldsymbol{T}$	Reduction matrix
u	Displacement
$\boldsymbol{u}$	Input for system/Vector containing displacement(s)/rotation(s) (time domain)
$\boldsymbol{U}$	Vector containing displacement(s)/rotation(s) (frequency domain)
$\boldsymbol{v}$	Interface variable
$\boldsymbol{w}$	Interface variable
$\boldsymbol{y}$	Output
$\boldsymbol{Y}$	Receptance matrix
$\boldsymbol{Z}$	Dynamic stiffness matrix

General meaning of subscripts, superscripts, and accents:

$_b$	Boundary
$_f$	Interface
$_i$	Internal
$_k$	Mode number
$_r$	Retained
$_\gamma$	Unique interface degrees of freedom of assembly
$_{(assy)}$	Belonging to the assembled system
$_{(c)}$	Belonging to substructure c
$_{(e)}$	Belonging to an element
$\langle\hat{\cdot}\rangle$	A reduced variable
$\langle\bar{\cdot}\rangle$	A propagated variable
$\langle\tilde{\cdot}\rangle$	Scaled variable
$\langle\cdot\rangle^*$	Complex conjugate

Notation conventions

Here, some important notation conventions will be given. Deviations from these conventions are mentioned in-text:

- Boldface variables can denote either vectors or matrices, where vectors are given by lower case symbols and matrices by uppercase symbols. Scalar values are given by plain symbols (non-boldface) and can either be written in upper or lower case. Two exceptions on this convention are the vector containing displacements/rotations and the vector forces/rotation in the frequency domain ($\boldsymbol{U}$ and $\boldsymbol{F}$, respectively).

- Block diagonal matrices are denoted by the notation $\mathrm{diag}\,(\cdot,\cdot)$, e.g.,

$$\mathrm{diag}\,(\boldsymbol{X},\boldsymbol{Y}) = \begin{bmatrix} \boldsymbol{X} & \boldsymbol{0} \\ \boldsymbol{0} & \boldsymbol{Y} \end{bmatrix}.$$

- Stacked vectors are indicated by $\mathrm{col}\,(\cdot;\cdot)$, for instance:

$$\mathrm{col}\,(\boldsymbol{x};\boldsymbol{y}) = \begin{bmatrix} \boldsymbol{x} \\ \boldsymbol{y} \end{bmatrix}.$$

- Vector and matrix norm are indicated by $\|\cdot\|_{\langle\cdot\rangle}$, where the subscript denotes which type of norm is used.

- A transfer function matrix is given by $\boldsymbol{H}_{kl}^{(c)}$, where c denotes the associated component, the subscript indicates that the input of the transfer is signal $\boldsymbol{l}$, and the output is signal $\boldsymbol{k}$.

- Signals are sometimes given as a function of certain variables. These functions are, for example, given by $G_k^{(c)}(\boldsymbol{l})$, where $\boldsymbol{k}$ denotes the output of this function, and $\boldsymbol{l}$ is the input of this function.

- The variable γ represents a bound on a transfer function. More specifically, it gives the H_∞-norm of a specific transfer function (matrix),

$$\gamma = \|\boldsymbol{H}(\omega)\|_\infty.$$

  The variable ε is a bound on the difference between an unreduced and reduced transfer function (matrix),

$$\varepsilon = \|\boldsymbol{H}(\omega) - \hat{\boldsymbol{H}}(\omega)\|_\infty.$$

- To select elements of a matrix $\boldsymbol{A}$, the notation $\boldsymbol{A}[k,l]$ is used, where k is the row-index and l the column-index.

- The maximal singular value of a matrix $\boldsymbol{A}$ is given by $\sigma_{max}(\boldsymbol{A})$.

- A summation of variables x_k with indexes k going from 1 up until n is given by

$$\sum_{k=1}^{n} x_k.$$

  The summation of all variables x_k with indexes k in a specific set $\mathcal{S}$ is given by

$$\sum_{k\in\mathcal{S}} x_k.$$

- If a variable $\boldsymbol{z}$ is or should be some function of specific variables, this is denoted by

$$\boldsymbol{z} = f(\cdot,\cdot).$$

- The time derivative of a time-dependent variable $\boldsymbol{x}$ with respect to the time t is given by

$$\dot{\boldsymbol{x}} = \frac{d\boldsymbol{x}}{dt}.$$

  Likewise, the second derivative is formulated by

$$\ddot{\boldsymbol{x}} = \frac{d^2\boldsymbol{x}}{dt^2}.$$

Abbreviations

A few abbreviations that are used throughout this report are:

CB	Craig-Bampton	FRF	Frequency response function
CMS	Component mode synthesis	FROI	Frequency range of interest
CVM	Condensed vibration mode	HH	Hintz-Herting
DOF	Degree of freedom	LM FBS	Lagrange multiplier frequency-based substructuring
DS	Dynamic substructuring	MT	Modal truncation
EOM	Equation of motion	POI	Point of interest

Sometimes, in the text a lowercase 's' will be affixed to an abbreviation. This indicates the plural form of the abbreviation, e.g., DOFs denotes degrees of freedom.

Chapter 1

Introduction

In the process of designing high-tech machinery, it often required to predict both static and dynamic behavior as a consequence of loads acting on the system from within or from the outside world. The branch of engineering which is concerned with modeling the dynamics of (complex) structures is called structural dynamics. Due to the increasing size and complexity of models, a dynamic analysis can be very demanding from a computational point of view. Therefore, dynamical behavior is often not modeled in full detail, but rather described by smaller representative models.

At ASML, systems are developed which are used for the production of semiconducter-based microchips (for the interested reader an introduction to semiconductor physics is given by Neamen [25] and Hepburn [14]). A side view of such a machine, which is called a waferscanner, is shown in Figure 1.1. Since models of these systems are very complex, they are divided in more manageable subsystems (or components), which can be modeled, reduced, and analyzed separately. Afterwards, these subsystem models are coupled to obtain the dynamical behavior of the full system. This approach of modeling, reducing, analyzing, and assembling individual components is referred to as dynamic substructuring (DS). This procedure offers significant advantages in engineering practice, since it allows different design teams to work on different parts of the system at the same time. It also enables a user to optimize the design of a part of a system, without having to run extensive computations for the entire system.

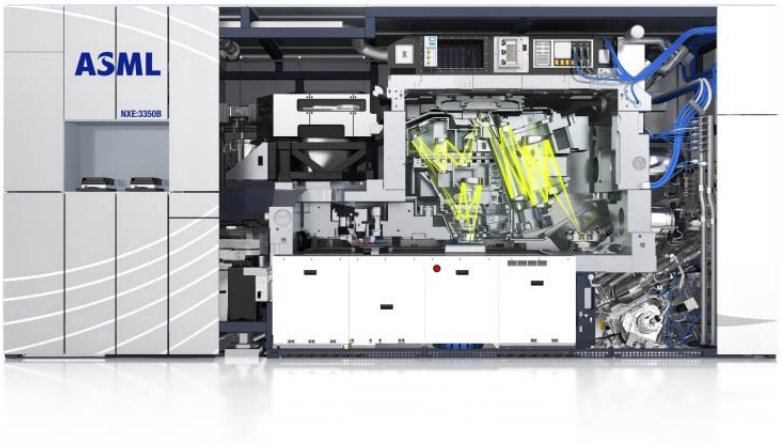

Figure 1.1: *Sideview of a TWINSCAN NXE EUV waferscanner system of ASML.*

Although dividing the system in components already makes the dynamic modeling of complex systems more manageable, it is often still computationally expensive to use a detailed finite element model (FEM) of an uncoupled subsystem. Therefore, model reduction is applied to the uncoupled component models, which drastically lowers their associated number of degrees of freedom (DOFs). The goal of this research is to find techniques that optimize this component reduction such that optimal accuracy (in the sense of low reduction errors) of the approximated (dynamic) behavior of the assembled system is achieved.

1.1 State-of-the-art in dynamic substructuring

As explained previously, component model order reduction is required to obtain reduced component models which are assembled to obtain a reduced assembly model. This reduction can be achieved by using various techniques. For example, moment matching [3] can reduce models with high accuracy. However, since this method is applied in the frequency domain, much information about the physical interpretation of the model is lost. Furthermore, preservation of stability properties of the model is not guarenteed by this method [3]. Other common reduction methods are balanced truncation [3] and optimal Hankel norm approximation [12]. An advantage of both methods is that they provide an a priori bound on the reduction error, which can be very useful to assess the reduction quality in an early stage. An important disadvantage is however that these methods use a first-order system description, which means that physical insight is lost.

Since component mode synthesis (CMS) does not suffer from the above mentioned disadvantages, this thesis uses CMS techniques to reduce the component system matrices as used in the second-order equation of motion of a component. Another motivation for the choice to use CMS techniques is that this methodology is already being used in the system dynamics group at ASML. In contrast to the balanced truncation and Hankel norm approximation methods, component mode synthesis does however not provide an a priori bound on the reduction error.

In Figure 1.2, an application of the CMS technique to a simple cantilever beam is illustrated (conform the DS methodology). As shown, the first step in this procedure is to divide the unreduced system in components. Then, mode shapes are determined which summarize specific dynamic behavior of all DOFs in a component. Although multiple shape types can be used (e.g., pre-defined polynomial series), in this thesis, the eigenmodes resulting from an eigenvalue problem are used. Since a small selection of these eigenmodes often suffices to approximate the dynamical behavior with sufficient accuracy, a subset of all component modes is employed to define a reduction basis for the component. Besides eigenmodes, some additional modes are also present in CMS to allow the components to be coupled. To determine these modes, the unreduced component models are used. In the fourth step, the reduction basis is applied to the unreduced component to generate a reduced component model. For the final step, the reduced components are assembled such that a reduced model of the complete assembly is obtained.

To obtain reduced component models which optimize the reduction quality of the reduced assembly, this research focuses on the selection of dynamic component modes for the component reduction bases (the third step in Figure 1.2). Currently, this selection is typically solely based on the eigenfrequencies associated to the eigenmodes [9, 31]. This is acceptable as, due to the high-frequency roll-off of receptances, which is typical for the receptance of mechanical systems,

dynamical behavior is often only relevant up to some user-defined frequency. Moreover, since disturbances are, in practice, often present at high-frequencies, an unreduced model does not properly represent the actual system at high-frequencies. Consequently, there is no point in approximating the unreduced model accurately in this frequency range. Current practice for the reduction of a (sub)system is therefore to only ensure accuracy up to some specific frequency, which is achieved by truncating all component eigenmodes with eigenfrequencies above this frequency. Using components which are reduced by applying this approach does however not guarantee that the assembly of the reduced components will be accurate in this frequency range as well. Therefore, as a rule of thumb, the cutoff frequency for a reduced component should be approximately 2.5 times higher than the maximum frequency range of interest.

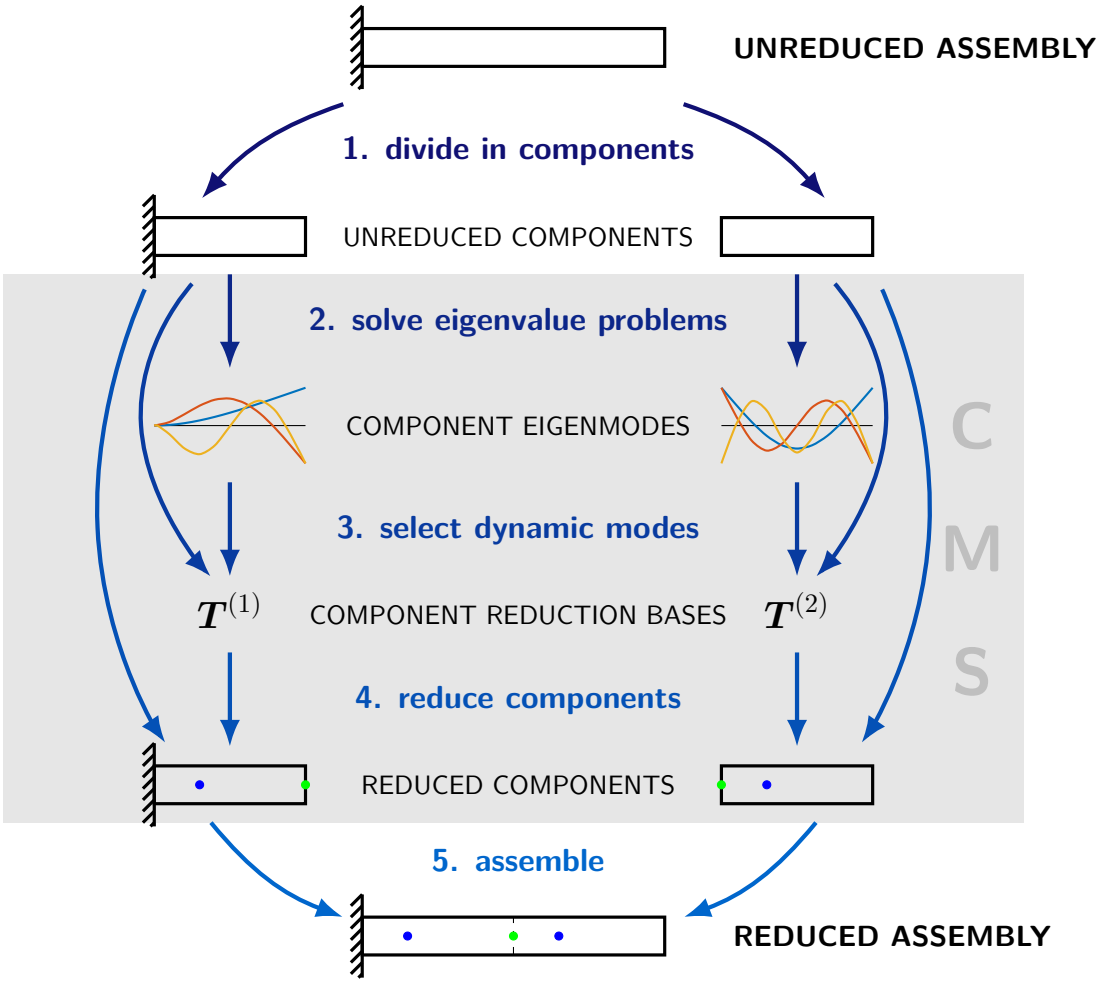

Figure 1.2: *Schematic representation of the dynamic substructuring procedure, where the intermediate steps (blue text) and results (black text) are indicated. The shaded area shows the part of the DS procedure referred to as CMS. The curved arrows coming from the unreduced components indicate that the unreduced component models are, besides step 2, also needed in steps 3 and 4.*

It is however not expected that retaining component modes based on their frequency is optimal. For example, if the assembly behavior is to be approximated accurately at specific points of interest (POIs), located in a relatively small part of the system, component modes inducing (local) assembly behavior at other parts of the system are not relevant. By truncating these irrelevant modes, other (more relevant) modes can be retained instead, or the reduction basis can be made smaller. This thesis therefore aims at finding a technique which is able to (efficiently) rank component modes based on their relevance to the assembly, such that an 'optimal' set of

retained component modes can be defined. An advantage of an optimal set of retained eigenmodes is that more accurate and/or more efficient reduced assembly models can be obtained. Furthermore, being able to predict which component modes are relevant can provide insight in which component modes cause specific (unwanted) behavior in an assembly.

One of the challenges to find an 'optimal' set of retained component modes is that the influence of individual component modes on an assembly of components has to be assessed. Preferably, this is done efficiently such that computation times are relatively low. Furthermore, the reduction quality of an assembly (related to the dynamic behavior at specific points of interest) has to be quantified such that various reduced assemblies can be compared in a fair and consistent manner. Once the influence of individual component modes is determined, the relevance of each individual mode to the assembly has to be determined. Finally, the information of the relevance of each eigenmode should be used to formulate a procedure to select which (dynamic) component eigenmodes should be used in the (component) reduction bases.

1.2 Research goals and approach

As mentioned previously, the main goal of this research is to find improved component reduction bases such that the accuracy of the reduced assembly model is optimal. To achieve this goal, the following objectives, based on the challenges identified in the previous section, have been defined:

- **Investigate different error propagation techniques:**
  To assess the relevance of component modes, propagation techniques which assess how component errors (induced by truncating specific component modes) propagate through an assembly are investigated. Since it is beneficial to have the potential to use the propagation methods in combination with experimentally obtained component models (besides the component models which need to be improved), this propagation is performed in the frequency domain. Additionally, this allows gathering insight in the frequency-dependent behavior of errors.
- **Define a measure for the reduction quality:**
  Since the error of a reduced system with respect to the unreduced system gives a measure for the quality of the reduced model, these reduction errors will be used to quantify the reduction quality of a reduced system. Furthermore, techniques are used which condense multi-dimensional (error) signals to scalar error measures which can easily be compared and ranked.
- **Find a procedure for the selection of retained component eigenmodes:**
  To evaluate the relevance of specific component modes to the assembly, assembly reduction errors induced by truncating (sets of) component eigenmodes are determined. Ranking (sets of) eigenmodes is then achieved by comparing the corresponding error measures. To select an optimal set of retained component eigenmodes, the information provided by ranking the assembly reduction error measures is used.

1.3 Thesis outline

The outline of this thesis is elaborated per chapter below:

- Chapter 2 is set out to provide the reader with the relevant background theory required for properly understanding this thesis. Here, the focus lies on the assembly of components and component reduction methods. Furthermore, this chapter introduces a demonstrator which is used throughout this thesis to illustrate the implementation of various techniques.

- Chapter 3 introduces a technique to assess the propagation of component errors through an assembly by looking at bounds on both transfer functions and transfer errors. In this chapter, a feedback framework will be adopted to efficiently find a bound on the assembly error for a system consisting of two reduced components. Determining such bounds for various reduced assemblies, which are obtained by using components reduced by retaining different (sets of) component modes, could provide insight in which retained modes result in the most accurate approximations of the assembly behavior. Finally, the small gain condition (stemming from control theory) is discussed, since this condition needs to hold in order to be able to use the expression for the bound on the assembly error.

- Chapter 4 investigates two new approaches which are used to determine the propagation of component errors. Both methods are based on the Lagrange multiplier frequency-based substructuring (LM FBS) technique [16]. The first approach will attempt to write the assembly reduction error in terms of contributions of individual component modes. The second approach is based on the sensitivity of an assembly with respect to its components and gives an approximation of the assembly error. In contrast to the error bound propagation method (see Chapter 3) which used a feedback representation of a system, both methods presented in this chapter can be easily applied on systems consisting of more than two components. Finally, both approaches utilize an efficient expression to estimate the component reduction error by using information on which eigenmodes are deleted from the component reduction bases. This estimation of the component reduction error will be discussed in Chapter 4 as well.

- Chapter 5 uses the sensitivity-based propagation method introduced in Chapter 4 and defines a measure for the reduction error of the assembly. This measure is used to rank multiple component modes and subsequently select the eigenmodes which are, for a specific user-defined frequency range of interest and points of interest, most relevant for the assembly. Finally, the selection procedure proposed in this thesis is applied to the demonstrator system and several results hereof are presented and discussed.

- Chapter 6 gives a list of the conclusions based on the work performed for this research. Furthermore, this chapter lists multiple topics which have not yet been discussed in this thesis and are therefore recommended to research in future work.

Detailed information about the demonstrator beam, derivations and proofs, and some mathematical background for notions used in this thesis can be found in Appendices A, B, and C, respectively. Finally, a declaration of the code of conduct is provided in Appendix D.

Chapter 2

Theoretical background

This chapter provides the theoretical background of several key aspects used throughout this thesis. Since the research conducted here is confined to numerical modeling, the topics and methods introduced in this chapter are of a numerical nature. Some of these methods can however be applied in an experimental context as well. For the discussion of these topics, it is assumed that the reader has some basic knowledge of finite element (FE) modeling as this forms an important backbone of this research.

The first topic which is discussed is the dynamic substructuring (DS) method, which is used to divide a system in multiple uncoupled subsystems. Section 2.2 introduces some theory on how to couple these subsystems such that an assembled system is obtained. Afterwards, techniques for the reduction of the models of the subsystems is discussed. Finally, a standard reduction procedure is illustrated in a DS context. The (reduced) model used for this illustration (Section 2.4) serves as a benchmark for the other chapters of this thesis.

2.1 Dynamic substructuring

As already discussed in the introduction, dynamic substructuring is a term used for methods that determine dynamical assembly behavior by modeling, reducing, and coupling the dynamical behavior at substructure level. Some advantages of these techniques are listed below:

- Information of substructures obtained in different domains can be combined. For example, experimentally obtained dynamical behavior of components can be combined with numerical models.
- Complex systems can be modeled, analyzed, reduced, and optimized at substructure level, simplifying the complexity of large assemblies.
- Substructures can be designed and modeled in different development teams, such that these teams do not require detailed knowledge regarding the models of other teams.
- Numerically solving multiple small components is less computationally intensive than solving a single large system.

Within the dynamic substructuring framework, multiple methods belonging to different classes exist: impulse-based dynamic substructuring [27], frequency-based dynamic substructuring (FBS) [8], and physical domain-related substructuring [17]. The former class (impulse-based) is not used that much in industry yet, since it is relatively new. Because of this fact, and the fact

that it currently often goes paired with relatively high computational costs [31], this class is not discussed in more detail in this research. Two methods belonging to the second class (FBS) are discussed briefly in Sections 2.2.3 and 2.2.4. This discussion is however restricted to assembly techniques. For the reduction of components, component mode synthesis (CMS), which is a method from the physical domain-related substructuring class, is used in this thesis. A reason for this is that the eigenmodes, used in this method, give a lot of valuable insight to engineers. Furthermore, this technique is popular within the ASML dynamic substructuring group (due to its implementation in software and the insight it provides). In Section 2.3, the component mode synthesis method and a more general component reduction method (modal truncation) are explained in more detail.

2.2 Coupling methods

In the previous section, it was explained that in the DS framework large complex systems are divided in different components. Since, in the end, information about the behavior of the full system (or assembly) is required, this section discusses how component models can be coupled. This process is referred to as "assembly" and uses information on the interfaces where different components are attached to each other. Although the assembly techniques shown in this section use unreduced component models, these can also be applied to reduced component models.

First, two conditions which are required for the assembly of substructures are discussed in Section 2.2.1. Then, a short discussion on coupling components in the physical domain is given. Afterwards, in Sections 2.2.3 and 2.2.4, two frequency-based assembly techniques are discussed, of which a comparison of these techniques is presented in Section 2.2.5.

2.2.1 Coupling conditions

In order to rigidly connect two components, the nodes at the interfaces of both components should have the same displacement and rotations. This condition is called the compatibility condition and is written as

$$\boldsymbol{B}_f \boldsymbol{u}_b^{(assy)} = \boldsymbol{0}. \tag{2.1}$$

In this equation, $\boldsymbol{u}_b^{(assy)}$ is the boundary degree of freedom related partition of $\boldsymbol{u}^{(assy)}$. Here, $\boldsymbol{u}^{(assy)}$ represents the collection of all degrees of freedom (DOFs) of the uncoupled components and is defined as

$$\boldsymbol{u}^{(assy)} = \mathrm{col}\left(\underbrace{\begin{bmatrix} \boldsymbol{u}_i^{(1)} \\ \boldsymbol{u}_b^{(1)} \end{bmatrix}}_{\boldsymbol{u}^{(1)}}; \ldots; \underbrace{\begin{bmatrix} \boldsymbol{u}_i^{(n_c)} \\ \boldsymbol{u}_b^{(n_c)} \end{bmatrix}}_{\boldsymbol{u}^{(n_c)}} \right), \tag{2.2}$$

where n_c denotes the number of components in an assembly. As is shown in Equation (2.2), $\boldsymbol{u}^{(assy)}$ consists of the DOFs of the components ($\boldsymbol{u}^{(c)},\ c \in \{1, 2, \ldots, n_c\}$), which are partitioned in internal and boundary parts (indicated by $_i$ and $_b$, respectively) and subsequently stacked in a column. Here, the boundary DOFs represent the combination of interface and so-called retained degrees of freedom in a component. These retained degrees of freedom typically represent the DOFs of specific points of interest. The remaining DOFs (except for DOFs constrained as a result of boundary conditions) are called internal DOFs and are typically the degrees of freedom which are reduced (when CMS methods are used for the component reduction). In Figure 2.1, an example of the definition of the various node types for a two-component cantilever beam

is given. Here, the a force $\boldsymbol{F}$ and displacement $\boldsymbol{U}$ are located at points of interest (indicated by blue dots) and the interface nodes are defined at the edges of both components which are connected in the assembled system.

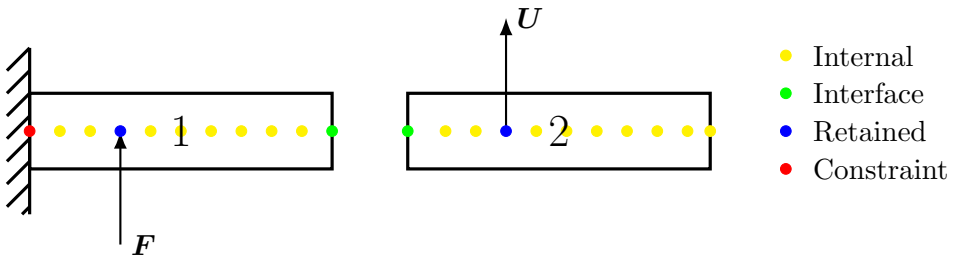

Figure 2.1: *Example of the definition of node types for a schematic representation of a two-component cantilever beam with input at component 1 and output at component 2. The nodes of each component are indicated by color-coded dots.*

Furthermore, in Equation (2.1), $\boldsymbol{B}_f \in \mathbb{Z}^{n_f^{(assy)} \times n_{sum,b}}$ represents a signed boolean matrix which enforces the compatibility condition. With respect to the size of this matrix, $n_f^{(assy)}$ denotes the number of unique interface degrees of freedom in the assembly and $n_{sum,b}$ represents the lumped sum of the total number of boundary DOFs in each component. More information about the exact definition of this matrix is given by de Klerk [17].

The second condition which needs to hold in order to rigidly couple components is related to the forces at the interfaces. The forces acting on the interfaces of two connected components should namely be equal in size and opposite in direction (third law of Newton). This so-called force equilibrium condition is formally defined as

$$\boldsymbol{L}_f^T \boldsymbol{g}_b^{(assy)} = \boldsymbol{0}, \tag{2.3}$$

where $\boldsymbol{L}_b \in \mathbb{Z}^{n_{sum,b} \times n_\gamma}$ is a boolean matrix which is chosen such that the interface forces $\boldsymbol{g}_b^{(assy)}$ satisfy the force equilibrium condition, and n_γ represents the total number of unique boundary DOFs in the assembly. The construction of $\boldsymbol{L}_b$ is explained in detail by de Klerk et al. [17]. Furthermore, $\boldsymbol{L}_b$ spans the nullspace of $\boldsymbol{B}_f$:

$$\boldsymbol{B}_f \boldsymbol{L}_b = \boldsymbol{0}. \tag{2.4}$$

In Equation (2.3), $\boldsymbol{g}_b^{(assy)}$ represents a vector with the interface forces in the assembly, which is obtained by stacking the interface forces of the uncoupled components which are denoted by $\boldsymbol{g}_b^{(c)}$ (similar to Equation (2.2)). Note that, since $\boldsymbol{g}_b^{(assy)}$ represents the interface forces acting on all boundary DOFs (thus interface and retained DOFs), in theory, $\boldsymbol{g}_b^{(assy)}$ could also apply forces at retained DOFs. In practice, however, the retained DOF related entries of $\boldsymbol{g}_b^{(assy)}$ are set to 0. Similarly the interface force vector which is defined for all degrees of freedom (boundary and internal), $\boldsymbol{g}^{(assy)}$, is zero at all non-interface DOFs.

By using these coupling conditions, it is assumed that the components are rigidly connected to each other. Furthermore, the nodes at matching interfaces of different components are assumed to be coincident and share the same set of degrees of freedom, such that the compatibility condition is easy to satisfy (this is called conforming interfaces). Although there are techniques which deal with non-rigid and non-conforming interfaces, these will not be discussed here since these are outside of the scope of this research. The interested reader is therefore referred to the work of Voormeren [31] and Rixen [26], respectively.

2.2.2 Assembly in the physical domain

As is common in structural dynamics, the equation of motion (EOM) of an undamped linear time-invariant component c is given by

$$\boldsymbol{M}^{(c)}\ddot{\boldsymbol{u}}^{(c)} + \boldsymbol{D}^{(c)}\dot{\boldsymbol{u}}^{(c)} + \boldsymbol{K}^{(c)}\boldsymbol{u}^{(c)} = \boldsymbol{f}^{(c)} + \boldsymbol{g}^{(c)}, \tag{2.5}$$

where $\boldsymbol{M}^{(c)} \in \mathbb{R}^{n_m^{(c)} \times n_m^{(c)}}$ is the mass matrix, $\boldsymbol{D}^{(c)} \in \mathbb{R}^{n_m^{(c)} \times n_m^{(c)}}$ is the structural damping matrix, and $\boldsymbol{K}^{(c)} \in \mathbb{R}^{n_m^{(c)} \times n_m^{(c)}}$ is the stiffness matrix. Furthermore, $\boldsymbol{f}^{(c)}$ is a vector representing external force(s) which are applied on the substructure and $\boldsymbol{g}^{(c)}$ represents constraint forces induced by the coupling with other components. Because of the general multi-input multi-output (MIMO) approach adopted in this research, it should be mentioned that whenever forces or displacements are mentioned, a combination of forces and moments, or displacements and rotations is actually meant. Likewise, 'displacement' vectors can contain both displacements and rotations, and 'force' vectors can contain both forces and moments. This is explained in more detail in Appendix A.1.

If the mass, damping, and stiffness matrices (also referred to as the system matrices) of all components in an assembly are known, the system matrices of the assembled system are obtained by exploiting the aforementioned compatibility and force equilibrium conditions. For this, if the coupling is performed in the physical domain, first, the component system matrices are partitioned in internal and boundary DOF related parts:

$$\begin{bmatrix} \boldsymbol{M}_{ii}^{(c)} & \boldsymbol{M}_{ib}^{(c)} \\ \boldsymbol{M}_{bi}^{(c)} & \boldsymbol{M}_{bb}^{(c)} \end{bmatrix} \begin{bmatrix} \ddot{\boldsymbol{u}}_i^{(c)} \\ \ddot{\boldsymbol{u}}_b^{(c)} \end{bmatrix} + \begin{bmatrix} \boldsymbol{D}_{ii}^{(c)} & \boldsymbol{D}_{ib}^{(c)} \\ \boldsymbol{D}_{bi}^{(c)} & \boldsymbol{D}_{bb}^{(c)} \end{bmatrix} \begin{bmatrix} \dot{\boldsymbol{u}}_i^{(c)} \\ \dot{\boldsymbol{u}}_b^{(c)} \end{bmatrix} + \begin{bmatrix} \boldsymbol{K}_{ii}^{(c)} & \boldsymbol{K}_{ib}^{(c)} \\ \boldsymbol{K}_{bi}^{(c)} & \boldsymbol{K}_{bb}^{(c)} \end{bmatrix} \begin{bmatrix} \boldsymbol{u}_i^{(c)} \\ \boldsymbol{u}_b^{(c)} \end{bmatrix} = \begin{bmatrix} \boldsymbol{0} \\ \boldsymbol{f}_b^{(c)} \end{bmatrix} + \begin{bmatrix} \boldsymbol{0} \\ \boldsymbol{g}_b^{(c)} \end{bmatrix}. \tag{2.6}$$

Note that, since $\boldsymbol{g}^{(c)}$ is only non-zero at the interface DOFs, the internal DOF related partition of $\boldsymbol{g}^{(c)}$ equals zero. Likewise, external forces are only applied at boundary DOFs. The reason for this is explained in Section 2.3.

Now, the partitions of the mass, damping, and stiffness matrices of all components are combined in block diagonal matrices:

$$\begin{aligned} \boldsymbol{M}_{ii} &= \operatorname{diag}\left(\boldsymbol{M}_{ii}^{(1)}, \ldots, \boldsymbol{M}_{ii}^{(n_c)}\right) & \boldsymbol{D}_{ii} &= \operatorname{diag}\left(\boldsymbol{D}_{ii}^{(1)}, \ldots, \boldsymbol{D}_{ii}^{(n_c)}\right) \\ \boldsymbol{M}_{ib} &= \boldsymbol{M}_{bi}^T = \operatorname{diag}\left(\boldsymbol{M}_{ib}^{(1)}, \ldots, \boldsymbol{M}_{ib}^{(n_c)}\right) & \boldsymbol{D}_{ib} &= \boldsymbol{D}_{bi}^T = \operatorname{diag}\left(\boldsymbol{D}_{ib}^{(1)}, \ldots, \boldsymbol{D}_{ib}^{(n_c)}\right) \\ \boldsymbol{M}_{bb} &= \operatorname{diag}\left(\boldsymbol{M}_{bb}^{(1)}, \ldots, \boldsymbol{M}_{bb}^{(n_c)}\right) & \boldsymbol{D}_{bb} &= \operatorname{diag}\left(\boldsymbol{D}_{bb}^{(1)}, \ldots, \boldsymbol{D}_{bb}^{(n_c)}\right) \\ & & \boldsymbol{K}_{ii} &= \operatorname{diag}\left(\boldsymbol{K}_{ii}^{(1)}, \ldots, \boldsymbol{K}_{ii}^{(n_c)}\right) \\ & & \boldsymbol{K}_{ib} &= \boldsymbol{K}_{bi}^T = \operatorname{diag}\left(\boldsymbol{K}_{ib}^{(1)}, \ldots, \boldsymbol{K}_{ib}^{(n_c)}\right) \\ & & \boldsymbol{K}_{bb} &= \operatorname{diag}\left(\boldsymbol{K}_{bb}^{(1)}, \ldots, \boldsymbol{K}_{bb}^{(n_c)}\right). \end{aligned} \tag{2.7}$$

The combined system matrices (as defined above), which are still uncoupled due to the block diagonal structure, are then assembled by exploiting the coupling conditions discussed in Section 2.2.1, where a unique boundary DOF field ($\boldsymbol{u}_\gamma$) is used to denote the behavior of all interface and retained DOFs in the assembly. Using the assembled mass, damping, and stiffness matrices ($\boldsymbol{M}^{(assy)}$, $\boldsymbol{D}^{(assy)}$, and $\boldsymbol{K}^{(assy)}$) and putting them in the form of an EOM for the assembled

system results in:

$$\underbrace{\begin{bmatrix} \boldsymbol{M}_{ii} & \boldsymbol{M}_{ib}\boldsymbol{L}_b \\ \boldsymbol{L}_b^T\boldsymbol{M}_{bi} & \boldsymbol{L}_b^T\boldsymbol{M}_{bb}\boldsymbol{L}_b \end{bmatrix}}_{\boldsymbol{M}^{(assy)}} \begin{bmatrix} \ddot{\boldsymbol{u}}_i^{(assy)} \\ \ddot{\boldsymbol{u}}_\gamma \end{bmatrix} + \underbrace{\begin{bmatrix} \boldsymbol{D}_{ii} & \boldsymbol{D}_{ib}\boldsymbol{L}_b \\ \boldsymbol{L}_b^T\boldsymbol{D}_{bi} & \boldsymbol{L}_b^T\boldsymbol{D}_{bb}\boldsymbol{L}_b \end{bmatrix}}_{\boldsymbol{D}^{(assy)}} \begin{bmatrix} \dot{\boldsymbol{u}}_i^{(assy)} \\ \dot{\boldsymbol{u}}_\gamma \end{bmatrix} + \dots$$
$$\underbrace{\begin{bmatrix} \boldsymbol{K}_{ii} & \boldsymbol{K}_{ib}\boldsymbol{L}_b \\ \boldsymbol{L}_b^T\boldsymbol{K}_{bi} & \boldsymbol{L}_b^T\boldsymbol{K}_{bb}\boldsymbol{L}_b \end{bmatrix}}_{\boldsymbol{K}^{(assy)}} \begin{bmatrix} \boldsymbol{u}_i^{(assy)} \\ \boldsymbol{u}_\gamma \end{bmatrix} = \begin{bmatrix} \boldsymbol{0} \\ \boldsymbol{L}_b^T\boldsymbol{f}_b^{(assy)} \end{bmatrix}. \tag{2.8}$$

Here, $\boldsymbol{u}_i^{(assy)}$ and $\boldsymbol{f}_b^{(assy)}$ are obtained by stacking their component equivalents ($\boldsymbol{u}_i^{(c)}$ and $\boldsymbol{f}_b^{(c)}$), in a way similar to the definition of $\boldsymbol{u}^{(assy)}$ in Equation (2.2). Note that, in this equation, the interface force term has disappeared. In a detailed derivation of Equation (2.8), given in the work of Voormeren [31], it is shown that this is a consequence of the force equilibrium condition (see Equation (2.3)). As a result of the compatibility condition, Equation (2.8) uses a unique boundary degree of freedom field ($\boldsymbol{u}_\gamma$), in which all interface DOFs are represented once.

The assembly technique shown in Equation (2.8) is referred to as the primal stiffness assembly method. This means that interfaces are described in terms of stiffness instead of flexibility and that the intermediate field is given in terms of displacements/rotations instead of forces/moments. Since the specific type of physical coupling is not of primary concern in this research, it was chosen to only introduce the most common coupling variant in this thesis. For a more detailed explanation of the other options, the work of Voormeren [31, 32] should be consulted.

2.2.3 Lagrange multiplier frequency-based substructuring

As an alternative to assembling the component system matrices in the physical domain, subsystems can also be coupled in the frequency domain. An advantage with respect to coupling in the physical domain, is that coupling in the frequency domain enables the direct use of measured frequency response functions (FRFs). Furthermore, specific input-output behavior can be analyzed, which can be beneficial if the behavior at particular POIs is of interest. A disadvantage is however that the system matrices of the assembly are not obtained. Therefore, physical insight in the form of, for example, mode shapes is not acquired.

Although multiple frequency-based coupling methods have been developed, this section is confined to the Lagrange multiplier frequency-based substructuring (LM FBS) method introduced by de Klerk et al. [16]. This technique uses the receptance matrices of uncoupled components ($\boldsymbol{Y}^{(c)}$) and returns the receptance matrix of the assembly of these components ($\boldsymbol{Y}^{(assy)}$).

Since an elaborate discussion of the LM FBS method is already given by de Klerk et al. [16], in this section, a brief derivation of this method is given. For this, first, the definition of the receptance matrix of a single component is given by

$$\underbrace{\begin{bmatrix} \boldsymbol{U}_i^{(c)}(s) \\ \boldsymbol{U}_b^{(c)}(s) \end{bmatrix}}_{\boldsymbol{U}^{(c)}} = \underbrace{\begin{bmatrix} \boldsymbol{Y}_{ii}^{(c)}(s) & \boldsymbol{Y}_{ib}^{(c)}(s) \\ \boldsymbol{Y}_{bi}^{(c)}(s) & \boldsymbol{Y}_{bb}^{(c)}(s) \end{bmatrix}}_{\boldsymbol{Y}^{(c)}(s)} \underbrace{\begin{bmatrix} \boldsymbol{F}_i^{(c)}(s) \\ \boldsymbol{F}_b^{(c)}(s) \end{bmatrix}}_{\boldsymbol{F}^{(c)}} \quad s \in \mathbb{C}, \tag{2.9}$$

where the transfers related to boundary DOFs ($\boldsymbol{U}_b^{(c)}$) and internal DOFs ($\boldsymbol{U}_i^{(c)}$) are partitioned. Note that the force $\boldsymbol{F}_b^{(c)}$ represents both interface forces (at the interface DOFs) and externally

applied forces at the boundary DOFs. Furthermore, the boldface letters in this equation indicate the MIMO nature of the receptances and in- and outputs. The input and output vectors, $\boldsymbol{F}^{(c)}(s)$ and $\boldsymbol{U}^{(c)}(s)$ can therefore simultaneously represent multiple forces/moments and displacements/rotations, respectively. In the rest of this thesis, the explicit dependency on s is omitted for brevity.

The receptance matrices of multiple components can, similar to the system matrices in Section 2.2.2, be combined in a block diagonal structure, which results in a receptance matrix containing uncoupled component receptances:

$$\boldsymbol{Y} = \text{diag}\left(\boldsymbol{Y}^{(1)}, \ldots, \boldsymbol{Y}^{(n_c)}\right). \tag{2.10}$$

Since the inverse of the receptance matrix equals the dynamic stiffness, the dynamic stiffness of all uncoupled components is written given by

$$\boldsymbol{Z} = \text{diag}\left(\boldsymbol{Z}^{(1)}, \ldots, \boldsymbol{Z}^{(n_c)}\right) = \text{diag}\left({\boldsymbol{Y}^{(1)}}^{-1}, \ldots, {\boldsymbol{Y}^{(n_c)}}^{-1}\right) = \boldsymbol{Y}^{-1}. \tag{2.11}$$

Using $\boldsymbol{Z}^{(c)}$ as a transfer between $\boldsymbol{U}^{(c)}$ and $\boldsymbol{F}^{(c)}$ of a single component, gives

$$\boldsymbol{Z}^{(c)}\boldsymbol{U}^{(c)} = \boldsymbol{F}^{(c)}. \tag{2.12}$$

When such a transfer is written for an assembly using $\boldsymbol{Z}$ (as defined in Equation (2.11)), the (yet unknown) interfaces forces can be isolated, such that the externally applied forces are represented by $\boldsymbol{F}^{(assy)}$ (note that $\boldsymbol{F}^{(assy)}$ now does not contain any interface forces anymore):

$$\boldsymbol{Z}\boldsymbol{U}^{(assy)} + \boldsymbol{B}_f^T\boldsymbol{\lambda} = \boldsymbol{F}^{(assy)}, \tag{2.13}$$

where the interface forces, denoted by $\boldsymbol{\lambda}$, are also referred to as Lagrange multipliers, and the boolean matrix $\boldsymbol{B}_f^T$ ensures that these forces are applied to the interface DOFs. Rewriting Equation (2.13), results in

$$\boldsymbol{U}^{(assy)} = \boldsymbol{Z}^{-1}\left(\boldsymbol{F}^{(assy)} - \boldsymbol{B}_f^T\boldsymbol{\lambda}\right) \tag{2.14}$$

$$= \boldsymbol{Y}\left(\boldsymbol{F}^{(assy)} - \boldsymbol{B}_f^T\boldsymbol{\lambda}\right), \tag{2.15}$$

which, by pre-multiplying with $\boldsymbol{B}_f$ and using the compatibility condition ($\boldsymbol{B}_f\boldsymbol{U}^{(assy)} = \boldsymbol{0}$), gives

$$\boldsymbol{B}_f\boldsymbol{Y}\left(\boldsymbol{F}^{(assy)} - \boldsymbol{B}_f^T\boldsymbol{\lambda}\right) = \boldsymbol{0} \tag{2.16}$$

$$\boldsymbol{B}_f\boldsymbol{Y}\boldsymbol{B}_f^T\boldsymbol{\lambda} = \boldsymbol{B}_f\boldsymbol{Y}\boldsymbol{F}^{(assy)}. \tag{2.17}$$

Solving Equation (2.17) for $\boldsymbol{\lambda}$ and substituting the result in Equation (2.15), gives an expression for the transfer from $\boldsymbol{F}^{(assy)}$ to $\boldsymbol{U}^{(assy)}$:

$$\boldsymbol{U}^{(assy)} = \underbrace{\boldsymbol{Y}\boldsymbol{F}^{(assy)}}_{\boldsymbol{C}_1} - \underbrace{\boldsymbol{Y}\boldsymbol{B}_f^T\underbrace{\underbrace{\left(\boldsymbol{B}_f\boldsymbol{Y}\boldsymbol{B}_f^T\right)^{-1}\underbrace{\boldsymbol{B}_f\boldsymbol{Y}\boldsymbol{F}^{(assy)}}_{\boldsymbol{C}_2}}_{\boldsymbol{C}_3=\boldsymbol{\lambda}}}_{\boldsymbol{C}_4}}. \tag{2.18}$$

In Equation (2.18), the term indicated by $\boldsymbol{C}_1$ represents the response an unconnected substructure would have due to an applied force on that particular uncoupled substructure. The second term ($\boldsymbol{C}_4$) is subdivided in three parts. The first part, $\boldsymbol{C}_2$, denotes the gap that would originate when a force $\boldsymbol{F}^{(assy)}$ is applied. This gap is caused by displacements at the interfaces. Because

of compatibility, this gap is however not allowed to exist and thus a force has to be present which 'closes' this gap. This force is given by $\boldsymbol{C}_3$ which actually equals the Lagrange multiplier $\boldsymbol{\lambda}$. This 'connecting' force, in turn, also influences the displacement $\boldsymbol{U}^{(assy)}$. This influence is given by $\boldsymbol{C}_4$.

Slightly rearranging Equation (2.18), gives

$$\boldsymbol{U}^{(assy)} = \left(\boldsymbol{Y} - \boldsymbol{Y}\boldsymbol{B}_f^T(\boldsymbol{B}_f\boldsymbol{Y}\boldsymbol{B}_f^T)^{-1}\boldsymbol{B}_f\boldsymbol{Y}\right)\boldsymbol{F}^{(assy)}, \tag{2.19}$$

where an expression for the receptance matrix of the assembly in terms of the uncoupled component receptances ($\boldsymbol{Y}$) is recognized:

$$\boldsymbol{Y}^{(assy)} = \boldsymbol{Y} - \boldsymbol{Y}\boldsymbol{B}_f^T(\boldsymbol{B}_f\boldsymbol{Y}\boldsymbol{B}_f^T)^{-1}\boldsymbol{B}_f\boldsymbol{Y}. \tag{2.20}$$

2.2.4 Feedback coupling

A different technique to couple components in the frequency domain is by using a feedback representation, as commonly used in control theory. In this section, this technique will be introduced by applying it to a system consisting of two subsystems ($\boldsymbol{\Sigma}^{(1)}$ and $\boldsymbol{\Sigma}^{(2)}$), where the input $\boldsymbol{u}$ is located at subsystem 1 and the output $\boldsymbol{y}$ is located at subsystem 2; $\boldsymbol{u}$ and $\boldsymbol{y}$ are thus non-colocated. A system diagram hereof is shown in Figure 2.2. Furthermore, both subsystems are interconnected by the interface variables $\boldsymbol{v}$ and $\boldsymbol{w}$. Clearly, a feedback loop between both systems is recognized here; $\boldsymbol{w}$ depends on $\boldsymbol{v}$, which itself again depends on $\boldsymbol{w}$. Note that, as is evident from the boldface variables, both subsystems represent MIMO systems. As indicated by Figure 2.2, $\boldsymbol{u}$, $\boldsymbol{y}$, $\boldsymbol{v}$, and $\boldsymbol{w}$ are connected to each other by transfer function matrices $\boldsymbol{H}^{(c)}$ within each subsystem. The subscript of $\boldsymbol{H}^{(c)}$ denotes between which in- and output this specific transfer acts. The transfer functions constituting the feedback loop ($\boldsymbol{H}_{wv}^{(1)}$ and $\boldsymbol{H}_{vw}^{(2)}$) are also referred to as the feedback loop transfer functions. It is important to remark that the transfer functions in Figure 2.2 can represent different types of transfers (e.g., receptance, dynamic stiffness, mobility, etc.), depending on the units of their in- and output variables.

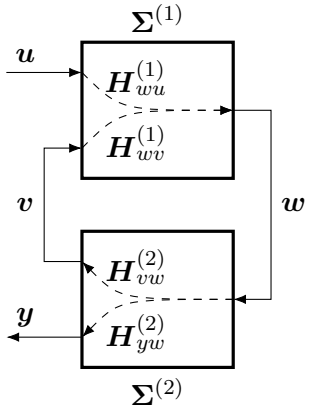

Figure 2.2: *System representation of two coupled subsystems in a feedback form, with non-colocated input and output.*

Next, the component-specific transfer functions ($\boldsymbol{H}^{(c)}$) are combined to define the direct transfer from $\boldsymbol{u}$ to $\boldsymbol{y}$:

$$\boldsymbol{H}_{yu}^{(assy)} = \boldsymbol{H}_{yw}^{(2)}(\boldsymbol{I} - \boldsymbol{H}_{wv}^{(1)}\boldsymbol{H}_{vw}^{(2)})^{-1}\boldsymbol{H}_{wu}^{(1)}. \tag{2.21}$$

Proof. Using Figure 2.2 as a guideline and starting with

$$\boldsymbol{y} = \boldsymbol{H}_{yw}^{(2)}\boldsymbol{w}, \tag{2.22}$$

it is clear that an expression for $\boldsymbol{w}$ should be obtained in order to write $\boldsymbol{y}$ as a function of the input $\boldsymbol{u}$. An expression for $\boldsymbol{w}$ is therefore given by

$$\boldsymbol{w} = \boldsymbol{H}_{wu}^{(1)}\boldsymbol{u} + \boldsymbol{H}_{wv}^{(1)}\boldsymbol{v}, \tag{2.23}$$

where

$$\boldsymbol{v} = \boldsymbol{H}_{vw}^{(2)}\boldsymbol{w}. \tag{2.24}$$

Substituting (2.24) in (2.23), results in

$$\boldsymbol{w} = \boldsymbol{H}_{wu}^{(1)}\boldsymbol{u} + \boldsymbol{H}_{wv}^{(1)}\boldsymbol{H}_{vw}^{(2)}\boldsymbol{w} \tag{2.25}$$

$$(\boldsymbol{I} - \boldsymbol{H}_{wv}^{(1)}\boldsymbol{H}_{vw}^{(2)})\boldsymbol{w} = \boldsymbol{H}_{wu}^{(1)}\boldsymbol{u} \tag{2.26}$$

$$\boldsymbol{w} = (\boldsymbol{I} - \boldsymbol{H}_{wv}^{(1)}\boldsymbol{H}_{vw}^{(2)})^{-1}\boldsymbol{H}_{wu}^{(1)}\boldsymbol{u}, \tag{2.27}$$

which can be substituted in (2.22) to obtain an expression for $\boldsymbol{y}$ in terms of $\boldsymbol{u}$:

$$\boldsymbol{y} = \underbrace{\left(\boldsymbol{H}_{yw}^{(2)}(\boldsymbol{I} - \boldsymbol{H}_{wv}^{(1)}\boldsymbol{H}_{vw}^{(2)})^{-1}\boldsymbol{H}_{wu}^{(1)}\right)}_{\boldsymbol{H}_{yu}^{(assy)}}\boldsymbol{u}. \tag{2.28}$$

Hereby, an expression for the direct transfer from an input at subsystem 1 to an output at subsystem 2 is given by $\boldsymbol{H}_{yu}^{(assy)}$, which equals its definition in Equation (2.21). □

In the following, a mechanical system consisting of two components is written such that it fits the feedback form of Figure 2.2. For this, a two-component cantilever beam which is shown in Figure 2.3, is used. In this figure, the receptances related to two points of interest (one at each component, depicted by the blue dots) and the interfaces (green dots) are indicated. Here, it should be mentioned that, just like in Figure 2.2, there are no direct transfers between the subsystems.

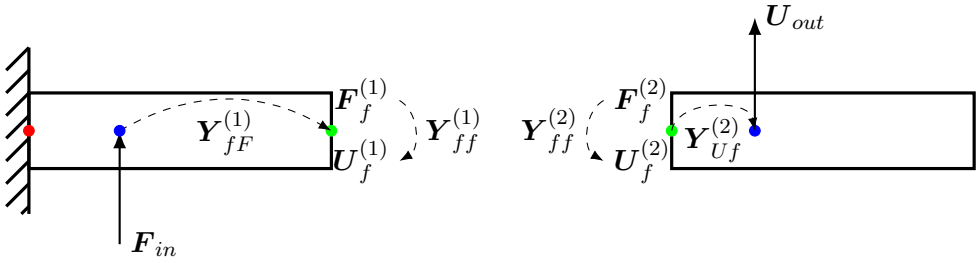

Figure 2.3: *Schematic representation of a two-component cantilever beam with input at subsystem 1 and output at subsystem 2, and corresponding forces, displacements, and receptances.*

Substituting the input and output in Figure 2.2 by the in- and output of the 2-component cantilever beam ($\boldsymbol{F}_{in}$ and $\boldsymbol{U}_{out}$) results in Figure 2.4 which shows a block diagram of a feedback representation of the cantilever beam. For the interface variables, the interface displacement at component 2 ($\boldsymbol{U}_f^{(2)}$) and the interface force at component 1 ($\boldsymbol{F}_f^{(1)}$) are used.

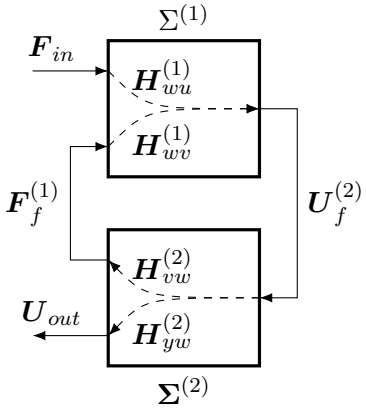

Figure 2.4: *Two mechanical subsystems (of the cantilever beam) written in feedback form, with corresponding input, output, and interface variables.*

Now, expressions for the general transfer functions (indicated by $\boldsymbol{H}^{(c)}$) in terms of the specific receptances of the cantilever beam (denoted by $\boldsymbol{Y}^{(c)}$) can be obtained. For this, the variables coming out of each subsystem block in Figure 2.4 should be a function of the inputs of that specific component and its receptances. For component 1, this results in requirement (2.29a):

$$\boldsymbol{U}_f^{(2)} = f_1\left(\boldsymbol{F}_{in}, \boldsymbol{F}_f^{(1)}\right), \tag{2.29a}$$

where $f(\cdot)$ indicates that a variable is a function of some other variable(s). For the second component, expressions should be found such that requirements (2.29b) and (2.29c) are met.

$$\boldsymbol{F}_f^{(1)} = f_2\left(\boldsymbol{U}_f^{(2)}\right) \tag{2.29b}$$

$$\boldsymbol{U}_{out} = f_3\left(\boldsymbol{U}_f^{(2)}\right) \tag{2.29c}$$

By following the steps in Appendix B.3, in which the coupling conditions have been exploited, Equations (2.30a), (2.30b), and (2.30c) are obtained, which satisfy these requirements:

$$\boldsymbol{U}_f^{(2)} = \boldsymbol{Y}_{fF}^{(1)}\boldsymbol{F}_{in} + \boldsymbol{Y}_{ff}^{(1)}\boldsymbol{F}_f^{(1)}, \tag{2.30a}$$

$$\boldsymbol{F}_f^{(1)} = -{\boldsymbol{Y}_{ff}^{(2)}}^{-1}\boldsymbol{U}_f^{(2)}, \tag{2.30b}$$

$$\boldsymbol{U}_{out} = \boldsymbol{Y}_{Uf}^{(2)}{\boldsymbol{Y}_{ff}^{(2)}}^{-1}\boldsymbol{U}_f^{(2)}. \tag{2.30c}$$

Here, Equations (2.30a)-(2.30c) are used to define the general transfer functions (as used in Figure 2.4) in terms of the receptances of the cantilever beam:

$$\boldsymbol{H}_{wu}^{(1)} = \boldsymbol{Y}_{fF}^{(1)} \tag{2.31a}$$

$$\boldsymbol{H}_{wv}^{(1)} = \boldsymbol{Y}_{ff}^{(1)} \tag{2.31b}$$

$$\boldsymbol{H}_{vw}^{(2)} = -{\boldsymbol{Y}_{ff}^{(2)}}^{-1} \tag{2.31c}$$

$$\boldsymbol{H}_{yw}^{(2)} = \boldsymbol{Y}_{Uf}^{(2)}{\boldsymbol{Y}_{ff}^{(2)}}^{-1}. \tag{2.31d}$$

Equations (2.30a)-(2.31d) show that the general transfer functions represent different types of transfer functions, as was mentioned before. For instance, as is evident from Equation (2.30a), both $\boldsymbol{H}_{wu}^{(1)}$ and $\boldsymbol{H}_{wv}^{(1)}$ represent receptances, since these link a force to a resulting displacement. Equation (2.30b) however shows that $\boldsymbol{H}_{vw}^{(2)}$ gives a transfer from a displacement to a force and

hence represents a dynamic stiffness. Finally, (2.30c) shows that $\boldsymbol{H}_{yw}^{(2)}$ gives a displacement as a function of a displacement and hence is a transmissibility.

Now, using Equations (2.30a)-(2.30c), Equation (2.21) can be translated to a function which gives the direct transfer from an input force at component 1 to the displacement at an output which is located at component 2 in terms of the receptances defined in Figure 2.3 (as used in Figure 2.3):

$$\boldsymbol{Y}_{UF,\text{Feedback}}^{(assy)} = \boldsymbol{Y}_{Uf}^{(2)}\boldsymbol{Y}_{ff}^{(2)^{-1}}\left(\boldsymbol{I} + \boldsymbol{Y}_{ff}^{(1)}\boldsymbol{Y}_{ff}^{(2)^{-1}}\right)^{-1}\boldsymbol{Y}_{fF}^{(1)}. \tag{2.32}$$

Note that this equation serves the same purpose as Equation (2.20), namely coupling component transfer functions such that transfers related to the assembled system are obtained.

2.2.5 Comparison of frequency-based coupling techniques

In the previous sections, two methods to assemble components in the frequency domain have been shown; using the LM FBS method, an expression for the assembly receptance was obtained in Equation (2.20), and a different expression for the assembly receptance was found using a feedback representation approach in Equation (2.32). This section will show that these expressions are equivalent, but that they have different applications.

Since the LM FBS expression for the assembly receptance matrix (found in Equation (2.20)) is written in a general form, first, this expression is used to find the same specific transfer as investigated for the feedback-coupled expression ($\boldsymbol{F}_{in}$ to $\boldsymbol{U}_{out}$), where the receptances as defined in Figure 2.3 are used. For this, the fact that the boolean mapping matrix $\boldsymbol{B}_f$ selects the interface-related partitions of $\boldsymbol{Y}$ (e.g., $\boldsymbol{B}_f\boldsymbol{Y}\boldsymbol{B}_f^T = \boldsymbol{Y}_{ff}$) is used, resulting in

$$\boldsymbol{Y}_{UF,\text{LM FBS}}^{(assy)} = \boldsymbol{Y}_{Uf}^{(2)}\left(\boldsymbol{Y}_{ff}^{(1)} + \boldsymbol{Y}_{ff}^{(2)}\right)^{-1}\boldsymbol{Y}_{fF}^{(1)}, \tag{2.33}$$

where the subscripts U and F denote the out- and input of the assembly transfer, respectively. Since Equations (2.32) and (2.33) represent the same (direct) receptance matrix, it holds that

$$\boldsymbol{Y}_{UF,\text{LM FBS}}^{(assy)} = \boldsymbol{Y}_{UF,\text{Feedback}}^{(assy)}. \tag{2.34}$$

Although not obvious at first, this statement can be proven by substituting the expressions for $\boldsymbol{Y}_{UF,Feedback}^{(assy)}$ and $\boldsymbol{Y}_{UF,\text{LM FBS}}^{(assy)}$ (given in Equations (2.32) and (2.33), respectively) in Equation (2.34):

$$\left(\boldsymbol{Y}_{ff}^{(1)} + \boldsymbol{Y}_{ff}^{(2)}\right)^{-1} = \underbrace{\boldsymbol{Y}_{ff}^{(2)}}_{\boldsymbol{B}}{}^{-1}\underbrace{\left(\boldsymbol{I} + \boldsymbol{Y}_{ff}^{(1)}\boldsymbol{Y}_{ff}^{(2)^{-1}}\right)}_{\boldsymbol{A}}{}^{-1}, \tag{2.35}$$

where it has been recognized that the terms $\boldsymbol{Y}_{Uf}^{(2)}$ and $\boldsymbol{Y}_{fF}^{(1)}$ can be omitted on both sides of the equality sign. Now, using the mathematical rule $\boldsymbol{B}^{-1}\boldsymbol{A}^{-1} = (\boldsymbol{A}\boldsymbol{B})^{-1}$, where $\boldsymbol{A}$ and $\boldsymbol{B}$ indicate terms in Equation (2.35), the right-hand side of this equation can be rewritten to

$$\boldsymbol{Y}_{ff}^{(2)^{-1}}\left(\boldsymbol{I} + \boldsymbol{Y}_{ff}^{(1)}\boldsymbol{Y}_{ff}^{(2)^{-1}}\right)^{-1} = \left(\left(\boldsymbol{I} + \boldsymbol{Y}_{ff}^{(1)}\boldsymbol{Y}_{ff}^{(2)^{-1}}\right)\boldsymbol{Y}_{ff}^{(2)}\right)^{-1} \tag{2.36}$$

$$= \left(\boldsymbol{Y}_{ff}^{(1)} + \boldsymbol{Y}_{ff}^{(2)}\right)^{-1}. \tag{2.37}$$

Hereby, it is shown that Equation (2.35) holds, hence proving that the expressions for $\boldsymbol{Y}_{UF,Feedback}^{(assy)}$ and $\boldsymbol{Y}_{UF,\text{LM FBS}}^{(assy)}$ are indeed equivalent.

Although both methods result in equivalent assembly receptances, there are some important distinctions to be made. For example, the LM FBS framework can be easily used to couple more than two subsystems. For the feedback representation method this would however be much more complex and cumbersome due to the lack of a general form. On the other hand, since Equation (2.33) is not exactly given in the form of Equation (2.21) (due to different use of the inverse terms in both equations), the LM FBS method does not directly provide suitable expressions for the (general) transfer functions, as required for Figure 2.4. The feedback coupling technique was however especially tailored for this purpose. Finally, the LM FBS expression gives a general expression for transfers between all possible combinations of in- and outputs, whereas the feedback representation is derived for a specific single (assembly) transfer with particular in- and outputs. Therefore, the LM FBS method is relatively versatile compared to the feedback representation approach.

2.3 Component reduction

Since complex systems are divided in multiple components in the DS framework, these individual component models can be reduced in order to make them (and their assembly) computationally more attractive. In this research, reduction techniques which use a transformation of a component model to a model consisting of mode shapes are utilized. These shapes essentially project different combinations of displacements/rotations of all degrees of freedom in a component. A single mode shape can thus capture the effect of many DOFs very efficiently. By only using a subset of all modes, a reduced component model is obtained which gives an accurate representation of the dynamical behavior of that component.

Traditionally, this truncation is done in such a way that all modes with eigenfrequencies up to a pre-determined cutoff frequency are kept. This cutoff frequency is often based on a user-defined frequency range of interest which, for instance, depends on the expected frequency range of disturbances. Furthermore, due to high-frequency roll-off which is typical for mechanical systems, the high-frequency behavior is often not of interest. Therefore, retaining all eigenmodes with eigenfrequencies below this user-defined cutoff frequency typically results in a sufficiently accurate reduced component model which is accurate in the frequency range below the cutoff frequency.

The reduction of a component is explained by investigating how the size of the mass, damping, and stiffness matrices in the EOM can be reduced. As discussed before, a vector containing the unreduced degrees of freedom in a component is given by $\boldsymbol{u}^{(c)}$. By defining a reduction basis $\boldsymbol{T}^{(c)} \in \mathbb{R}^{n_m^{(c)} \times n_r^{(c)}}$, where $n_r^{(c)}$ represents the number of DOFs of the reduced system and in which the selected mode shapes are collected, this unreduced vector is approximated by

$$\boldsymbol{u}^{(c)} \approx \boldsymbol{T}^{(c)} \hat{\boldsymbol{u}}^{(c)}. \tag{2.38}$$

Here, $\hat{\boldsymbol{u}}^{(c)}$ is a reduced vector of DOFs which contains generalized DOFs ($\boldsymbol{q}^{(c)}$) and possibly some of the original unreduced DOFs (as will be seen in Sections 2.3.2 and 2.3.3). The generalized degrees of freedom represent the amplifications of the mode shapes in $\boldsymbol{T}^{(c)}$.

Now, substituting this expression for $\boldsymbol{u}^{(c)}$ in the EOM (Equation (2.5)), results in

$$\boldsymbol{M}^{(c)}\boldsymbol{T}^{(c)}\ddot{\hat{\boldsymbol{u}}}^{(c)} + \boldsymbol{D}^{(c)}\boldsymbol{T}^{(c)}\dot{\hat{\boldsymbol{u}}}^{(c)} + \boldsymbol{K}^{(c)}\boldsymbol{T}^{(c)}\hat{\boldsymbol{u}}^{(\boldsymbol{c})} = \boldsymbol{f}^{(c)} + \boldsymbol{g}^{(c)} + \boldsymbol{r}^{(c)}, \tag{2.39}$$

where $\boldsymbol{r}^{(c)}$ is a residual force which is introduced due to the fact that the reduction does, by definition, not give an exact solution. By pre-multiplication of Equation (2.39) with the

transpose of $\boldsymbol{T}^{(c)}$, it is imposed that this residual force should be zero in the space spanned by the reduction basis however ($\boldsymbol{T}^{(c)^T}\boldsymbol{r}^{(c)} = \boldsymbol{0}$) [31]. Equation (2.39) then results in

$$\underbrace{\boldsymbol{T}^{(c)^T}\boldsymbol{M}^{(c)}\boldsymbol{T}^{(c)}}_{\hat{\boldsymbol{M}}^{(c)}}\ddot{\hat{\boldsymbol{u}}}^{(c)} + \underbrace{\boldsymbol{T}^{(c)^T}\boldsymbol{D}^{(c)}\boldsymbol{T}^{(c)}}_{\hat{\boldsymbol{D}}^{(c)}}\dot{\hat{\boldsymbol{u}}}^{(c)} + \underbrace{\boldsymbol{T}^{(c)^T}\boldsymbol{K}^{(c)}\boldsymbol{T}^{(c)}}_{\hat{\boldsymbol{K}}^{(c)}}\hat{\boldsymbol{u}}^{(c)} = \underbrace{\boldsymbol{T}^{(c)^T}\boldsymbol{f}^{(c)}}_{\hat{\boldsymbol{f}}^{(c)}} + \underbrace{\boldsymbol{T}^{(c)^T}\boldsymbol{g}^{(c)}}_{\hat{\boldsymbol{g}}^{(c)}}, \quad (2.40)$$

where expressions for the reduced system matrices ($\hat{\boldsymbol{M}}^{(c)}, \hat{\boldsymbol{D}}^{(c)}, \hat{\boldsymbol{K}}^{(c)} \in \mathbb{R}^{n_r^{(c)} \times n_r^{(c)}}$) as well as the reduced external and interface forces ($\hat{\boldsymbol{f}}^{(c)}$ and $\hat{\boldsymbol{g}}^{(c)}$) are given.

In the following sections, different definitions of the reduction basis are introduced by discussing three distinct methods. The last two methods are component mode synthesis methods. As will be discussed, an important difference between CMS and non-CMS methods is that CMS methods facilitate the assembly of uncoupled components. This is achieved by explicitly keeping the boundary DOFs ($\boldsymbol{u}_b^{(c)}$) in $\hat{\boldsymbol{u}}^{(c)}$ which, in contrast to the internal DOFs, will thus not be substituted by generalized coordinates.

2.3.1 Modal truncation

Modal truncation (MT) is a technique which uses (a selection of) undamped dynamic eigenmodes of a subsystem as the sole ingredient of its reduction basis. These eigenmodes are the eigenvectors $\boldsymbol{\phi}_k^{(c)}$ of the undamped eigenvalue problem defined below:

$$\left(\boldsymbol{K}^{(c)} - {\omega_k^{(c)}}^2\boldsymbol{M}^{(c)}\right)\boldsymbol{\phi}_k^{(c)} = \boldsymbol{0}, \quad (2.41)$$

where $\omega_k^{(c)}$ is the angular eigenfrequency associated to mode $\boldsymbol{\phi}_k^{(c)}$. The total amount of eigenmodes ($n_m^{(c)}$) that can be found using this equation is equal to the number of DOFs in the component (which equals the number of columns/rows in $\boldsymbol{K}^{(c)}$, $\boldsymbol{D}^{(c)}$, and $\boldsymbol{M}^{(c)}$). The indexes of the set of all eigenmodes are given by the set $\mathcal{M}^{(c)} = \left\{1, ..., n_m^{(c)}\right\}$. Now, by choosing a subset $\mathcal{K}^{(c)} = \left\{k \in \mathcal{M}^{(c)}\right\}$ of these modes which represents the set of kept modes, Equation (2.38) can be written as

$$\boldsymbol{u}^{(c)} \approx \boldsymbol{\Phi}_{\mathcal{K}^{(c)}}^{(c)}\boldsymbol{q}^{(c)} = \boldsymbol{T}_{MT}^{(c)}\boldsymbol{q}^{(c)} = \boldsymbol{T}_{MT}^{(c)}\hat{\boldsymbol{u}}^{(c)}, \quad (2.42)$$

where the columns of $\boldsymbol{\Phi}_{\mathcal{K}^{(c)}}^{(c)}$ are all kept eigenvectors $\boldsymbol{\phi}_k^{(c)}$, for which $k \in \mathcal{K}^{(c)}$. Since these vectors are the only ingredient of the reduction bases, $\boldsymbol{T}_{MT}^{(c)} = \boldsymbol{\Phi}_{\mathcal{K}^{(c)}}^{(c)}$. As shown in Equation (2.42), all degrees of freedom of the unreduced system are replaced by generalized coordinates $\boldsymbol{q}^{(c)}$. As a consequence, the boundary DOFs are not explicitly kept and hence straightforward coupling is not feasible for this method. Therefore, different component reduction techniques are introduced in Sections 2.3.2 and 2.3.3.

The eigenmodes which are not used in the reduction basis are referred to as deleted modes and are represented by the set $\mathcal{D}^{(c)} = \left\{d \in \mathcal{M}^{(c)}, d \notin \mathcal{K}^{(c)}\right\}$. Since all modes have a certain static contribution, deleting some modes causes the reduced system to be, by definition, statically inexact. Therefore, techniques have been developed which compensate for this static error by only taking the static contribution of the deleted modes into account [9]. Finally, if $\mathcal{D}^{(c)}$ is an empty set, and thus all modes are kept, the reduced and unreduced models are equivalent. In this case, $\boldsymbol{T}_{MT}^{(c)}$ does not provide a reduction, but rather a coordinate transformation.

2.3.2 Craig-Bampton

To ensure that reduced components can be assembled, component mode synthesis methods will be used. One such method, which is widely applied (also within ASML) is the Craig-Bampton method [6].

Instead of the vibration modes which were used for the modal truncation technique, this method uses so-called fixed boundary vibration modes $\boldsymbol{\phi}^{(c)}_{fixed}$ for its reduction basis. This means that the dynamic modes of the system are determined in case all interface and retained DOFs are fixed. These eigenmodes are obtained by solving the (undamped) eigenvalue problem:

$$\left(\boldsymbol{K}^{(c)}_{ii} - {\omega^{(c)}_k}^2 \boldsymbol{M}^{(c)}_{ii}\right) \boldsymbol{\phi}^{(c)}_{fixed,k} = \boldsymbol{0}, \tag{2.43}$$

where, by only using the internal DOF related partitions of $\boldsymbol{M}^{(c)}$ and $\boldsymbol{K}^{(c)}$, the boundary degrees of freedom are virtually constrained. A kept set of these undamped vibration modes, used for the reduction basis, is collected in the set of kept fixed vibration modes $\boldsymbol{\Phi}^{(c)}_{\mathcal{K}^{(c)},fixed}$.

Besides dynamic/vibration modes, static modes (which are related to the boundary DOFs) are present in CMS reduction bases. Because of this, in contrast to the modal truncation method, which is statically inexact, the static behavior at the boundary DOFs is approximated accurately. Since the boundary DOFs represent both interface and retained DOFs, the components reduced using CMS are thus statically exact at the interface and retained DOFs. For this reason, POIs are typically included in the set of retained DOFs.

In the Craig-Bampton method, these static modes are given by so-called constraint modes. These modes are obtained by evaluating the static problem (so without inertial influences) for the internal DOF related partition of Equation (2.6). Using the fact that it was specified that no external forces act on the internal DOFs, the internal DOF related partition of these modes is written as

$$\boldsymbol{\Psi}^{(c)}_{const} = -{\boldsymbol{K}^{(c)}_{ii}}^{-1} \boldsymbol{K}^{(c)}_{ib}, \tag{2.44}$$

which represents a condensation of the internal static behavior to the boundary DOFs [31].

Now, $\boldsymbol{\Phi}^{(c)}_{\mathcal{K}^{(c)},fixed}$ and $\boldsymbol{\Psi}^{(c)}_{const}$ are used to define a reduction matrix for the CB method ($\boldsymbol{T}^{(c)}_{CB}$). An expression for this matrix is given in Equation (2.45).

$$\underbrace{\begin{bmatrix} \boldsymbol{u}^{(c)}_i \\ \boldsymbol{u}^{(c)}_b \end{bmatrix}}_{\boldsymbol{u}^{(c)}} \approx \underbrace{\begin{bmatrix} \boldsymbol{\Phi}^{(c)}_{\mathcal{K}^{(c)},fixed} & \boldsymbol{\Psi}^{(c)}_{const} \\ \boldsymbol{0} & \boldsymbol{I} \end{bmatrix}}_{\boldsymbol{T}^{(c)}_{CB}} \underbrace{\begin{bmatrix} \boldsymbol{q}^{(c)}_i \\ \boldsymbol{u}^{(c)}_b \end{bmatrix}}_{\hat{\boldsymbol{u}}^{(c)}} \tag{2.45}$$

In this equation, $\boldsymbol{u}^{(c)}$ and $\hat{\boldsymbol{u}}^{(c)}$ are separated in partitions related to internal and boundary degrees of freedom and the reduction matrix is partitioned accordingly. Furthermore, $\boldsymbol{q}^{(c)}_i$ represents a vector containing the generalized DOFs for the vibration modes indicating deflections of the kept eigenmodes.

As can be seen in Equation (2.45), $\boldsymbol{\Phi}^{(c)}_{\mathcal{K}^{(c)},fixed}$ and $\boldsymbol{\Psi}^{(c)}_{const}$ represent shapes that are related to the internal DOFs only. Hence, no information about the behavior of the boundary degrees of freedom is present in these modes. Therefore, the vibration modes for all DOFs of the substructure are given by the left column partition in $\boldsymbol{T}^{(c)}_{CB}$, where $\boldsymbol{\Phi}^{(c)}_{\mathcal{K}^{(c)},fixed}$ is appended by a zero-matrix, indicating that the boundary DOFs were virtually constrained for the fixed-boundary vibration modes. Furthermore, the constraint modes (given by the right column

partition of $\boldsymbol{T}_{CB}^{(c)}$, where $\boldsymbol{\Psi}_{const}^{(c)}$ is appended with an identity matrix) are defined as the static deformation of the internal DOFs caused by a unit displacement/rotation applied to a single boundary DOF, where all other boundary DOFs have zero displacement/rotation. Therefore, for each constraint mode, all boundary DOFs have zero deflection except for one, as is indicated by the identity matrix in the lower right partition of $\boldsymbol{T}_{CB}^{(c)}$. Due to this identity matrix, the lower row in Equation (2.45) reads $\boldsymbol{u}_b^{(c)} = \boldsymbol{u}_b^{(c)}$, which shows that the boundary degrees of freedom are indeed kept explicitly and thus enables the coupling of the reduced components.

Finally, it should be remarked that a downside of the fixed-boundary vibration modes is that they are very difficult (or impossible) to measure experimentally, making experimental validation of the numerical eigenmodes very challenging [31]. Furthermore, since each boundary DOF has a single associated static mode, systems with large interfaces can have a large amount of static modes. To counteract this problem, interface reduction can be applied [31]. Since in this research only systems with relatively small interfaces are investigated, interface reduction is not discussed in detail here.

2.3.3 Hintz-Herting

Another widely used CMS method within ASML is the method coined by Hintz and Herting [15]. The popularity of this method at ASML is partly caused by the fact that the Hintz-Herting (HH) method is implemented in dynamic analysis software such as Ansys (as is also the case for the CB method), which is utilized at ASML. In contrast to the CB method, the HH method uses free-boundary vibration modes. Since for the free-boundary eigenvalue problem the boundary DOFs are not virtually constrained, the complete $\boldsymbol{M}^{(c)}$ and $\boldsymbol{K}^{(c)}$ matrices are used for the eigenvalue problem. Note that the undamped eigenvalue problem and the undamped eigenmodes are thus equal to those for the modal truncation method (Equation (2.41)):

$$\left(\boldsymbol{K}^{(c)} - {\omega_k^{(c)}}^2 \boldsymbol{M}^{(c)}\right) \boldsymbol{\phi}_k^{(c)} = \boldsymbol{0}. \tag{2.46}$$

For the reduction matrix, again a subset of the eigenmodes is collected in $\boldsymbol{\Phi}_{\mathcal{K}^{(c)}}^{(c)}$ which, for the Hintz-Herting technique, only includes non-rigid eigenmodes ($\omega_k^{(c)} \neq 0$). As has already been mentioned, the goal of CMS is to be able to retain the boundary DOFs explicitly.However, if $\boldsymbol{\Phi}_{\mathcal{K}^{(c)}}^{(c)}$ would directly be used in the reduction basis, this would not be the case, since $\boldsymbol{\phi}_k^{(c)}$ is non-zero at its boundary DOF related elements. The set of kept eigenvectors is therefore partitioned in a boundary and internal part ($\boldsymbol{\Phi}_{\mathcal{K}^{(c)},b}^{(c)}$ and $\boldsymbol{\Phi}_{\mathcal{K}^{(c)},i}^{(c)}$, respectively). To ensure that these modes do not influence the boundary DOFs, the dynamic information at the boundary DOFs is condensed to the internal DOFs using the constraint modes defined in Equation (2.44), which results in the so-called condensed vibration modes (CVM) [15]:

$$\boldsymbol{\Phi}_{CVM}^{(c)} = \boldsymbol{\Phi}_{\mathcal{K}^{(c)},i}^{(c)} - \boldsymbol{\Psi}_{const}^{(c)} \boldsymbol{\Phi}_{\mathcal{K}^{(c)},b}^{(c)}. \tag{2.47}$$

As mentioned, only non-rigid eigenmodes are used in Equation (2.47). Due to the free-boundary nature of the proposed eigenvalue problem, there is however a possibility that rigid body eigenmodes are present. These modes are therefore taken into account by inertia relief modes. This type of mode represents the response of the internal degrees of freedom under the influence of inertial effects on both the internal and boundary DOFs. As an example, when a substructure (which is free in space) has an external force applied to it, it will have rigid body motions. If this substructure is connected to a different (constrained) substructure however, these rigid body

modes are suppressed. Nevertheless, inertial effects will be induced on the assembled system by the rigid body eigenmodes in this case [21]. The displacements/rotations of the internal DOFs which are the result of these effects, are described by the set of inertia relief modes [15]:

$$\boldsymbol{\Phi}_{ir}^{(c)} = -\boldsymbol{K}_{ii}^{(c)^{-1}} \boldsymbol{M}_{ib}^{(c)} \boldsymbol{\Phi}_{0,b}^{(c)} - \boldsymbol{K}_{ii}^{(c)^{-1}} \boldsymbol{M}_{ii}^{(c)} \boldsymbol{\Psi}_{const}^{(c)} \boldsymbol{\Phi}_{0,b}^{(c)}, \tag{2.48}$$

where $\boldsymbol{\Phi}_{0,b}^{(c)}$ represents the boundary DOF partition of the rigid body eigenmodes. As shown in Equation (2.49), the displacements/rotations of the boundary DOFs associated to the inertia relief modes are again set to zero.

Besides the condensed vibration and inertia relief modes, which both represent dynamic mode contributions, the static modes are, as was the case for the Craig-Bampton method, given by constraint modes. Combining these three mode types, results in the reduction matrix for the Hintz-Herting method $\boldsymbol{T}_{HH}^{(c)}$, where the lower row again reads $\boldsymbol{u}_b^{(c)} = \boldsymbol{u}_b^{(c)}$:

$$\underbrace{\begin{bmatrix} \boldsymbol{u}_i^{(c)} \\ \boldsymbol{u}_b^{(c)} \end{bmatrix}}_{\boldsymbol{u}^{(c)}} \approx \underbrace{\begin{bmatrix} \boldsymbol{\Phi}_{CVM}^{(c)} & \boldsymbol{\Phi}_{ir}^{(c)} & \boldsymbol{\Psi}_{const}^{(c)} \\ \boldsymbol{0} & \boldsymbol{0} & \boldsymbol{I} \end{bmatrix}}_{\boldsymbol{T}_{HH}^{(c)}} \underbrace{\begin{bmatrix} \boldsymbol{q}_i^{(c)} \\ \boldsymbol{q}_{ir}^{(c)} \\ \boldsymbol{u}_b^{(c)} \end{bmatrix}}_{\hat{\boldsymbol{u}}^{(c)}}. \tag{2.49}$$

2.4 Demonstrator

Having discussed the theory needed to divide and reduce component models and to subsequently assemble them, in this section, an illustrative example of these techniques is given. For this, the cantilever beam from Section 2.2.4 is modeled using Euler elements. Due to this element-choice, there is one (perpendicular) displacement and one rotation degree of freedom at each node. Because of this, the structure is a multi-input multi-output (MIMO) system. A schematic representation of this beam is shown in Figure 2.5, where two components are distinguished by splitting the beam down the middle. In this figure, all nodes are indicated by (colored) dots. The blue dots indicate the nodes of the retained degrees of freedom (and thus the POIs), the green dots represent the interface nodes (which are typically also POIs), and the yellow dots are the internal nodes. The combination of the blue and green dots thus shows the nodes belonging to the set of boundary nodes. The red dot in component 1 is a constraint node of which, in this case, both degrees of freedom (displacement and rotation) are constrained. Therefore, these DOFs are not included in the system matrices of the first component. For that reason, these matrices of the first components have two rows/columns less than the system matrices for component 2. How the mass and stiffness matrices are constructed is explained in Appendix A.1. This appendix also gives more details on, among others, the parameters of the components.

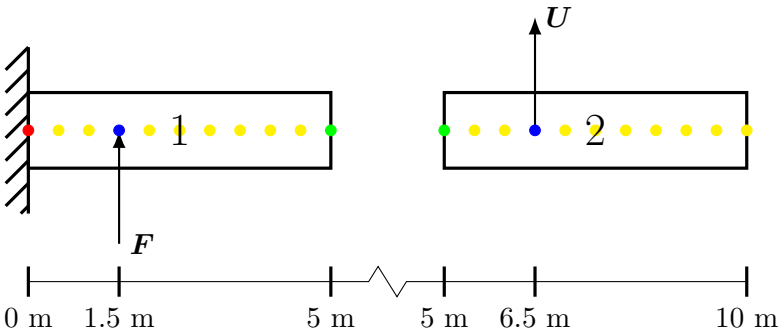

Figure 2.5: *Schematic representation of a two-component cantilever beam with input at component 1 and output at component 2. The nodes of each component are indicated by (color-coded) dots.*

Now that two component models are obtained, they are reduced using component mode synthesis. In this example, the Hintz-Herting method is used, because this method is used in the majority of this report. With respect to the amount of modes in the reduction bases of both components, since each node has two associated DOFs, both components have 2 interface DOFs and 2 retained DOFs, resulting in 4 boundary DOFs in total per component. Therefore, 4 constraint modes are used in each component reduction basis. If the second component is uncoupled, it is unconstrained and hence free in space. As a result, two rigid body motions are present for the second component (translation and rotation of the entire component). Therefore, two inertia relief modes are used in the reduction basis of the second component. Since the first component is fully constrained, the reduction basis for this component contains no inertia relief modes. Finally, it is chosen to use three condensed vibration modes with the lowest associated eigenfrequencies for each component. Hereto, the non-condensed eigenmodes used to obtain these condensed vibration modes, are shown in Figure 2.6. The amount of modes in each component is summarized per type in Table 2.1. This table also tabulates the total number of degrees of freedom in both the reduced and unreduced components. It should be noted that the amount of DOFs of a reduced model equals the total amount of modes in the reduction basis.

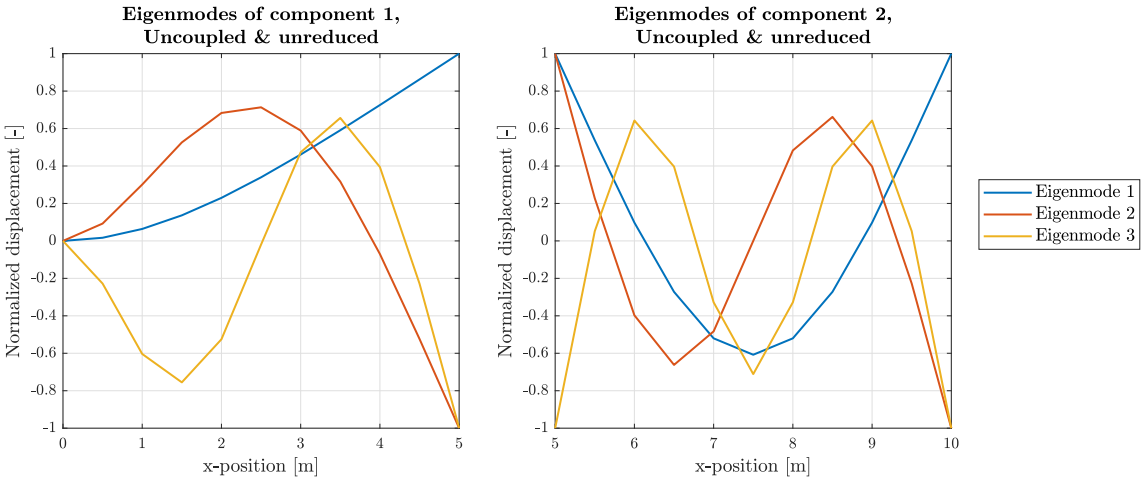

Figure 2.6: *First three undamped eigenmodes of the unreduced uncoupled (cantilever) beam components.*

Table 2.1: *Amount of DOFs for the unreduced/reduced individual components and assembled system. Also the amount of mode types per component reduction basis is tabulated.*

Number of:	Component 1	Component 2	Assembly
DOFs, unreduced	20	22	40
DOFs, reduced	7	9	14
Elastic modes	3	3	n.a.
Inertia relief modes	0	2	n.a.
Constraint modes	4	4	n.a.

In order to determine the frequency response function matrix (or receptance matrix) of a reduced/unreduced structure (which can either represent an assembly or component), Equations (2.50) and (2.51) are used [19]:

$$\boldsymbol{Y}(\omega j) = \boldsymbol{Z}^{-1}(\omega j) = \left(\boldsymbol{K} + \omega j \boldsymbol{D} - \omega^2 \boldsymbol{M}\right)^{-1}, \tag{2.50}$$

$$\hat{\boldsymbol{Y}}(\omega j) = \boldsymbol{T}\hat{\boldsymbol{Z}}^{-1}(\omega j)\boldsymbol{T}^T = \boldsymbol{T}\left(\hat{\boldsymbol{K}} + \omega j \hat{\boldsymbol{D}} - \omega^2 \hat{\boldsymbol{M}}\right)^{-1}\boldsymbol{T}^T. \tag{2.51}$$

Since in this research modal damping is assumed, the structural damping matrix is obtained by using an expression found in [9]:

$$\begin{aligned} \boldsymbol{D} &= 2\boldsymbol{\Phi}^{-T}\boldsymbol{\Phi}^T\boldsymbol{M}\boldsymbol{\Phi}\boldsymbol{\Xi}\boldsymbol{\Omega}\boldsymbol{\Phi}^{-1} \\ &= 2\boldsymbol{M}\boldsymbol{\Phi}\boldsymbol{\Xi}\boldsymbol{\Omega}\boldsymbol{\Phi}^{-1}, \end{aligned} \tag{2.52}$$

where $\boldsymbol{\Phi}$ represents the set of all undamped eigenvectors (obtained from Equation (2.41) or (2.46)), $\boldsymbol{\Omega}$ is a matrix with the angular eigenfrequencies corresponding to these eigenvectors on its diagonal, and $\boldsymbol{\Xi}$ is a diagonal matrix containing the modal damping parameters ξ_k. For now however, no damping is included yet.

Since $\boldsymbol{Y}(\omega j)$ represents the transfers from any degree of freedom to any other degree of freedom (or to itself), it is chosen to plot only one specific transfer for each component. In this example, these are the transfers from a force at the fourth node from the left (at $x = 1.5$ m for component 1, and $x = 6.5$ m for component 2) to the displacement at the same node for both components, as is shown in the small schematic representations of these components in the lower left corner of the plots. In terms of DOFs, this comes down to the transfers from the seventh DOF of each component to itself, where counting starts from the left and odd numbers represent translation-related DOFs and even numbers represent rotation-related DOFs. This numbering is used in (among others) Figure 2.7 and clarified in detail in Table A.4. The frequency response functions (FRFs) of these transfers are shown in Figure 2.7, where the magnitude of the transfer function can be interpreted as the amplification of the input (force) to the output (displacement) at specific frequencies.

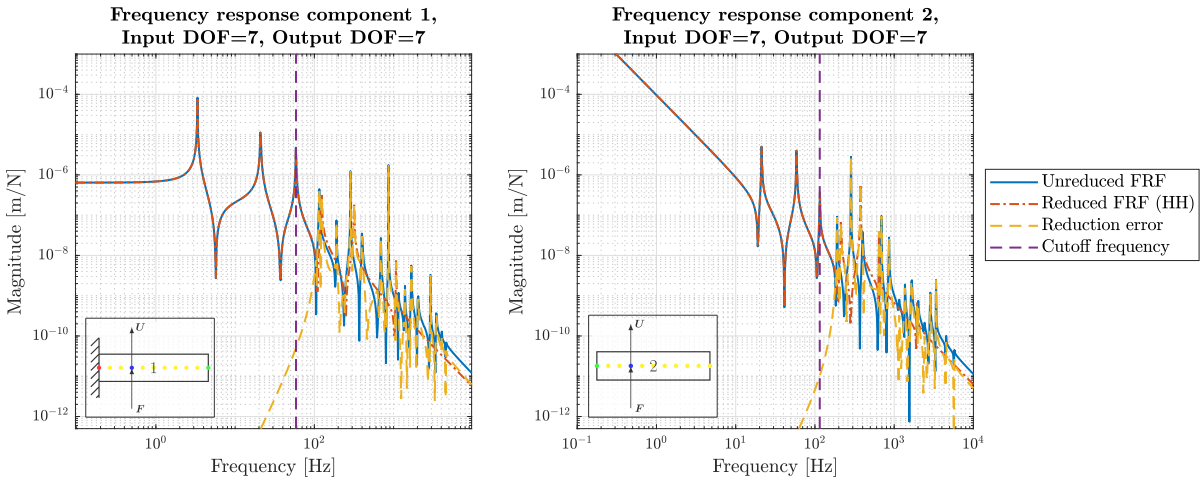

Figure 2.7: *Unreduced and reduced FRFs of the uncoupled components, where the displacement is measured at the same DOF as where the force is applied.*

In Figure 2.7, both the unreduced and reduced FRFs are shown. As is to be expected, below the cutoff frequency, the reduced and unreduced FRFs of both components are almost identical. This is also indicated by the reduction error (dashed yellow line), which is negligibly small below this frequency. These cutoff frequencies are defined as the highest eigenfrequency associated to the set of kept eigenvectors for the reduction basis of each component. It is also noted that, by using the Hintz-Herting method, the static information of all truncated modes is taken into account, resulting in statically correct FRFs (at the boundary DOFs).

When the (unreduced) FRFs of component 1 and 2 are compared, a few major dissimilarities are recognized. First of all, the most obvious difference is the low-frequent (or static) behavior. Since component 2 is free in space, the magnitude for $\omega \to 0$ tends to infinity. For the first component, this magnitude tends to a constant (flexibility) value however. Furthermore, the eigenfrequencies of component 2 are slightly higher.

To assemble the reduced components, Equation (2.8) is used to obtain $\hat{\boldsymbol{M}}^{(assy)}$ and $\hat{\boldsymbol{K}}^{(assy)}$. By using Equations (2.50) and (2.51), the reduced and unreduced receptance matrices of the assembled system are obtained. In Figure 2.8, the reduced and unreduced FRFs of the transfer from a force at component 1 to a displacement at component 2, as is indicated in Figure 2.5 (as well as the schematic beam in the lower left corner), are plotted.

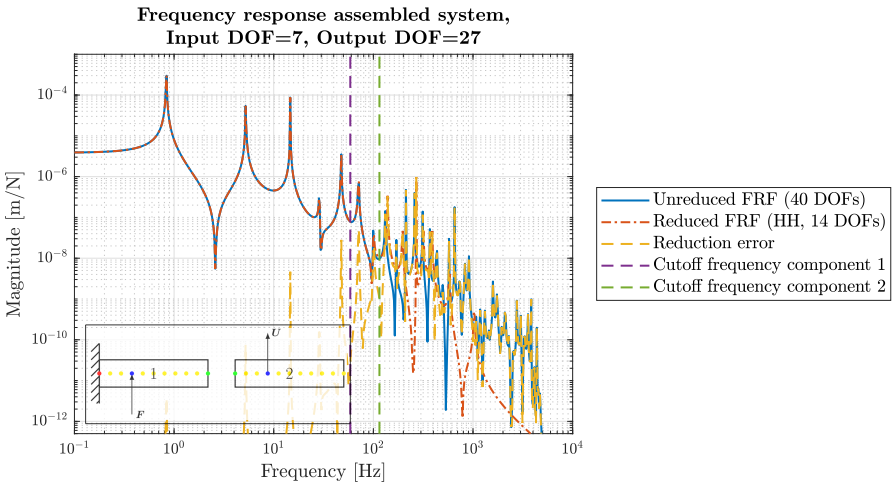

Figure 2.8: *Unreduced and reduced FRFs of the assembled system, where the measured displacement and applied force are non-colocated.*

Figure 2.8 shows that, similar to component 1, the magnitude of the FRF of the assembly is approximately constant for frequencies below the first eigenfrequency. This is again caused by the fact that the assembled system is constrained at one end. Additionally, it can be seen that below the lowest cutoff frequency of both components, the reduced FRF of the assembly is almost identical to the unreduced FRF. Above the cutoff frequency of component 1, the reduction error becomes less accurate and especially above the cutoff frequency of component 2, the response is approximated relatively poorly by the reduced assembly model. This is however exactly what should be expected, and since in practice the high-frequency behavior is often not of interest (as a result of, for instance, the high-frequent roll-off and disturbances), the reduction applied here is acceptable.

Chapter 3

Error bound propagation

The goal of this thesis is to find which component eigenmodes should be kept in the component reduction bases, such that the reduction quality of the assembly is improved. To achieve this, the quality of the reduced assembly should be determined for multiple reduction bases, which contain different (combinations of) eigenmodes. In this chapter, the aim is to assess this quality by analyzing the propagation of bounds on the reduction errors of components through an assembly. By doing this, an upper bound on the assembly error, which is induced by these component errors, is obtained. Since this upper bound serves as an estimate of the exact assembly reduction error, the estimates which are obtained by using different reduction bases, can be compared to find which reduction bases induce the most accurate reduced assembly. One of the advantages of this approach is that the assembly error can be linked to component errors, which allows for goal-oriented improvement of the reduced models of specific components.

In order to find an expression for the propagated errors, this chapter uses the feedback representation as introduced in Section 2.2.4. In Section 3.1, the expression for the above mentioned upper bound on the error is introduced. Also, the small gain condition, which needs to be satisfied in order to be able to use this bound, is discussed in this section. Afterwards, the topics discussed in the first section are implemented and analyzed. Finally, a discussion on the general applicability of this theory on different types of systems is given.

The theory discussed in this chapter is based on the work of Besselink [1, 2]. In his work, Besselink investigated a feedback system consisting of one reduced linear subsystem and one unreduced non-linear subsystem. In this thesis, the methods introduced in [2] are however implemented to a system consisting out of two linear subsystems which are both reduced. Furthermore, in this thesis, the in- and output are non-colocated, whereas Besselink used a colocated system. This thesis thus provides, in that sense, an extension to the theory discussed by Besselink [2].

3.1 Framework for error bound

In this section, the small gain condition and an expression for the bound on the assembly error as a result of reduction errors in the uncoupled components are introduced. As already mentioned, the (control theory inspired) feedback representation of a 2-component system will be used for this purpose. A system diagram of such a system is recapitulated in Figure 3.1a. Here, it should be remembered that, as was already mentioned in Section 2.2.4, the transfer function matrices

in the diagrams of Figure 3.1 can represent different types of (MIMO) transfer functions. A reduced variant of the feedback representation is given by Figure 3.1b. Here, both systems are reduced, where the reduced variables and transfer functions are indicated by a hat.

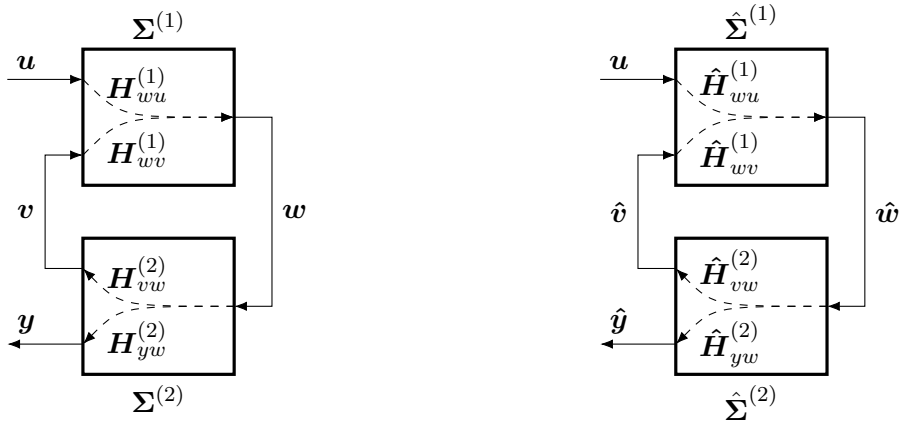

(a) *Subsystems 1 & 2 unreduced.*

(b) *Subsystems 1 & 2 reduced.*

Figure 3.1: *Reduced and unreduced system representations of two coupled subsystems ($\boldsymbol{\Sigma}^{(1)}$ and $\boldsymbol{\Sigma}^{(2)}$) in a feedback representation, where the input and output are located at different subsystems.*

3.1.1 Small gain condition

Originally, the small gain condition is a notion from control theory which is used to check stability of a feedback system. This condition serves as a relatively easy-to-check conservative alternative to the Nyquist criterion. Since this condition also needs to be satisfied in order to use the upper bound on the assembly error which is introduced in Section 3.1.2, this condition is presented for a system written in feedback form as introduced in Section 2.2.4. Based on the work of Skogestad and Postlethwaite [28], the small gain condition is defined as

$$\gamma^{(1)}_{wv}\gamma^{(2)}_{vw} < 1. \tag{3.1}$$

A derivation of this condition is given in Appendix B.1. In Equation (3.1), $\gamma^{(c)}$ denotes the $\mathcal{H}_\infty$-norm of a transfer function matrix ($\gamma^{(c)}_{ij} := \|\boldsymbol{H}^{(c)}_{ij}\|_\infty$). Since the $\mathcal{H}_\infty$-norm represents the maximal amplification of a transfer function matrix, this norm can be regarded as an upper bound on the amplification of the transfer function matrix. As is explained in Appendix C.2.2, this maximal amplification equals the highest induced 2-norm of the transfer function matrix, evaluated over the frequency. Due to the use of the $\mathcal{H}_\infty$-norms for the transfer functions related to the feedback loop ($\boldsymbol{H}^{(1)}_{wv}$ and $\boldsymbol{H}^{(2)}_{vw}$), the small gain condition evaluates if, in a worst-case scenario, the signal going through the feedback loop will become smaller over time, such that the response of the feedback system will not explode.

Because of the use of $\mathcal{H}_\infty$-norms, the small gain condition presented here is conservative and hence merely a sufficient condition for stability of the closed-loop system. Not satisfying the condition does therefore not directly imply instability. This conservatism is partly caused by the fact that $\gamma^{(1)}_{wv}$ and $\gamma^{(2)}_{vw}$ represent the maximal amplification induced by their associated transfer function matrices (evaluated over the frequency). It is however likely that these maximal amplifications are not located at the same frequency for both subsystems. Nevertheless, the product of $\gamma^{(1)}_{wv}$ and $\gamma^{(2)}_{vw}$ assumes a worst-case scenario in which it is assumed that these maximal

amplifications are located at the same frequency. Furthermore, phase information is neglected by this condition. This can be easily illustrated in a SISO context; in the classical Nyquist criterion, where the (-1,0) point in the complex plane should be avoided, the amplitude is allowed to be larger than one (outside the unit disk), as long as this high amplitude corresponds to the correct phase angle. The small gain condition however states that the largest amplitude should always be smaller than one (inside the unit disk), regardless of the phase, making it impossible to encircle the (-1,0) point. Hence, satisfying the (conservative) small gain condition, guarantees stability.

An advantage of the use of $\mathcal{H}_\infty$-norms of the transfer functions is that it enables the use of the small gain condition in a non-linear context as well, as is shown by Besselink [2]. Since this research is confined to linear systems, non-linear applications of this theorem will not be discussed in this thesis. A second advantage of the use of upper bounds which can be exploited in this research is that this is more attractive from a computational point of view; instead of calculating the small gain condition at each frequency as proposed by Skogestad and Postlethwaite [28], the condition in Equation (3.1) is only evaluated once.

3.1.2 Upper bound on assembly error

By using the feedback representation, an upper bound on the reduction error of an assembly can be determined. This upper bound has already been derived by Besselink for a class of non-linear systems (for which incremental bounds [23] are used). In this section, such a bound is introduced for a system in which both linear subsystems are reduced and the in- and output are non-colocated.

The bound on the reduction error, as is given below, is actually given by a bound on the gain/amplification of the input, which results in a bound on the error of the output. To be exact, this 'error gain bound' gives, for some $\mathcal{L}_2$-norm of the input ($\|\boldsymbol{u}\|_2$), an upper bound on the $\mathcal{L}_2$-norm of the reduction error of the output ($\|\boldsymbol{\delta y}\|_2$):

$$\|\boldsymbol{\delta y}\|_2 = \|\boldsymbol{y} - \hat{\boldsymbol{y}}\|_2 \leq \bar{\varepsilon}_{yu}^{(assy)} \|\boldsymbol{u}\|. \tag{3.2}$$

Here, $\bar{\varepsilon}_{yu}^{(assy)}$ represents the aforementioned error gain bound, of which an expression is obtained by performing similar derivations as in [2]. The expression for the error bound of the specific system configuration used in this thesis, is given by Equation (3.3):

$$\begin{aligned}\bar{\varepsilon}_{yu}^{(assy)} = {} & \varepsilon_{yw}^{(2)} \left(1 - \gamma_{wv}^{(1)}\gamma_{vw}^{(2)}\right)^{-1} \gamma_{wu}^{(1)} + \hat{\gamma}_{yw}^{(2)} \left(1 - \hat{\gamma}_{wv}^{(1)}\hat{\gamma}_{vw}^{(2)}\right)^{-1} \dots \\ & \cdot \left(\varepsilon_{wu}^{(1)} + \varepsilon_{wv}^{(1)}\gamma_{vw}^{(2)} \left(1 - \gamma_{wv}^{(1)}\gamma_{vw}^{(2)}\right)^{-1} \gamma_{wu}^{(1)} + \hat{\gamma}_{wv}^{(1)}\varepsilon_{vw}^{(2)} \left(1 - \gamma_{wv}^{(1)}\gamma_{vw}^{(2)}\right)^{-1} \gamma_{wu}^{(1)}\right),\end{aligned} \tag{3.3}$$

which is derived in Appendix B.2. The most important steps in this derivation are:

- Using the $\mathcal{H}_\infty$-norm to determine the upper bound on transfer functions and errors of transfer functions (see Appendix C.2.2 for a detailed explanation hereof).
- Utilizing the triangle inequality to write norms of a sum of variables as the sum of the individual norms of these variables (see Appendix C.2.1 for a definition of this inequality).
- Separating a reduction error caused by reduced transfer function and reduced inputs in two separate terms where one term is related to the error caused solely by using the reduced transfer function and the other term is related to the error solely caused by the reduced input (see Appendix C.2.3 for an elaborate explanation).

In Equation (3.3), $\varepsilon^{(c)}$, $c \in \{1, 2\}$, denotes the $\mathcal{H}_\infty$-norm of the reduction error of a specific transfer function matrix ($\varepsilon^{(c)} = \|\boldsymbol{H}^{(c)}(s) - \hat{\boldsymbol{H}}^{(c)}(s)\|_\infty$). Furthermore, it can be recognized that the upper bounds of the reduction errors of specific transfer functions ($\varepsilon^{(c)}$) are propagated through the system by pre- and post-multiplying them with bounds on the transfer functions of the unreduced and/or reduced uncoupled components ($\gamma^{(c)}$ and $\hat{\gamma}^{(c)}$, respectively).

One of the terms which is used for this propagation is given by $\left(1 - \gamma_{wv}^{(1)}\gamma_{vw}^{(2)}\right)^{-1}$ and is recognized as a common artifact of transfer functions of closed-loop feedback systems. Because of the inverse in this term, $\gamma_{wv}^{(1)}\gamma_{vw}^{(2)}$ is not allowed to equal one, since otherwise $\bar{\varepsilon}_{yu}^{(assy)}$ would be unbounded. This restriction is related to the small gain condition; if $\gamma_{wv}^{(1)}\gamma_{vw}^{(2)} = 1$, the small gain condition is not satisfied. Also note that the small gain should hold for the reduced system as well, as is required by the term $\left(1 - \hat{\gamma}_{wv}^{(1)}\hat{\gamma}_{vw}^{(2)}\right)^{-1}$ in Equation (3.3).

As can be seen in the extensive derivation of Equation (3.3) in Appendix B.2, Equations (3.2) and (3.3) implicitly use a lot of (stacked) inequalities. Due to the stacking of these inequalities, $\bar{\varepsilon}_{yu}^{(assy)}$ can be rather restrictive. As a simple example, suppose $a \geq b \geq c \geq d \geq e$, it is then rather likely that $a \gg e$. With each additional (stacked) inequality, $\bar{\varepsilon}_{yu}^{(assy)}$ thus becomes less tight. Furthermore, by using $\mathcal{H}_\infty$-norms, a worst-case scenario is obtained which makes the inequality (very) conservative. In other words, the found error gain bound may be much larger than the actual error gain. Therefore, proper interpretation and a fair comparison of the reduction errors for various reduction bases, based on $\bar{\varepsilon}_{yu}^{(assy)}$ (as is the intended goal of this approach), might not be possible. This is investigated in the following sections of this chapter.

As mentioned by Besselink [2], γ, ε, and $\hat{\gamma}$ are related to each other by

$$\gamma^{(c)} + \varepsilon^{(c)} \geq \hat{\gamma}^{(c)}. \tag{3.4}$$

By exploiting this relation, Equation (3.3) can be written in an alternative form:

$$\begin{aligned}\bar{\varepsilon}_{yu,alt} = {} & \varepsilon_{yw}^{(2)}\left(1 - \gamma_{wv}^{(1)}\gamma_{vw}^{(2)}\right)^{-1}\gamma_{wu}^{(1)} + \left(\gamma_{yw}^{(2)} + \varepsilon_{yw}^{(2)}\right)\left(1 - \left(\gamma_{wv}^{(1)} + \varepsilon_{wv}^{(1)}\right)\left(\gamma_{vw}^{(2)} + \varepsilon_{vw}^{(2)}\right)\right)^{-1}\dots \\ & \cdot\left(\varepsilon_{wu}^{(1)} + \varepsilon_{wv}^{(1)}\gamma_{vw}^{(2)}\left(1 - \gamma_{wv}^{(1)}\gamma_{vw}^{(2)}\right)^{-1}\gamma_{wu}^{(1)} + \left(\gamma_{wv}^{(1)} + \epsilon_{wv}^{(1)}\right)\varepsilon_{vw}^{(2)}\left(1 - \gamma_{wv}^{(1)}\gamma_{vw}^{(2)}\right)^{-1}\gamma_{wu}^{(1)}\right),\end{aligned} \tag{3.5}$$

where no information about the reduced system is required anymore. This is particularly useful if a reduction method is used which gives an a priori estimate of the error (e.g., balanced truncation [3] or optimal Hankel norm approximation [12]), since the reduced system does not have to be determined anymore then. Although using an a priori estimate for the error is a more efficient way to determine a bound on the reduction error of the assembly, it comes at the cost of an additional decrease in the tightness of the assembly error bound (due to an increased level of conservatism caused by the use of the inequality given in Equation (3.4)). Furthermore, if components are reduced using CMS techniques (as is intended in this research), there is no a priori estimate of the error. Therefore, the use of Equation (3.5) has no advantages and merely comes at the cost of an additional loss in tightness of the error bound. It is therefore not advised to use Equation (3.5) in the context of reduction using component mode synthesis.

In case a system with only a single reduced subsystem is to be analyzed, Equation (3.5) proves to be useful however. For instance, if only $\boldsymbol{\Sigma}^{(1)}$ is reduced, an expression for the bound on the reduction error gain is simply obtained from Equation (3.5) by setting $\varepsilon_{yw}^{(2)}$ and $\varepsilon_{vw}^{(2)}$ to zero (since subsystem 2 is unreduced, the (bound on the) reduction errors related to $\boldsymbol{\Sigma}_2$ are zero):

$$\bar{\varepsilon}_{yu,alt}^{(assy)} = \gamma_{yw}^{(2)}\left(1 - \left(\gamma_{wv}^{(1)} + \varepsilon_{wv}^{(1)}\right)\gamma_{vw}^{(2)}\right)^{-1}\left(\varepsilon_{wu}^{(1)} + \varepsilon_{wv}^{(1)}\gamma_{vw}^{(2)}\left(1 - \gamma_{wv}^{(1)}\gamma_{vw}^{(2)}\right)^{-1}\gamma_{wu}^{(1)}\right). \tag{3.6}$$

Note that, although similar, this error bound deviates slightly from the error bound found in [2] due to the non-colocated configuration of the in- and output of the system investigated in this thesis. This equation can also be translated back to a (somewhat tighter) form including reduced transfer function bounds by substituting $\left(\gamma_{wv}^{(1)} + \varepsilon_{wv}^{(1)}\right)$ by $\hat{\gamma}_{wv}^{(1)}$. Of course, a similar procedure can be used in case only subsystem 2 is reduced.

3.2 Applicability

In this section, the framework discussed in the previous section is applied to the model of the cantilever beam, which was discussed in Section 2.4. Here, it is shown that there are already limitations on the applicability of this framework for a relatively simple example. These limitations are discussed in Section 3.2.1. Afterwards, some techniques are presented that show how, using the knowledge of these limitations, a small gain compatible system can be obtained. For the reduced model of the cantilever beam, the (Hintz-Herting) reduced model defined in Section 2.4 is used.

3.2.1 Limitations

For the demonstrator cantilever beam which was put in feedback representation form in Section 2.2.4, the small gain condition is not satisfied. Because of this, the error bound propagation approach can not be used. The reason for why the condition is not satisfied, is explained with the aid of Figure 3.2. This figure shows the magnitude of the translation-related elements (force-to-displacement/displacement-to-displacement/displacement-to-force) of the relevant unreduced transfer functions as used for Equation (3.3). Also, the magnitude of the translation-related element of $\boldsymbol{H}_{wv}^{(1)}\boldsymbol{H}_{vw}^{(2)}$ (which is also referred to as the loop gain) is plotted (in black). Clearly, the maximal amplitude of this element of $\boldsymbol{H}_{wv}^{(1)}\boldsymbol{H}_{vw}^{(2)}$ is much larger than 1 for multiple frequency ranges. With this knowledge, it makes sense that a conservative bound on this loop gain (given by $\gamma_{wv}^{(1)}\gamma_{vw}^{(2)}$) is also larger than 1, which results in not satisfying the small gain condition. Since, for this example, this bound equals approximately 5.53×10^{10}, the small gain condition is indeed not met.

Although the transfer functions plotted in Figure 3.2 only show a single element of the transfer functions, these are very useful for explaining the cause of the limitations on the applicability of the error bound for this case study. Namely, the magnitude of the elements of the transfer function matrices give a reasonable estimate of the (order of magnitude of the) matrix gain. It can thus be stated that the maximal magnitude of the translation-related element of the loop gain being larger than 1 does not guarantee stable behavior.

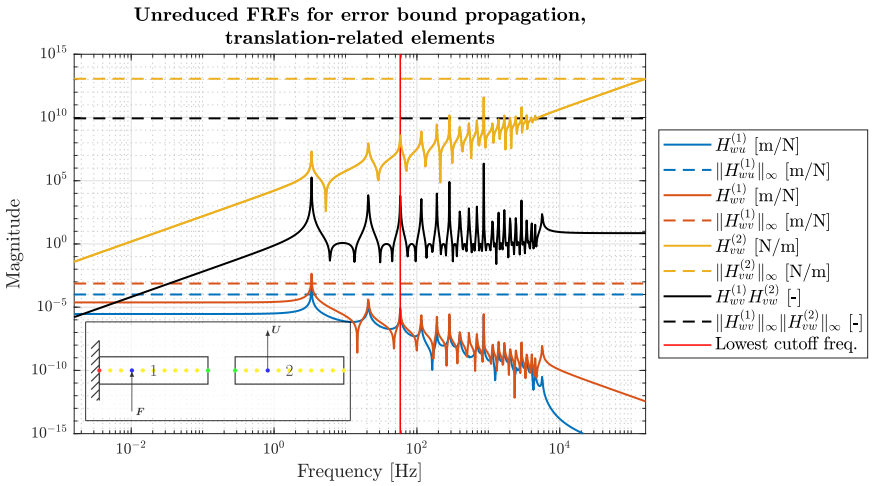

Figure 3.2: *Translation-related elements of unreduced transfer function matrices as used for the error bound propagation. The translation-related element of the loop gain matrix is shown in black.*

Analyzing Figure 3.2 more thoroughly, a few causes for the high value of $\gamma_{wv}^{(1)}\gamma_{vw}^{(2)}$ can be identified, which are listed below.

- **Infinite high-frequency gains:**
  For $\boldsymbol{H}_{vw}^{(2)}$, which represents the dynamic stiffnesses of the interface of component 2 ($\boldsymbol{H}_{vw}^{(2)} = -{\boldsymbol{Y}_{ff}^{(2)}}^{-1}$), the high-frequency gain grows with a +2 slope. When calculating the $\mathcal{H}_\infty$-norm of this transfer function matrix, a (very) high value is found which is related to the increased gains for high frequencies. In theory, this bound would even be infinite. Due to this 'infinite' upper bound, $\gamma_{wv}^{(1)}\gamma_{vw}^{(2)}$ becomes infinite as well, which clearly indicates potential instability, albeit solely a consequence of the combination of the high-frequency +2 slope and the use of the $\mathcal{H}_\infty$-norm.

- **Resonance peaks:**
  A similar, but less severe cause is the presence of resonance peaks. Due to these (sharp) peaks, the upper bound on the transfer function is relatively large. This is for example seen in Figure 3.2, where $\boldsymbol{H}_{wv}^{(1)}[1,1]$ has a resonance peak at 3.35 Hz which significantly increases its upper bound $\|\boldsymbol{H}_{wv}^{(1)}[1,1]\|_\infty$ with respect to the low-frequency static magnitude. Here, $[1,1]$ denotes the force-to-displacement element of $\boldsymbol{H}_{wv}^{(1)}$.

- **Similarity in dynamic stiffness levels:**
  Finally, there is also an effect of the similarity of $\boldsymbol{Y}_{ff}^{(1)}$ and $\boldsymbol{Y}_{ff}^{(2)}$ for mechanical systems with comparable (dynamic) stiffness levels. Due to the definition of the transfer functions ($\boldsymbol{H}_{wv}^{(1)} = \boldsymbol{Y}_{ff}^{(1)}$ and $\boldsymbol{H}_{vw}^{(2)} = -{\boldsymbol{Y}_{ff}^{(2)}}^{-1}$), if $\boldsymbol{Y}_{ff}^{(1)} \approx \boldsymbol{Y}_{ff}^{(2)}$, the absolute value of the product of $\boldsymbol{H}_{wv}^{(1)}$ and $\boldsymbol{H}_{vw}^{(2)}$ is approximately equal to unity. In practice, this is not the case due to small dissimilarities, but it can be recognized from Figure 3.2 that the magnitude of the black line lies relatively close to 10^0 for most frequencies.

  Therefore, the magnitude of one or both of these transfer functions needs to be lowered such that the black line lies below 10^0. For example, lowering the dynamic stiffness of component 2, will lead to a lower magnitude of $\boldsymbol{H}_{vw}^{(2)}$. Similarly, increasing the dynamic stiffness of component 1 leads to a lower receptance and hence a lower magnitude of $\boldsymbol{H}_{wv}^{(1)}$. Both approaches result in lower loop transfers, making it more feasible to satisfy the small

gain condition. Here, it is important to understand that, because of the inverse relation between the transfer function and the receptance of component 2, either increasing or decreasing the dynamic stiffnesses of both components simultaneously, will not affect the value of $\boldsymbol{H}_{wv}^{(1)}\boldsymbol{H}_{vw}^{(2)}$ or $\gamma_{wv}^{(1)}\gamma_{vw}^{(2)}$.

Although for the explanation given here, the unreduced transfer functions have been used, equivalent phenomena and problems are observed for their reduced variants and the 'reduced' small gain condition ($\hat{\gamma}_{wv}^{(1)}\hat{\gamma}_{vw}^{(2)} < 1$).

3.2.2 Small gain compatible system

Having discussed the limitations that the small gain condition imposes on the applicability of the error bound propagation method, this section proposes a technique which changes the system representation slightly such that the small gain condition is easier to satisfy. Furthermore, two techniques are discussed with which a different 'small gain compatible' system can be obtained. Since these latter two techniques fundamentally change the system, these techniques are merely presented to investigate what the requirements for a system are in order to satisfy the small gain condition.

First of all, to negate the effect of the infinite high-frequency upper bound on a transfer function due to its high-frequency +2 slope (as discussed at the first bullet in Section 3.2.1), filtering is used. By using an appropriate filter $C(\omega j)$ to redefine the transfer functions as the original transfer function multiplied with (the inverse of) $C(\omega j)$ as shown in Figure 3.3, the effect of the high-frequency +2 slope can be negated.

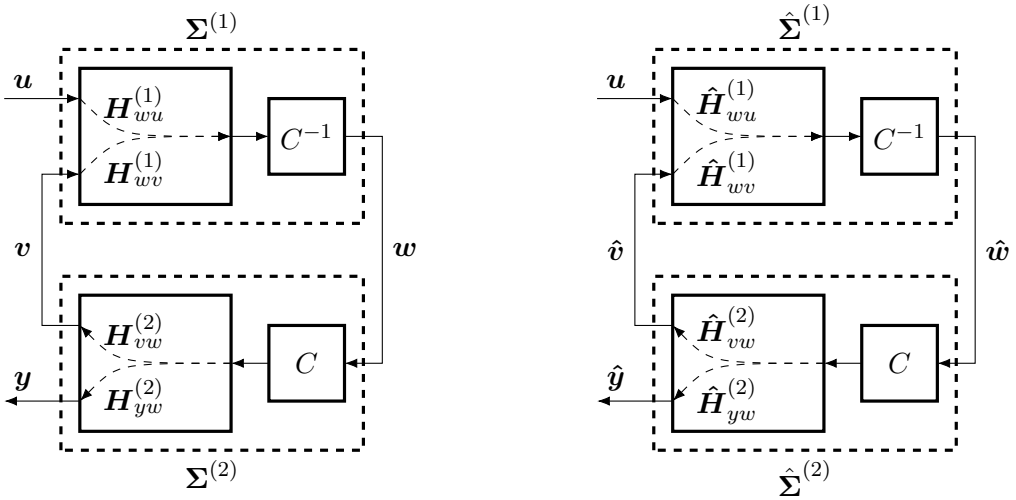

(a) *Subsystems 1 & 2 unreduced.*

(b) *Subsystems 1 & 2 reduced.*

Figure 3.3: *Reduced and unreduced system representations of two coupled subsystems ($\boldsymbol{\Sigma}^{(1)}$ and $\boldsymbol{\Sigma}^{(2)}$) in a feedback representation with filtering, where the input and output are located at different subsystems.*

In this research, a second-order low-pass filter, defined as

$$C(\omega j) = \frac{k_{LP}}{\frac{1}{(2\pi f_{LP})^2}(\omega j)^2 \frac{2\beta}{2\pi f_{LP}}(\omega j) + 1}, \quad \omega \in \mathbb{R}, \tag{3.7}$$

where $f_{LP} = 3.34$ Hz, $k_{LP} = 1$, and $\beta = 1$, is used for this purpose. Here, β is chosen such that

no additional resonance peak is imposed by the filter and $k_{LP} = 1$ ensures that the static behavior is not altered. Furthermore, by choosing f_{LP} at the lowest eigenfrequency of both components, the -2 slope of the low-pass filter only acts from this eigenfrequency to $\omega = \infty$. Hereby, the filter neutralizes the +2 slope (which approximately starts at the lowest eigenfrequency) of for example $\boldsymbol{H}_{vw}^{(2)}$ in Figure 3.2, while not amplifying the magnitudes below the first eigenfrequency.

For the system presented in thesis, only adding such filtering does however not suffice to satisfy the small gain condition. Therefore, two additional methods are discussed which explain how the (sub)system(s) can be fundamentally changed in order to meet the small gain condition.

First of all, to abate the effect of the resonance peaks on the upper bound, damping can be added. Due to damping, resonance peaks are less sharp and high in magnitude. As a consequence, the $\mathcal{H}_\infty$-norm is much lower, leading to decreased values of $\gamma_{wv}^{(1)}\gamma_{vw}^{(2)}$ and $\hat{\gamma}_{wv}^{(1)}\hat{\gamma}_{vw}^{(2)}$. For the particular example shown in this section, modal damping is applied on both components separately, where all modes are damped equally with a modal damping factor of 0.10. It should be remarked that a modal damping factor of 0.10 is relatively high, but, for this particular example, this is needed in order to be able to meet the small gain condition.

Additionally, as already discussed at the last bullet in Section 3.2.1, the levels of the loop transfer functions of both components can be changed in such a way that the loop gain (which is the product of the dynamic stiffness of component 2 and its inverse of component 1) becomes smaller. To illustrate this, the parameters of component 2 were altered such that the small gain condition is met (where the above mentioned filtering and damping techniques are already implemented). The parameters for both components, obtained after tuning, are tabulated in Table 3.1.

Table 3.1: *Tuned parameters for both components of a 'small gain compatible' two-component cantilever beam.*

Parameter	Unit	Component 1	Component 2
Density	$\mathrm{kg/m^3}$	7.850×10^{3}	7.850×10^{-1}
Cross-sectional area	$\mathrm{m^2}$	1×10^{-2}	1×10^{-6}
Area moment of intertia	$\mathrm{m^4}$	$1/12\times10^{-4}$	$1/12\times10^{-4}$
Young's modulus	$\mathrm{N/m^2}$	2.1×10^{11}	2.1×10^{11}
Length	m	5	5

Using all three of the previously mentioned techniques, a plot similar to that of Figure 3.2 is given by Figure 3.4. In this figure, the effects of the filtering and damping can clearly be recognized by the high-frequency horizontal line and the relatively smooth resonance peaks, respectively. Also, the parameter variation of component 2 can be recognized by the overall magnitude of $\boldsymbol{H}_{vw}^{(2)}$ which has been lowered by a factor of 10^{-8} with respect to Figure 3.2. Also, the first resonance peak of $\boldsymbol{H}_{vw}^{(2)}$, is shifted towards a much higher frequency due to the decreased mass of the second component.

As the black line in Figure 3.4 shows, the (translation-related element of the) loop gain of the small gain compatible system is smaller than 1 for all frequencies. Calculating $\gamma_{wv}^{(1)}\gamma_{vw}^{(2)}$ shows that the bound on the loop gain is also smaller than one (namely 0.552, see Table 3.2). Note that, due to its implicit conservatism, $\gamma_{wv}^{(1)}\gamma_{vw}^{(2)}$ is larger than the highest peak of $\boldsymbol{H}_{wv}^{(1)}\boldsymbol{H}_{vw}^{(2)}$.

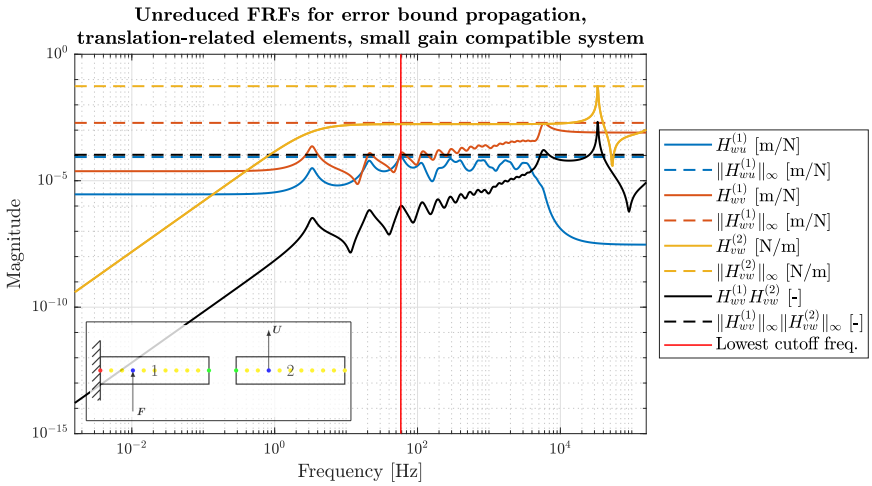

Figure 3.4: *Translation-related elements of unreduced transfer function matrices as used for the error bound propagation, for the small gain compatible system. Also, the loop gain is shown for all frequencies.*

The values for $\gamma_{wv}^{(1)}\gamma_{vw}^{(2)}$ for the systems shown in Figures 3.2 and 3.4, indicating satisfaction of the small gain condition for the case in Figure 3.4, are given in Table 3.2. Furthermore, this table shows the value of the actual bound on the reduction error gain ($\|\boldsymbol{E}_{yu}^{(assy)}\|_\infty = \|\boldsymbol{Y}_{yu}^{(assy)} - \hat{\boldsymbol{Y}}_{yu}^{(assy)}\|_\infty$). Also, the upper bound on the assembly error gain as given by Equation (3.3) is tabulated. For the original system, the upper bound does not exist since, for this case, $\gamma_{wv}^{(1)}\gamma_{vw}^{(2)} \gg 1$. For the small gain compatible system the error bound calculated using Equation (3.3) is however a valid upper bound for $\|\boldsymbol{E}_{yu}^{(assy)}\|_\infty$. Table 3.2 shows that this error bound is approximately a factor 6×10^6 higher than the actual error. This upper bound thus provides a very conservative bound, as was already expected due to the stacked inequalities and $\mathcal{H}_\infty$-norms. Therefore, this upper bound should not be used as an accurate and reliable estimate for the assembly reduction error.

Most importantly, however, by adding damping and tuning the subsystem parameters, the small gain compatible system is fundamentally different from the original system. Looking at the parameters in Table 3.1, it should also be noted that this 'small gain compatible' system has almost no realistic physical interpretation. These techniques should therefore not be seen as a solution, but as a tool that shows why the small gain condition is not met for a 'normal' system and what has to be changed in order for it to do.

Table 3.2: *Bound on the loop gain, maximal assembly reduction error gain and upper bound on the assembly reduction error gain for the original cantilever beam system and a small gain compatible cantilever beam system.*

Variable	Unit	Original system	Small gain compatible system
$\gamma_{wv}^{(1)}\gamma_{vw}^{(2)}$	-	$5.53\times10^{10} \not< 1$	$5.52\times10^{-1} < 1$
$\|\boldsymbol{E}_{yu}^{(assy)}\|_\infty$	m/N	4.38×10^{-4}	6.23×10^{-7}
$\bar{\varepsilon}_{yu}^{(assy)}$	m/N	n.a.	1.00×10^{-1}

3.3 Alternative applications

In Section 3.2, it was explained that for the two-component cantilever beam (introduced in Section 2.4), the small gain condition does not hold, even if filtering techniques are applied. Also, it became clear that only specific systems satisfy this condition. In this section, this statement is investigated in further detail. Hereto, we study a similar cantilever beam, but now with a spring-damper attached in the middle. Figures 3.5 and 3.6 show how such a system can be split into two subsystems in several ways; Figure 3.5 shows a system where the beam is split in two components, but now with a spring-damper directly attached to the right part of the beam. In Figure 3.6, the interface is defined between the entire cantilever beam and a separate spring-damper. Both representations have the same input (force) and output (displacement), which are located at $x = 1.5$ m and at $x = 5$ m, respectively. Note that this is slightly different from the location of the output as previously used.

When analyzing these two systems using the framework developed in this chapter, the relevant transfer functions for the feedback representation, as shown in Figure 3.1, are assumed to be known. The reduced model of the spring-damper substructure is modeled as a 'perfect' theoretical spring-damper, where k_d and d_d are both chosen as unity. Therefore, the reduced receptance of the spring-damper is given by:

$$\hat{Y}_{SD}(\omega j) = \frac{1}{d_d \omega j + k_d}. \tag{3.8}$$

Since adding a (small) 'disturbance' to this reduced model results in a receptance with more detail, this receptance can be used as the unreduced receptance of the spring-damper:

$$Y_{SD}(\omega j) = \hat{Y}_{SD}(\omega j) + disturbance(\omega j). \tag{3.9}$$

Because the disturbance only changes the behavior of the perfect spring-damper slightly, Equation (3.8) gives a good approximation of the 'disturbed' model and can therefore be regarded as a reduced model. Although this approach does not use a physically realistic unreduced spring-damper model, for convenience, it is opted to use this approach since this example only serves as a simple demonstration of the applicability of the error bound propagation method. In the analyses given below, both damping (modal, 10%) and filtering (second-order low-pass) have been applied.

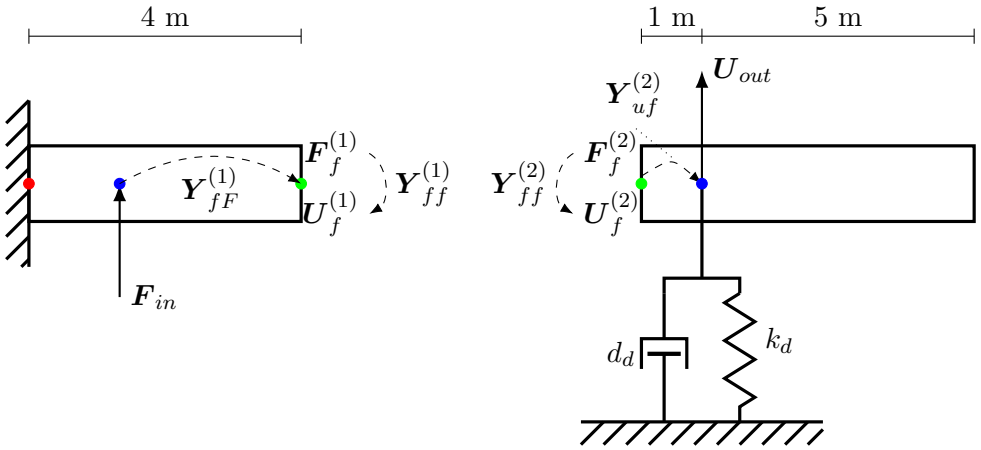

Figure 3.5: *Schematic representation of a substructured cantilever beam with an attached damper. The input is located at the left beam component and the output at the right beam component. Relevant forces, displacements, and transfer functions are also indicated.*

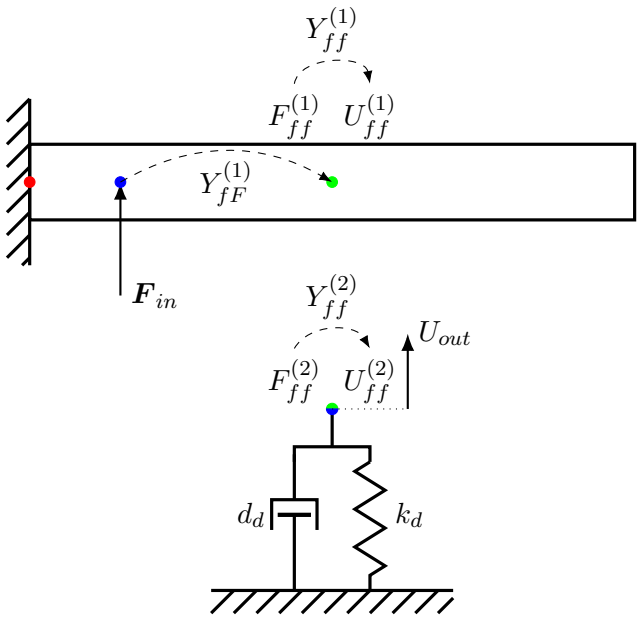

Figure 3.6: *Schematic representation of a substructured cantilever beam with a separated damper. The input is located at the beam subsystem and the output at the spring-damper subsystem. Relevant forces, displacements, and transfer functions are also indicated.*

For the system depicted in Figure 3.5, the small gain condition is again not satisfied as is shown in Table 3.3. This can be explained by the fact that the addition of the (relatively weak) spring-damper does not significantly change $\boldsymbol{H}_{vw}^{(2)}$ and $\boldsymbol{H}_{yw}^{(2)}$ with respect to the system discussed in the previous section. Therefore, the small gain condition is again not met due to the similar dynamic stiffness levels of both components.

Table 3.3: *Bound on the loop gain, maximal assembly reduction error gain and upper bound on the assembly error gain for two equivalent spring-damper systems. For the first system, the spring-damper is attached to the right half of the beam. For the second system, the spring-damper is detached and serves as a subsystem itself.*

Variable	Unit	Attached spring-damper	Detached spring-damper
$\gamma_{wv}^{(1)}\gamma_{vw}^{(2)}$	-	$2.03\times10^{7} \not< 1$	$1.34\times10^{-2} < 1$
$\|\boldsymbol{E}_{yu}^{(assy)}\|_\infty$	m/N	9.21×10^{-8}	4.17×10^{-9}
$\bar{\varepsilon}_{yu}^{(assy)}$	m/N	n.a.	1.13×10^{-5}

In Figure 3.6, the subsystem boundary is chosen such that the spring-damper is a separate subsystem. Because of this, physically, the beam and the spring-damper components behave completely differently. Now, since $\boldsymbol{H}_{vw}^{(2)}$ has a (very) different profile with different dynamic stiffness levels compared to the beam subsystem, the small gain condition can potentially be met. This is again only true if the difference in dynamic stiffness of both subsystems is sufficiently high as was discussed in Section 3.2.1. Using the parameters for the spring-damper mentioned above, the small gain condition is met , as is evident from the value for $\gamma_{wv}^{(1)}\gamma_{vw}^{(2)}$ in Table 3.3. An additional advantage of the use of the spring-damper as a separate subsystem is that it has no resonances which increase the bound (as discussed at the second bullet in Section 3.2.1).

In Figure 3.7, the upper bound on the error gain of the assembly ($\bar{\varepsilon}_{yu}^{(assy)}$) as given in Equation

(3.3), is compared to the actual maximal error gain ($\|\boldsymbol{E}_{yu}^{(assy)}\|_\infty$) for both system representations. Here, only an error bound for the system with the detached spring-damper is presented, since for the other representation the small gain condition is not satisfied. The values for $\|\boldsymbol{E}_{yu}^{(assy)}\|_\infty$ and $\bar{\varepsilon}_{yu}^{(assy)}$ shown in Figure 3.7 are also listed in Table 3.3. Furthermore, it should be noted that $\boldsymbol{H}_{yu}^{(assy)}$ and $\boldsymbol{E}_{yu}^{(assy)}$ are identical for both system representations, proving that the representations are indeed equivalent.

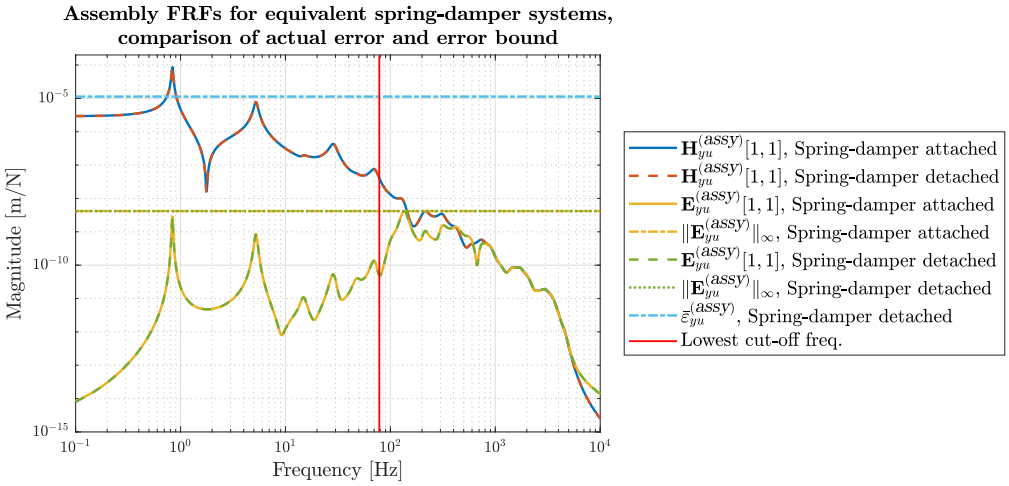

Figure 3.7: *Comparison of the bound on the error and upper bound on the assembly of both spring-damper system representations. The force-to-displacement elements of the presented transfer/error functions are plotted.*

To summarize, satisfying the small gain condition depends on the choice of the subsystem boundaries and the levels of the dynamic stiffness in both subsystems. For a system which does not satisfy the condition, a different interface boundary might enable low loop gains and hence satisfaction of the small gain condition. For instance, the first system shown (with a spring-damper attached to one half of the beam), can not be used in the framework of the small gain theorem, whereas detaching the spring-damper results in a system which satisfies the small gain theorem. It should however be noted that the location of the interface usually is not a choice, but a given design (boundary) condition. Therefore, only by coincidence the interfaces could be defined such that the small gain condition is satisfied.

Finally, it is remarked that the error bound propagation approach can also be applied to different physical systems. Here, thermal systems might prove to be especially interesting, since for these systems the small gain condition is possibly easier to satisfy. This assumption is based on the fact that thermal systems are represented by first-order equations and therefore do not have any resonance peaks in their FRFs. Furthermore, for problems in which the subsystems have different thermal properties, such as insulation problems, there is a difference in the magnitudes of the transfer functions of different thermal subsystems which is required for satisfying the small gain condition (similar to the required difference in dynamic stiffness magnitude levels of subsysytems in mechanical examples).

3.4 Discussion

In this chapter, the error bound propagation method has been introduced, explained and implemented to a simple demonstrator. For this, the approach proposed by Besselink [2] is extended

to a system consisting out of two linear subsystems which are both reduced. This approach provides an expression for a conservative bound on the reduction error gain of a reduced system (which is given in a feedback representation) with non-colocated in- and outputs. This bound could potentially be used to efficiently estimate the assembly error caused by using specific component reduction bases and use such estimates to compare the quality resulting from the use of various reduction bases.

This potential is however difficult to achieve since the error bound typically turns out to be too loose (possibly several orders of magnitude larger than the actual maximal value of the reduction error gain). Moreover, in practice, only a subset of systems satisfies the small gain condition, as illustrated for a simple cantilever beam demonstrator. Although filtering conditions the subsystems such that it is easier to meet the small gain condition, it turns out that this does not always suffice however.

Furthermore, by adding high damping and tuning parameters of the subsystems, a 'small gain compatible' system is obtained. Such systems are however relatively difficult to find and moreover do not represent realistic mechanical systems. The choice of the location of the interface is also of critical importance for meeting the small gain condition. Since subsystem boundaries can typically not be chosen freely however, the small gain condition remains a major limitation. Nevertheless, the error bound propagation method might have potential for different physical systems (e.g., thermal systems), which are characterized by different 'stiffness' levels for the components and do not suffer from resonance peaks.

Finally, since this approach requires a feedback representation framework, extendability of this approach to larger and/or different systems proves to be difficult. To tackle this problem, the LM FBS method can be used to couple component receptance matrices. In Section 2.2.5, it was however already shown that this method can not be applied efficiently to obtain a feedback form suitable for the error bound propagation approach. Therefore, in the next chapter, (unbounded) error propagation in the framework of the LM FBS method will be investigated as an alternative to using a feedback representation.

Chapter 4

Component error propagation

In the previous chapter, it was shown that the derived bound on the reduction error of an assembly is not very useful to determine the relevance of individual component modes to an assembly of mechanical subsystems. Therefore, in this chapter, two new methods to analyze the propagation of component errors are examined. Both methods are based on the Lagrange multiplier frequency-based substructuring technique as discussed in Section 2.2 and do not use bounds on the FRFs. The purpose of these methods is to determine the relevance of component modes for the assembly, by comparing the quality of the reduced assembly FRFs when different reduction bases (which use different combinations of eigenmodes) are implemented, such that an optimal set of kept component eigenmodes is found. One of the advantages of these propagation methods is that, in contrast to the feedback representation framework used in the previous chapter, the LM FBS method enables coupling more than two components with relative ease. Furthermore, the techniques discussed in this chapter are not limited by restrictive conditions.

Since this chapter concerns the propagation of component reduction errors, before introducing the propagation methods in Sections 4.2 and 4.3, Section 4.1 discusses how the reduction error of an uncoupled component can be estimated efficiently.

4.1 Component error estimation

This section proposes a more efficient approach to calculate the reduction error in a component which is caused by truncating eigenmodes. Here, the error is defined as the difference of the reduced receptance matrix with respect to the unreduced receptance matrix. For the reduction of components, the Hintz-Herting method is applied in this thesis. The reduction error is therefore typically obtained by subtracting the reduced receptance from the unreduced receptance:

$$\boldsymbol{E}_{HH}^{(c)} = \boldsymbol{Y}^{(c)} - \hat{\boldsymbol{Y}}_{HH}^{(c)}, \tag{4.1}$$

where the HH-reduced receptance $\hat{\boldsymbol{Y}}_{HH}^{(c)}$ is determined by Equation (2.51) and involves the computation of a costly inverse. Since, eventually, the reduction error needs to be evaluated for multiple reduction bases, this inverse operation has to be performed numerous times, which is not favorable because of computational costs. Therefore, this section introduces an alternative more efficient technique to determine $\hat{\boldsymbol{Y}}_{HH}^{(c)}$.

To find an efficient expression for the HH-induced component error, we first look at a powerful expression for the reduction error of a component which is reduced by modal truncation. Since

the eigenvectors of $\boldsymbol{M}^{(c)}$ and $\boldsymbol{K}^{(c)}$ orthogonalize $\boldsymbol{M}^{(c)}$ and $\boldsymbol{K}^{(c)}$, spectral decomposition of the unreduced receptance matrix is enabled [20, 29]:

$$\boldsymbol{Y}^{(c)}(\omega j) = \sum_{k=1}^{n_m^{(c)}} \frac{\boldsymbol{\phi}_k^{(c)} \boldsymbol{\phi}_k^{(c)^T}}{{\omega_k^{(c)}}^2 - 2j\xi_k^{(c)}\omega_k^{(c)}\omega - \omega^2} = \sum_{k=1}^{n_m^{(c)}} \boldsymbol{Y}_{\boldsymbol{\phi}_k}^{(c)}(\omega j), \tag{4.2}$$

where the unreduced receptance is obtained by summing the modal receptance contributions ($\boldsymbol{Y}_{\boldsymbol{\phi}_k}^{(c)}$) of all modes. Now, since reduction by modal truncation (MT) only uses a selection of these eigenvectors (indicated by the set $\mathcal{K}^{(c)}$), the MT-reduced receptance is given by the summation of the receptance contributions of these kept modes only:

$$\hat{\boldsymbol{Y}}_{MT}^{(c)}(\omega j) = \sum_{k \in \mathcal{K}^{(c)}} \frac{\boldsymbol{\phi}_k^{(c)} \boldsymbol{\phi}_k^{(c)^T}}{{\omega_k^{(c)}}^2 - 2j\xi_k^{(c)}\omega_k^{(c)}\omega - \omega^2} =: \sum_{k \in \mathcal{K}^{(c)}} \boldsymbol{Y}_{\boldsymbol{\phi}_k}^{(c)}(\omega j). \tag{4.3}$$

Equations (4.2) and (4.3) now immediately show that an efficient calculation of the MT-reduction error is obtained by the summation of the receptance contributions of all deleted modes:

$$\boldsymbol{E}_{MT}^{(c)}(\omega j) = \boldsymbol{Y}^{(c)}(\omega j) - \hat{\boldsymbol{Y}}_{MT}^{(c)}(\omega j) \tag{4.4}$$

$$= \sum_{k=1}^{n_m} \boldsymbol{Y}_{\boldsymbol{\phi}_k}^{(c)}(\omega j) - \sum_{k \in \mathcal{K}^{(c)}} \boldsymbol{Y}_{\boldsymbol{\phi}_k}^{(c)}(\omega) = \sum_{k \in \mathcal{D}^{(c)}} \boldsymbol{Y}_{\boldsymbol{\phi}_k}^{(c)}(\omega j), \tag{4.5}$$

where $\mathcal{D}^{(c)} = \{1, 2, \ldots, n_m^{(c)}\} \setminus \mathcal{K}^{(c)}$ denotes the set of deleted modes. Since the modal receptance contributions only have to be calculated once for every mode, if all component eigenmodes are known, Equation (4.5) proves to be a very efficient expression for computing a large variety of modal truncation errors caused by different combinations of deleted eigenmodes.

In the context of dynamic substructuring, where eventually multiple component mass and stiffness matrices are to be coupled, a modal truncation reduction basis does however not allow for easy coupling. The reason for this fact is that, in contrast to a CMS-based reduction basis, a MT reduction basis does not explicitly keep the boundary DOFs, as was explained in Section 2.3. Therefore, CMS-based reduction bases are used in a DS context. Since the Craig-Bampton method (introduced in Section 2.3.2) uses fixed-boundary vibration modes in contrast to the free-boundary vibration modes used in a modal truncation reduction basis, the CB error can not be expressed in terms of the modal receptance contributions as defined above. Therefore, the Hintz-Herting method (introduced in Section 2.3.3), which also uses free-boundary vibration modes, is used. In contrast to the MT method, the HH reduction error is not mathematically identical to the sum of the modal receptance contributions of the deleted modes. This is caused by the additional constraint and inertia relief modes in the HH basis.

In the following exposition, it is shown that that the contribution of these additional modes to the reduced receptance can be separated from the contributions of the eigenmodes. Since this extra contribution can be regarded as a term which makes the reduced receptance more exact, it is assumed that, if the reduction basis is to be optimized, the set of kept non-rigid eigenmodes should be optimized first. Afterwards, the error (resulting from the inclusion of the eigenmodes only) is decreased even more by the contribution of the additional modes. In other words, this approach assumes that the eigenmodes constituting an 'optimal' modal truncation basis, are also the eigenmodes which should be used for an 'optimal' Hintz-Herting basis. Below, it is shown that the contributions of the inertia relief and constraint modes can indeed be separated from the contributions of the eigenmodes, where the modal superposition characteristic of the eigenmodes is maintained as well.

To show that the eigenmode contributions can be separated from the constraint and inertia relief contributions, a different definition of the Hintz-Herting reduction basis is used:

$$\begin{bmatrix} \boldsymbol{u}_i \\ \boldsymbol{u}_b \end{bmatrix} \approx \underbrace{\begin{bmatrix} \boldsymbol{\Phi}_{\mathcal{K}} & \boldsymbol{\Phi}_{ir,o} & \boldsymbol{\Psi}_{const,o} \end{bmatrix}}_{\boldsymbol{T}_{HH,o}} \begin{bmatrix} \boldsymbol{q}_i \\ \boldsymbol{q}_{ir} \\ \boldsymbol{u}_b \end{bmatrix} := \begin{bmatrix} \boldsymbol{\Phi}_{\mathcal{K}} & \boldsymbol{X}_o \end{bmatrix} \begin{bmatrix} \boldsymbol{q}_i \\ \boldsymbol{q}_{ir} \\ \boldsymbol{u}_b \end{bmatrix}. \tag{4.6}$$

This equation is obtained by rewriting Equation (2.49) such that the (non-condensed) kept vibration eigenmodes $\boldsymbol{\Phi}_{\mathcal{K}}$ are used instead of the condensed vibration modes ($\boldsymbol{\Phi}_{CVM}$, which are forced to be zero at the boundary DOFs). Note that, in contrast to the equations given above, the explicit component notation ($^{(c)}$) is omitted for brevity in the remainder of this section.

Furthermore, in Equation (4.6), the small o in the subscripts of $\boldsymbol{\Phi}_{ir,o}$ and $\boldsymbol{\Psi}_{const,o}$ (of which the combination is indicated by $\boldsymbol{X}_o$) denotes that the columns of these variables have been made mass-orthonormal with respect to $\boldsymbol{\Phi}_{\mathcal{K}}$. This orthonormalization is performed by the stabilized Gram-Schmidt algorithm [13]. Here, the reduced system obtained with $\boldsymbol{T}_{HH,o}$ remains equivalent to the original reduced system (obtained with $\boldsymbol{T}_{HH}$ as in Equation (4.6)) under the orthogonalization process. The reduced mass and stiffness matrices obtained by this redefined reduction matrix are given by

$$\hat{\boldsymbol{M}}_{HH,o} = \boldsymbol{T}_{HH,o}^T \boldsymbol{M} \boldsymbol{T}_{HH,o} = \begin{bmatrix} \boldsymbol{I} & \boldsymbol{0} \\ \boldsymbol{0} & \boldsymbol{X}_o{}^T \boldsymbol{M} \boldsymbol{X}_o \end{bmatrix}, \tag{4.7}$$

and

$$\hat{\boldsymbol{K}}_{HH,o} = \boldsymbol{T}_{HH,o}^T \boldsymbol{K} \boldsymbol{T}_{HH,o} = \begin{bmatrix} \mathrm{diag}(k_i) & \boldsymbol{0} \\ \boldsymbol{0} & \boldsymbol{X}_o{}^T \boldsymbol{K} \boldsymbol{X}_o \end{bmatrix}, \tag{4.8}$$

where $\mathrm{diag}(k_i)$ is a diagonal matrix with the squared radial eigenfrequencies of the kept modes on its diagonal ($k_i = \omega_i^2,\ i \in \mathcal{K}$) [9]. Furthermore, block diagonal structures (which originate from the aforementioned orthonormalization), are clearly recognized.

Due to the fact that $\boldsymbol{\Phi}_{\mathcal{K}}$ and $\boldsymbol{X}_o$ block-diagonalize the (reduced) system matrices, the reduced receptance matrix can be calculated as the sum of receptance contributions of both individual blocks, as is proven in Appendix B.4 (note that this is similar to the orthogonalizing property of the eigenvectors enabling the spectral decomposition in Equation (4.2)). The resulting expression for $\hat{\boldsymbol{Y}}_{HH}$ is

$$\hat{\boldsymbol{Y}}_{HH}(\omega j) = \boldsymbol{Y}_{\boldsymbol{X}_o}(\omega j) + \sum_{k \in \mathcal{K}} \boldsymbol{Y}_{\boldsymbol{\phi}_k}(\omega j) \tag{4.9}$$

$$= \boldsymbol{Y}_{\boldsymbol{X}_o}(\omega j) + \hat{\boldsymbol{Y}}_{MT}(\omega j), \tag{4.10}$$

where $\boldsymbol{Y}_{\boldsymbol{X}_o}$ represents the receptance contribution of all inertia relief and constraint modes. Furthermore, since the upper left blocks in Equations (4.7) and (4.8) (which are caused by $\boldsymbol{\Phi}_{\mathcal{K}}$) are fully diagonal, the modal receptance contributions ($\boldsymbol{Y}_{\boldsymbol{\phi}_k}$) of each individual eigenmode as introduced in Equation (4.3) can still be used.

Since the lower right blocks in Equations (4.7) and (4.8) are not fully diagonal, the contribution to the reduced receptance of this block ($\boldsymbol{Y}_{\boldsymbol{X}_o}$) has to be calculated using Equation (4.11).

$$\boldsymbol{Y}_{\boldsymbol{X}_o}(\omega j) = \boldsymbol{X}_o \left(\hat{\boldsymbol{K}}_{\boldsymbol{X}_o} + \omega j \hat{\boldsymbol{D}}_{\boldsymbol{X}_o} - \omega^2 \hat{\boldsymbol{M}}_{\boldsymbol{X}_o} \right)^{-1} \boldsymbol{X}_o{}^T, \tag{4.11}$$

where $\hat{\boldsymbol{M}}_{X_o}$, $\hat{\boldsymbol{D}}_{X_o}$, and $\hat{\boldsymbol{K}}_{X_o}$ are given by

$$\hat{\boldsymbol{M}}_{X_o} = \boldsymbol{X}_o{}^T \boldsymbol{M} \boldsymbol{X}_o \qquad \hat{\boldsymbol{D}}_{X_o} = \boldsymbol{X}_o{}^T \boldsymbol{D} \boldsymbol{X}_o \qquad \hat{\boldsymbol{K}}_{X_o} = \boldsymbol{X}_o{}^T \boldsymbol{K} \boldsymbol{X}_o. \tag{4.12}$$

Note that this is analogous to the calculation of the component receptance using the dynamic stiffness in Equation (2.51) and hence involves the computation of an inverse.

The contributions of $\boldsymbol{Y}_{\boldsymbol{X}_o}$ and all individual modal receptance contributions ($\boldsymbol{Y}_{\boldsymbol{\phi}_k}$) to a reduced FRF are shown in Figure 4.1. For this figure, the FRF representing the transfer from a force at the retained node of component 1 (of the demonstrator beam as introduced in Section 2.4) to a displacement at the same node, is used. Notice that, since component 1 has no rigid body modes, $\boldsymbol{Y}_{\boldsymbol{X}_o}$ only represents the contribution of the constraint modes.

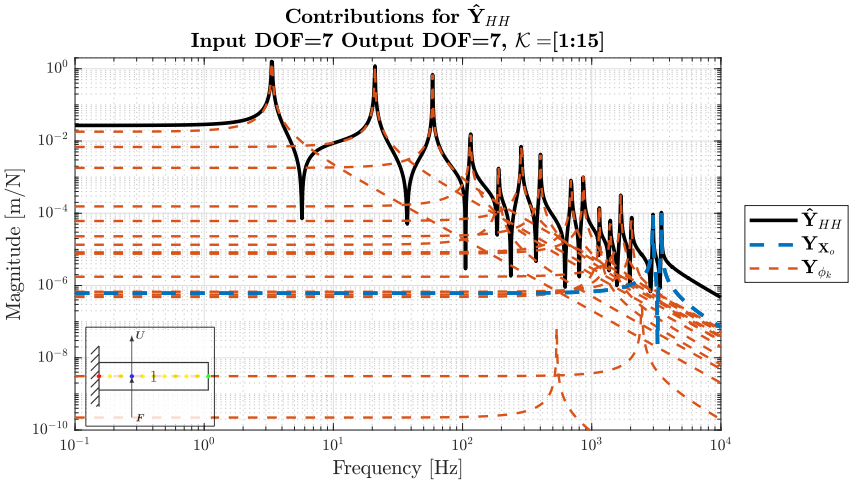

Figure 4.1: *Dynamic mode contributions and constraint mode contribution to the FRF at component 1 (force-to-displacement element). The reduced system shown here, is calculated by retaining eigenmodes 1-15.*

Finally, from Equation (4.10) and Figure 4.1 it becomes apparent that, if there are relatively few constraint and inertia relief modes compared to the number of kept eigenmodes, and a representative set of eigenmodes is used, the constraint and inertia relief contributions are relatively unimportant and hence $\hat{\boldsymbol{Y}}^{(c)}_{HH} \approx \hat{\boldsymbol{Y}}^{(c)}_{MT}$. Because of this, the assumption to use the eigenmodes for an 'optimal' MT basis for the 'optimal' HH basis, can be advocated. The reduced systems found using Hintz-Herting and modal truncation are namely comparable and hence the optimal set of kept eigenmodes for both bases will be, at the very least, comparable as well. One critical attribute of the Hintz-Herting method which allows for this, is that it uses free-boundary vibration modes, which the modal truncation method also uses. The error estimation technique introduced here might also be applicable to other CMS methods that employ free-boundary vibration modes. This is however left for further research.

4.2 Error contributors

This section aims at finding a method to determine the relevance of component modes to an assembly. Hereto, it is attempted to express the assembly error in terms of the deleted component eigenmodes. To do so, a technique is used that looks at the propagation of component errors through the assembly. By using this approach, assembly errors originating from different component modes can potentially be distinguished. This knowledge can then be used to select modes for 'optimal' component reduction bases, which minimize the assembly reduction error. In Section 4.2.1, the existence and applicability of such an expression is examined. Afterwards, Section 4.2.2 applies the findings of Section 4.2.1 to the cantilever beam demonstrator.

4.2.1 Error contributor definition

The method presented here uses the Lagrange multiplier frequency-based substructuring method to define the assembly receptance as a function of the receptances of the uncoupled components. To recapitulate from Section 2.2.3, the LM FBS method makes use of

$$\boldsymbol{Y}^{(assy)} = \boldsymbol{Y} - \boldsymbol{Y}\boldsymbol{B}_f^T(\boldsymbol{B}_f\boldsymbol{Y}\boldsymbol{B}_f^T)^{-1}\boldsymbol{B}_f\boldsymbol{Y} \tag{4.13}$$

to express the receptance matrix of the assembly ($\boldsymbol{Y}^{(assy)}$) in terms of the uncoupled component receptance matrices, which are given by the blocks of the block diagonal matrix $\boldsymbol{Y}$ (see Section 2.2.3). The assembly of uncoupled component receptances is enabled by the boolean mapping matrix $\boldsymbol{B}_f$, which selects the interface DOF related partitions of $\boldsymbol{Y}$. Similarly, the reduced assembly receptance is given by

$$\hat{\boldsymbol{Y}}^{(assy)} = \hat{\boldsymbol{Y}} - \hat{\boldsymbol{Y}}\boldsymbol{B}_f^T(\boldsymbol{B}_f\hat{\boldsymbol{Y}}\boldsymbol{B}_f^T)^{-1}\boldsymbol{B}_f\hat{\boldsymbol{Y}}. \tag{4.14}$$

Using the above equations, the assembly reduction error ($\boldsymbol{E}_Y^{(assy)} = \boldsymbol{Y}^{(assy)} - \hat{\boldsymbol{Y}}^{(assy)}$) is expressed in terms of so-called error contributors (indicated by a bar, $\bar{\boldsymbol{E}}$):

$$\begin{aligned}\boldsymbol{E}_{Y,bb}^{(assy)} &= \underbrace{\boldsymbol{E}_{Y,bb}}_{\bar{\boldsymbol{E}}_{bb}} \underbrace{- \boldsymbol{E}_{Y,bf}\boldsymbol{Y}_{ff}^{-1}\boldsymbol{Y}_{fb}}_{\bar{\boldsymbol{E}}_{bf}} \underbrace{- \hat{\boldsymbol{Y}}_{bf}\overbrace{\left(\boldsymbol{Y}_{ff}^{-1} - \hat{\boldsymbol{Y}}_{ff}^{-1}\right)}^{\boldsymbol{E}_{BYB^T}}\boldsymbol{Y}_{fb}}_{\bar{\boldsymbol{E}}_{ff}} \underbrace{- \hat{\boldsymbol{Y}}_{bf}\hat{\boldsymbol{Y}}_{ff}^{-1}\boldsymbol{E}_{Y,fb}}_{\bar{\boldsymbol{E}}_{fb}} \\ &= \bar{\boldsymbol{E}}_{bb} + \bar{\boldsymbol{E}}_{bf} + \bar{\boldsymbol{E}}_{ff} + \bar{\boldsymbol{E}}_{fb},\end{aligned} \tag{4.15}$$

where the subscripts $_f$ and $_b$ refer to interface and boundary DOFs, respectively. A derivation of this expression is given in Appendix B.5. Since the reduction is performed in the CMS context, the static behavior is only approximated properly at the boundary nodes. Therefore, only the transfers related to the boundary DOFs (or POIs) are taken into account in Equation (4.15).

Equation (4.15) shows that different 'error sources' ($\boldsymbol{E}_{Y,bb}$, $\boldsymbol{E}_{Y,bf}$, $\boldsymbol{E}_{BYB^T}$, and $\boldsymbol{E}_{Y,fb}$) exist, which are the errors of transfer functions between specific node types (e.g., $\boldsymbol{E}_{Y,bf}$ is the error of the receptance matrix containing transfers from interface DOFs to boundary DOFs). The propagation of these error sources is facilitated by pre- and/or post-multiplying these error sources with receptance matrices which results in propagated errors (the error contributors in Equation (4.15)). This way of calculating the assembly error is similar to the error bound propagation method, where the bounds on the transfer errors propagate through the assembly by pre- and post-multiplication with bounds on transfer functions as well.

Each propagated error can thus be interpreted as the contribution of some error of the transfer between specific DOFs to the assembly error. For example, $\bar{\boldsymbol{E}}_{bb}$ can be interpreted as the part of the assembly error resulting from the error of transfers between inputs and outputs at boundary DOFs of the uncoupled components. Similarly, $\bar{\boldsymbol{E}}_{bf}$ represents the propagated error matrix originating from the transfers from the interface DOFs to any DOF at the output, where the outputs are typically the points of interest. Since the POIs are defined as boundary DOFs (because of the static correctness of these DOFs in a CMS context), the outputs are located at the boundary DOFs. The interpretation of the other error contributors is summarized in Table 4.1.

Table 4.1: *Interpretation of all error contributors in Equation (4.15). The in- and outputs can be located at any boundary DOF.*

$\bar{\boldsymbol{E}}$	Interpretation of error contributor
$\bar{\boldsymbol{E}}_{bb}$	Error of the transfer function from the input (at any boundary DOF) to the output (at any boundary DOF) for uncoupled components.
$\bar{\boldsymbol{E}}_{bf}$	Propagated error of the transfer from interface DOFs to the output (at any boundary DOF).
$\bar{\boldsymbol{E}}_{ff}$	Propagated error of the transfer from interface DOFs to interface DOFs.
$\bar{\boldsymbol{E}}_{fb}$	Propagated error of the transfer from input (at any boundary DOF) to interface DOFs.

By using the interpretations of the contributions to the assembly error, shown in Table 4.1, an insightful classification of the most important parts contributing to the total reduction error is obtained. Section 4.2.2 discusses this in further detail, but first the applicability of this expression for an 'automated' component mode selection procedure is discussed.

As mentioned before, the reduction error of the assembly will be used to choose component eigenmodes such that the assembly reduction error is minimized. Therefore, it would be highly beneficial if there would be an expression that gives the contribution of a single component mode to the assembly error (similar to how $\boldsymbol{Y}^{(c)}_{\boldsymbol{\phi}_k}$ does this for the component receptance in Equation (4.5)). Using such a hypothetical expression, the assembly error would be given by the sum of the assembly contributions caused by all deleted modal receptance contributions. Since the component modes associated to the highest contributions to the assembly error would then constitute the optimal set of kept modes, selecting an optimal set in this way would be relatively easy. Existence of an expression which has the above mentioned property would therefore be highly beneficial.

In Equations (4.16)-(4.18), it is shown that $\boldsymbol{E}_Y$ can be written in terms of modal receptance contributions:

$$\boldsymbol{E}_Y = \boldsymbol{Y} - \hat{\boldsymbol{Y}} \tag{4.16}$$

$$= \begin{bmatrix} \sum_{k=1}^{n_m^{(1)}} \boldsymbol{Y}^{(1)}_{\boldsymbol{\phi}_k} & & \\ & \ddots & \\ & & \sum_{k=1}^{n_m^{(n_c)}} \boldsymbol{Y}^{(n_c)}_{\boldsymbol{\phi}_k} \end{bmatrix} - \begin{bmatrix} \sum_{k\in\mathcal{K}^{(1)}} \boldsymbol{Y}^{(1)}_{\boldsymbol{\phi}_k} & & \\ & \ddots & \\ & & \sum_{k\in\mathcal{K}^{(n_c)}} \boldsymbol{Y}^{(n_c)}_{\boldsymbol{\phi}_k} \end{bmatrix} \tag{4.17}$$

$$= \begin{bmatrix} \sum_{k\in\mathcal{D}^{(1)}} \boldsymbol{Y}^{(1)}_{\boldsymbol{\phi}_k} & & \\ & \ddots & \\ & & \sum_{k\in\mathcal{D}^{(n_c)}} \boldsymbol{Y}^{(n_c)}_{\boldsymbol{\phi}_k} \end{bmatrix}. \tag{4.18}$$

Since $\boldsymbol{E}_{Y,bb}$, $\boldsymbol{E}_{Y,bf}$, and $\boldsymbol{E}_{Y,fb}$ are partitions of $\boldsymbol{E}_Y$ (selected by $\boldsymbol{B}_f$), these error sources can be expressed in terms of the modal receptance contributions. In contrast to these error sources, the error source of $\bar{\boldsymbol{E}}_{ff}$ ($\boldsymbol{E}_{BYB^T}$) can not be expressed in terms of the deleted component mode contributions however. The reason for this is that this error is actually a combination of the receptance matrices of multiple components that share an interface. Since the inverse of a sum does not equal the sum of the inverses, this error source can not be written in terms of the

reduction error of the uncoupled components ($\boldsymbol{E}_Y = \boldsymbol{Y} - \hat{\boldsymbol{Y}}$) as is shown in below

$$\boldsymbol{E}_{BYB^T} = \boldsymbol{Y}_{ff}^{-1} - \hat{\boldsymbol{Y}}_{ff}^{-1} \tag{4.19}$$

$$= \left(\boldsymbol{B}_f \boldsymbol{Y} \boldsymbol{B}_f^T\right)^{-1} - \left(\boldsymbol{B}_f \hat{\boldsymbol{Y}} \boldsymbol{B}_f^T\right)^{-1} \tag{4.20}$$

$$\neq \left(\boldsymbol{B}_f \left(\boldsymbol{Y} - \hat{\boldsymbol{Y}}\right) \boldsymbol{B}_f^T\right)^{-1}. \tag{4.21}$$

Since it is not possible to write $\boldsymbol{E}_{BYB^T}$ in terms of the modal receptance contributions of the component modes, $\boldsymbol{E}_{Y,bb}^{(assy)}$ cannot be directly allocated to the receptance contributions of the truncated component modes.

An alternative approach to find the optimal reduction bases using Equation (4.15) would be to compute various assembly errors, caused by different reduction bases (with different combinations of kept eigenmodes), and compare them. Using Equation (4.15) for this would however be less efficient than directly computing $\boldsymbol{E}_{Y,bb}^{(assy)} = \boldsymbol{Y}_{bb}^{(assy)} - \hat{\boldsymbol{Y}}_{bb}^{(assy)}$, where the component receptances are calculated using Equations (4.13) and (4.14) (although also the estimation of the component error as introduced in Section 4.1 can be used). Therefore, Section 4.3 proposes a different, more efficient error propagation technique.

Although it is concluded that Equation (4.15) does not enable an efficient evaluation of the assembly error, the decomposition into error contributors does provide insight. This is treated in the following subsection.

4.2.2 Error contributor implementation

Since Equation (4.15) gives an expression for the assembly reduction error in terms of error contributors, this equation can be used to assess the influence and relevance of each individual error contributor. In this section, this is illustrated by an application to the demonstrator, where the reduced beam as provided in Section 2.4 is used (note that the error estimation technique of Section 4.1 is thus not used here). For this, it is most straightforward to neglect phase information and only compare magnitudes. To obtain a fair comparison, the contributors should then however not be compared to the magnitude of the actual error, but rather to the sum of the magnitudes of the error contributors, as defined by

$$\left|\boldsymbol{E}_{Y,bb}^{(assy)}[k,l]\right| \leq \left|\bar{\boldsymbol{E}}_{bb}[k,l]\right| + \left|\bar{\boldsymbol{E}}_{bf}[k,l]\right| + \left|\bar{\boldsymbol{E}}_{ff}[k,l]\right| + \left|\bar{\boldsymbol{E}}_{fb}[k,l]\right| = \bar{\boldsymbol{E}}_{sum}[k,l], \tag{4.22}$$

where the triangle inequality is exploited and $\boldsymbol{E}[k,l]$ selects the element in row k and column l of $\boldsymbol{E}$. From this equation, it can be seen that $\bar{\boldsymbol{E}}_{sum}$ serves as an upper bound on the actual error. In Figure 4.2, the magnitude and phase information of all error contributors is shown for the transfer between a non-colocated in- and output. This figure shows that $\bar{\boldsymbol{E}}_{sum}[k,l]$ (bright green) is not perfectly equal to $\left|\boldsymbol{E}_{Y,bb}^{(assy)}[k,l]\right|$ (black), but provides a relatively good approximation. This holds especially well below the cutoff frequencies of both components.

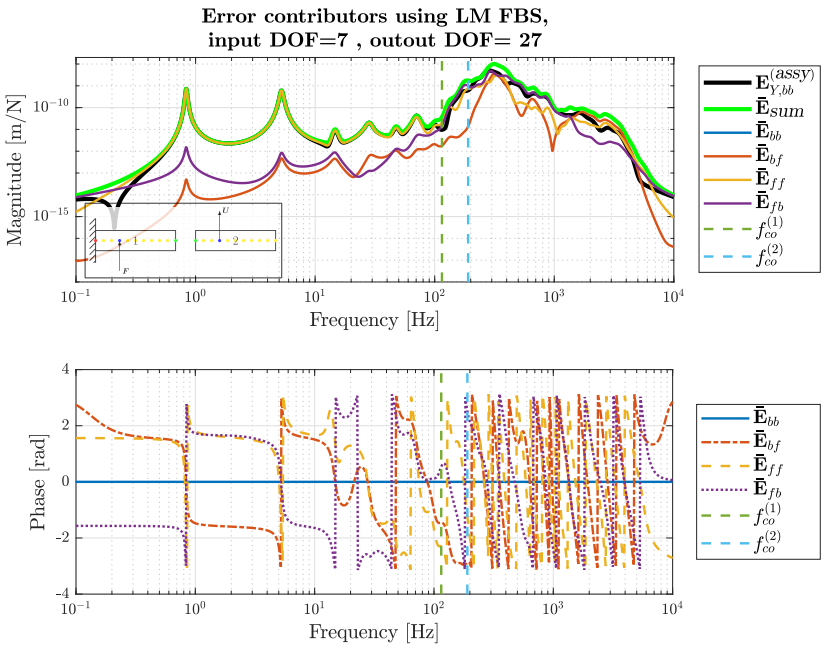

Figure 4.2: *Comparison of the magnitudes of all error contributors to $\bar{\boldsymbol{E}}_{sum}$ for the transfer between a force at component 1 to a displacement at component 2. In the lower plot the corresponding phase information is shown.*

In more detail we observe that the reason for why the magnitudes of the error contributors need to be compared to $\bar{\boldsymbol{E}}_{sum}$ lies in the fact that the error contributors carry specific phase information. For example, if two error contributors have opposing phase, the magnitudes are 'compensating'. In this case, the magnitude of both transfers may be larger than the actual error, giving a false impression of their relevance. This is for example seen at the first anti-resonance of the actual error (black) in Figure 4.2 ($f = 0.21$ Hz). This is however not a major issue since the reduction error is already low at such an anti-resonance anyway, which is favorable.

It should be noticed that, in Figure 4.2, the blue line (which represents the contribution of $\bar{\boldsymbol{E}}_{bb}$) is zero. This is explained by the fact that, since a transfer from one component to an other is investigated, this transfer is located in one of the off-diagonal blocks of $\boldsymbol{E}_{Y,bb}$ which is zero due ot the block diagonal form of $\boldsymbol{Y}$ ($\boldsymbol{E}_{Y,bb} = \boldsymbol{Y}_{Y,bb} - \hat{\boldsymbol{Y}}_{Y,bb}$).

From Figure 4.2, it is apparent that, especially below the cutoff frequency, $\bar{\boldsymbol{E}}_{ff}$ dominates the assembly error. This relevance of interface transfer functions is recognized from Chapter 3 where the interface transfers went through a feedback loop potentially causing the assembly error to 'blow up'. From this fact, it can thus be concluded that the interface transfers play the most important role in the assembly of substructures.

Finally, it should be noted that the system represented in Figure 4.2 is a damped system. For this, modal damping has a been implemented where for each mode $\xi_k = 0.05$. In the remaining part of this thesis, this specific modal damping is used.

4.3 Sensitivity-based error propagation

This section introduces an alternative way to assess the propagation of component errors through an assembly. This new method utilizes the LM FBS expression as a starting point for a sensitivity

approach to approximate the assembly error. First of all, Section 4.3.1 presents and explains this approach in detail. Afterwards, Section 4.3.2 shows an implementation of this technique and gives some conclusions on (among others) the applicability of this approach for an automated selection procedure.

As was done in the previous section, this section only evaluates the boundary node-related entries of the receptance matrices. The receptance matrix $\boldsymbol{Y}$ will therefore, from here on, only denote the partition containing the boundary DOF related entries of the receptance, which were previously denoted using the explicit subscript notation $\boldsymbol{Y}_{bb}$.

4.3.1 Definition of sensitivity-based error propagation methodology

As the name suggests, the sensitivity-based error propagation approach makes use of a sensitivity to determine the propagation of component errors. To be exact, the sensitivity of the assembly receptance with respect to component receptance(s) is used. In Equation (4.23), which approximates the assembly error as a consequence of an error in (one of) the components ($\boldsymbol{\Delta Y}$), this sensitivity is given by the term $\frac{\partial \boldsymbol{Y}^{(assy)}}{\partial \boldsymbol{Y}}$.

$$\boldsymbol{E}_Y^{(assy)}(\omega j) \approx \boldsymbol{\Delta Y}^{(assy)}(\omega j) = \sum_{k}^{n_b^{(assy)}} \sum_{l}^{n_b^{(assy)}} \frac{\partial \boldsymbol{Y}^{(assy)}}{\partial \boldsymbol{Y}[k,l]}(\omega j) \boldsymbol{\Delta Y}[k,l](\omega j). \tag{4.23}$$

Here, $n_{sum,b}$ denotes the sum of the number of boundary DOFs in all components (remember that $\boldsymbol{Y} \in \mathbb{C}^{n_{sum,b} \times n_{sum,b}}$), and $[k,l]$ selects specific matrix-elements. Equation (4.23) is based on an uncertainty quantification method found in the work of Voormeren [30] and de Klerk and Voormeren [18], that uses a first-order Taylor approximation to determine the difference in the assembly as a result of a change/error in the component receptances. In contrast to the work in [30, 18], this thesis focuses on a numerical application. For brevity, the explicit frequency-dependence notation as used in Equation (4.23) is omitted in the following exposition.

Equation (4.23) thus provides a different way to check the reduction quality of the assembly as a result of specific component reduction bases. One of the advantages of this approach is that, according to this equation, an error in the assembly has two (separable) causes (the error in an uncoupled component and its propagation through the assembly). Besides the premise that this gives additional insight, the computation of these terms can be separated. The following two subsections will provide derivations of these individual terms, starting with $\frac{\partial \boldsymbol{Y}^{(assy)}}{\partial \boldsymbol{Y}[k,l]}$.

4.3.1.1 Sensitivity of assembly with respect to component

To quantify the sensitivity of the assembly receptance with respect to component receptances, the expression for an assembly receptance matrix as defined in the LM FBS framework is recapitulated:

$$\boldsymbol{Y}^{(assy)} = \boldsymbol{Y} - \boldsymbol{Y}\boldsymbol{B}_f^T(\boldsymbol{B}_f\boldsymbol{Y}\boldsymbol{B}_f^T)^{-1}\boldsymbol{B}_f\boldsymbol{Y} \tag{4.24}$$

$$= \boldsymbol{Y} - \boldsymbol{Y}\boldsymbol{Q}\boldsymbol{Y}, \tag{4.25}$$

where $\boldsymbol{Q}$ is defined as

$$\boldsymbol{Q} = \boldsymbol{B}_f^T \left(\boldsymbol{B}_f\boldsymbol{Y}\boldsymbol{B}_f^T\right)^{-1} \boldsymbol{B}_f. \tag{4.26}$$

Calculating the partial derivative of Equation (4.25) with respect to an element in $\boldsymbol{Y}$ gives:

$$\begin{aligned}\frac{\partial \boldsymbol{Y}^{(assy)}}{\partial \boldsymbol{Y}[k,l]} &= \frac{\partial \boldsymbol{Y}}{\partial \boldsymbol{Y}[k,l]} - \frac{\partial \left(\boldsymbol{Y}\boldsymbol{Q}\boldsymbol{Y}\right)}{\partial \boldsymbol{Y}[k,l]} \\ &= \frac{\partial \boldsymbol{Y}}{\partial \boldsymbol{Y}[k,l]} - \frac{\partial \boldsymbol{Y}}{\partial \boldsymbol{Y}[k,l]}\boldsymbol{Q}\boldsymbol{Y} - \boldsymbol{Y}\frac{\partial \boldsymbol{Q}}{\partial \boldsymbol{Y}[k,l]}\boldsymbol{Y} - \boldsymbol{Y}\boldsymbol{Q}\frac{\partial \boldsymbol{Y}}{\partial \boldsymbol{Y}[k,l]},\end{aligned} \tag{4.27}$$

where the product rule has been used.

In Equation (4.27), two distinctive partial derivatives are used. The first derivative ($\frac{\partial \boldsymbol{Y}}{\partial \boldsymbol{Y}[k,l]}$) which stands for the derivative of the matrix containing the uncoupled component receptances with respect to one of its elements, is rather simple to compute. Since all matrices are linear with respect to their elements, this derivative is namely written as:

$$\frac{\partial \boldsymbol{Y}}{\partial \boldsymbol{Y}[k,l]} = \boldsymbol{P}_{kl}, \tag{4.28}$$

where $\boldsymbol{P}_{kl}$ is a zero matrix, except for the entry at row k and column l which equals 1 [30].

Furthermore, the second derivative ($\frac{\partial \boldsymbol{Q}}{\partial \boldsymbol{Y}[k,l]}$) can be written in terms of $\frac{\partial \boldsymbol{Y}}{\partial \boldsymbol{Y}[k,l]}$:

$$\frac{\partial \boldsymbol{Q}}{\partial \boldsymbol{Y}[k,l]} = \boldsymbol{B}_f^T \frac{\partial \left(\boldsymbol{B}_f \boldsymbol{Y} \boldsymbol{B}_f^T\right)^{-1}}{\partial \boldsymbol{Y}[k,l]} \boldsymbol{B}_f \tag{4.29}$$

$$= -\boldsymbol{B}_f^T \left(\boldsymbol{B}_f \boldsymbol{Y} \boldsymbol{B}_f^T\right)^{-1} \frac{\partial \left(\boldsymbol{B}_f \boldsymbol{Y} \boldsymbol{B}_f^T\right)}{\partial \boldsymbol{Y}[k,l]} \left(\boldsymbol{B}_f \boldsymbol{Y} \boldsymbol{B}_f^T\right)^{-1} \boldsymbol{B}_f \tag{4.30}$$

$$= -\boldsymbol{B}_f^T \left(\boldsymbol{B}_f \boldsymbol{Y} \boldsymbol{B}_f^T\right)^{-1} \boldsymbol{B}_f \frac{\partial \boldsymbol{Y}}{\partial \boldsymbol{Y}[k,l]} \boldsymbol{B}_f^T \left(\boldsymbol{B}_f \boldsymbol{Y} \boldsymbol{B}_f^T\right)^{-1} \boldsymbol{B}_f. \tag{4.31}$$

Consequently, by implementing Equations (4.26) and (4.28), a relatively simple expression for the derivative of $\boldsymbol{Q}$ with respect to an element in $\boldsymbol{Y}$ is obtained:

$$\frac{\partial \boldsymbol{Q}}{\partial \boldsymbol{Y}[k,l]} = \boldsymbol{Q}\boldsymbol{P}_{kl}\boldsymbol{Q}. \tag{4.32}$$

To arrive at Equation (4.30), it is used that $\frac{\partial (\boldsymbol{A}^{-1})}{\partial p} = -\boldsymbol{A}^{-1}\frac{\partial \boldsymbol{A}}{\partial p}\boldsymbol{A}^{-1}$ for some invertible matrix $\boldsymbol{A}$, where $\boldsymbol{A}$ is substituted by $\boldsymbol{B}_f \boldsymbol{Y} \boldsymbol{B}_f^T$.

To conclude, by combining Equation (4.27), (4.28), and (4.32), $\frac{\partial \boldsymbol{Y}^{(assy)}}{\partial \boldsymbol{Y}[k,l]}$ is given by

$$\frac{\partial \boldsymbol{Y}^{(assy)}}{\partial \boldsymbol{Y}[k,l]} = \boldsymbol{P}_{kl} - \boldsymbol{P}_{kl}\boldsymbol{Q}\boldsymbol{Y} + \boldsymbol{Y}\boldsymbol{Q}\boldsymbol{P}_{kl}\boldsymbol{Q}\boldsymbol{Y} - \boldsymbol{Y}\boldsymbol{Q}\boldsymbol{P}_{kl}. \tag{4.33}$$

Note that, when the sensitivity with respect to multiple elements of $\boldsymbol{Y}$ is to be determined, the inverse needed for $\boldsymbol{Q}$ only has to be calculated once, making its implementation relatively efficient.

4.3.1.2 Error in uncoupled components

In Equation (4.23), the error made in components as a result of reduction is given by $\boldsymbol{\Delta Y}$. Because of the block-diagonal structure of $\boldsymbol{Y}$, $\boldsymbol{\Delta Y}$ is block diagonal as well. The blocks on the diagonal of $\boldsymbol{\Delta Y}$ represent the errors made in the individual component receptances ($\boldsymbol{\Delta Y}^{(c)}$):

$$\boldsymbol{\Delta Y} = \text{diag}\left(\boldsymbol{\Delta Y}^{(1)}, \ldots, \boldsymbol{\Delta Y}^{(n_c)}\right). \tag{4.34}$$

In Section 4.1, it was assumed that the non-rigid free-boundary eigenmodes used for an 'optimal'/improved modal truncation basis are also the dynamic eigenmodes which can be used for an improved Hintz-Herting reduction basis. The reduction errors of the uncoupled components are therefore given as the sum of the modal receptance contributions of the deleted eigenmodes:

$$\boldsymbol{\Delta Y}^{(c)} = \sum_{k \in \mathcal{D}} \boldsymbol{Y}^{(c)}_{\boldsymbol{\phi}_k} = \sum_{k \in \mathcal{D}^{(c)}} \frac{\boldsymbol{\phi}_k^{(c)} \boldsymbol{\phi}_k^{(c)^T}}{{\omega_k^{(c)}}^2 - 2j\xi_k^{(c)}\omega_k^{(c)}\omega - \omega^2}. \tag{4.35}$$

The advantage of the use of Equation (4.35) is once more the low associated computational cost.

4.3.2 Implementation of sensitivity-based error propagation

Using the expression to approximate the assembly error caused by truncating component modes, as found in the previous section, the relevance of individual component modes for the assembly can be evaluated. In this section, this is illustrated for the demonstrator beam where the Young's modulus of component 1 has been lowered by a factor of 100 with respect to the original parameters as given in Table A.2 (the updated parameters are given in Table A.3). The motivation behind this change is that it allows for easier discrimination between modes of both components.

To judge the influence of individual modes on the assembly, a strategy is applied where the assembly error caused by only excluding a single component mode from the reduction basis of the corresponding component is approximated. If a mode of a specific component is deleted from the reduction basis of this component, all other components are thus unreduced and hence have no associated error. By comparing such approximated assembly errors for various cases where individual component modes are truncated, the relative relevance of each component mode is assessed. In line with our notation, the approximated assembly error caused by exclusively truncating mode $\boldsymbol{\phi}_k^{(c)}$, is denoted by $\boldsymbol{\Delta Y}^{(assy)}_{\boldsymbol{\phi}_k^{(c)}}$.

Although $\boldsymbol{\Delta Y}^{(assy)}_{\boldsymbol{\phi}_k^{(c)}}$ represents a MIMO error, analyzing one specific element of this 'error matrix' (representing a SISO transfer) already provides some insight in which deleted modes cause the largest errors. Figure 4.3 illustrates such a comparison for the approximated errors for the demonstrator beam, caused by individually truncating $\boldsymbol{\phi}_1^{(1)}$, $\boldsymbol{\phi}_2^{(1)}$, $\boldsymbol{\phi}_1^{(2)}$, or $\boldsymbol{\phi}_2^{(2)}$. This figure shows that deleting either one of the first 2 modes of component 1 results in significantly higher (approximated) assembly errors than when one of the first 2 modes of component 2 is truncated. Performing such an analysis for all component modes gives the opportunity to determine improved reduction bases by selecting the most relevant component modes. In Chapter 5, this selection procedure will be automated.

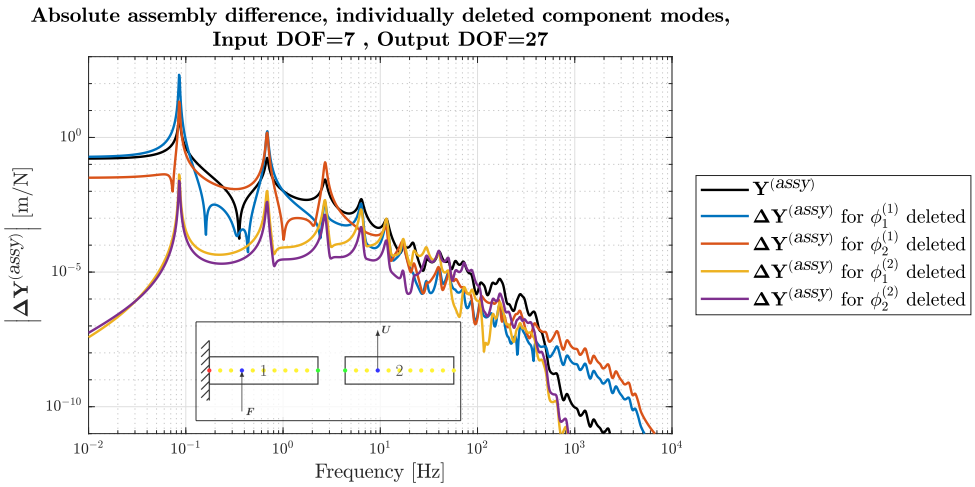

Figure 4.3: *Comparison of the magnitudes of the approximated (absolute) assembly errors induced by truncating individual component modes (modes $\boldsymbol{\phi}_1^{(1)}$, $\boldsymbol{\phi}_2^{(1)}$, $\boldsymbol{\phi}_1^{(2)}$, and $\boldsymbol{\phi}_2^{(2)}$). This approximation is performed with the sensitivity-based error propagation approach.*

The fact that, according to Figure 4.3, the second component is less relevant for the assembly error, can be related to the relatively low stiffness of component 1. Due to this less stiff component, this part of the beam will deflect and bend more than component 2. Therefore, component 1 dominates the behavior of the entire beam. With this knowledge, it is explained that an error in component 1 indeed leads to relatively high errors in the assembly compared to an error in component 2.

Finally, since Figure 4.3 only shows the error of one particular transfer (one element of $\boldsymbol{\Delta Y}^{(assy)}_{\boldsymbol{\phi}_k^{(c)}}$), Chapter 5 will discuss how the approximated error of all transfers of interest can be taken into account in an automated selection procedure. Furthermore, although the absolute error, plotted in Figure 4.3, definitely gives insight in the relevance of modes, (in this example) it does not provide a fair comparison between low- and high-frequency errors. This is for instance recognized at high frequencies, where the absolute errors of the modes of component 1 (blue and red) are relatively low in comparison to their static value. Because of this, it seems as if the reduction is accurate at these high frequencies. Relative to the unreduced receptance (black), these errors are very large however, hence indicating that the approximated FRFs are inaccurate in these frequency regions. In Chapter 5, this will be resolved by using a relative measure for the error.

4.4 Discussion

This chapter introduced an efficient expression for the reduced receptance error of a component which is reduced using a modal truncation reduction basis. Since the Hintz-Herting basis uses the same free-boundary vibration modes as the modal truncation basis, it is assumed that the modes used in the 'optimal' MT reduction basis are also the eigenmodes to be used in an 'optimal' HH reduction basis.

In Section 4.2, a method was developed which divides an assembly reduction error in contributions of specific error sources that propagate through the assembly. This expression can however not be used to express the assembly error in contributions of the individual component modes.

Therefore, the influence of an individual component mode on the assembly can not be quantified precisely using this method. Also, calculating the assembly error (for multiple reduction bases) using this method is not preferred, as it involves computing multiple inverses. For these reasons, it is advised not to use the error contributor expression in an automated component selection procedure, as this requires an efficient way to assess the relevance of individual component modes. Nevertheless, some insights can be obtained by using these error contributors. For example, it tells us that (for the demonstrator), below the cutoff frequency, the contribution of the interface receptance errors dominates the reduction error of the assembly.

As an alternative propagation method, Section 4.3 introduced a technique to approximate the reduction error of an assembly. This technique is summarized in Figure 4.4, where the approach is divided in two branches: the sensitivity branch (left) and component error branch (right). In the right branch, the modal receptance contributions of each component mode efficiently determine the component reduction error, as was explained in Section 4.1. The left branch uses the partial derivative of the LM FBS expression for the assembly receptance with respect to the uncoupled component receptances. Finally, the component error (obtained by the right branch) and the sensitivity (left branch), are combined to obtain the first-order Taylor approximation of the difference in the assembly induced by these component errors.

By applying this method to the demonstrator beam, the potential of this method to assess the relevance of component modes was shown. Using this knowledge, component designs can be enhanced such that the performance of the assembly is improved. Furthermore, it enables the relatively efficient computation of the assembly reduction error caused by truncating individual component modes. This is used for an automated selection procedure, which will be discussed in Chapter 5.

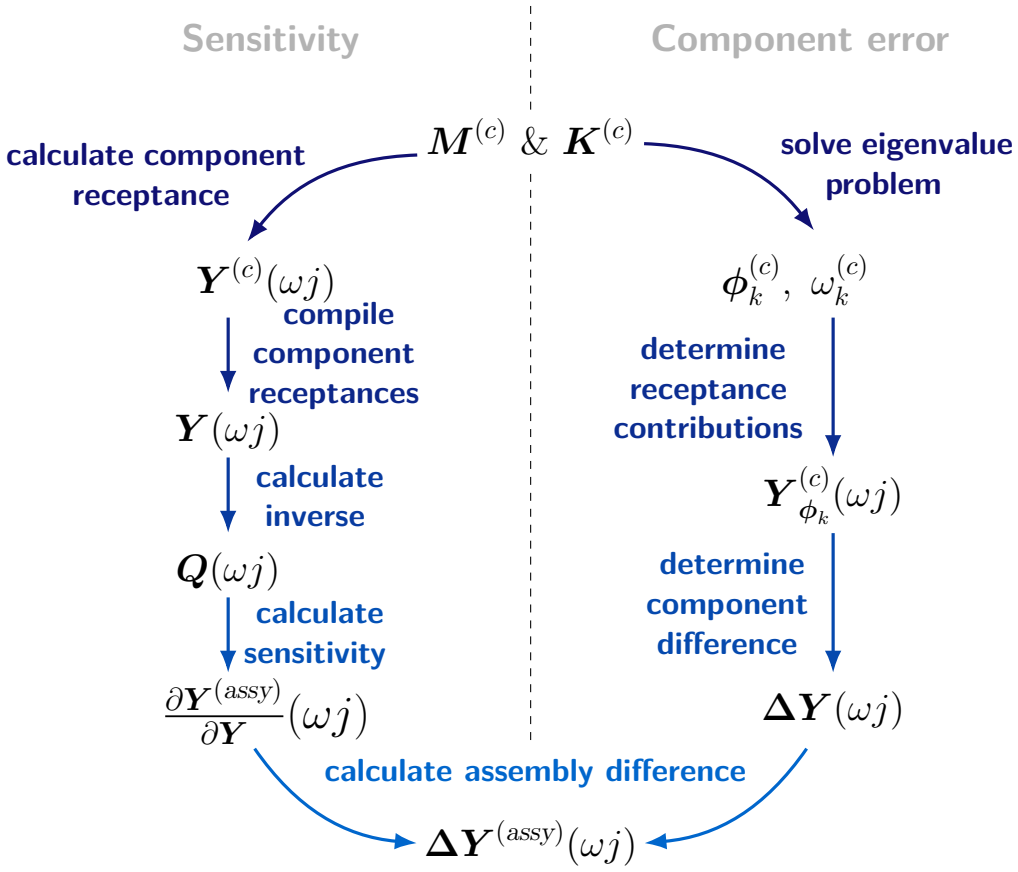

Figure 4.4: *Roadmap for the sensitivity-based assembly error approximation method, consisting out of the component error estimation, and sensitivity-based error propagation.*

Chapter 5

Component mode selection

As discussed in the previous chapter, the representation of an assembly error in contributors is not an efficient way to calculate the errors associated to a large number of reduction bases. Therefore, in this chapter, the approximated assembly error obtained by the sensitivity-based approach (introduced in Section 4.3) is used. The goal of this chapter is to establish an 'automated' procedure which selects which dynamic eigenmodes should be used in the Hintz-Herting reduction bases of the components. Since the Hintz-Herting reduction basis already takes the rigid eigenmodes into account using the inertia relief modes, this selection will only concern non-rigid eigenmodes. To automate the selection process, first a measure for the error which allows for straightforward ranking of different receptance errors is defined in Section 5.1. Afterwards, Section 5.2 elaborates on the selection procedure in more detail. Finally, some results and an evaluation of the effectiveness of the component mode selection procedure are given in Section 5.3. Throughout this chapter, the cantilever beam defined in Appendix A is used, where its parameters are given in Table A.3 (with component 1 thus being relatively flexible).

5.1 Error measure

In Equation (4.23), the assembly reduction error caused by component reduction errors which propagate through the assembly ($\boldsymbol{\Delta Y}^{(assy)}(\omega j)$) was approximated. Since this error indicates the reduction quality, it is used to compare the assembly reduction quality induced by various reduction bases. A disadvantage however is that $\boldsymbol{\Delta Y}^{(assy)}(\omega j)$ is a multi-input multi-output (MIMO) function of the frequency. To automatically rank reduction bases based on the quality of the associated reduced assembly, the information in $\boldsymbol{\Delta Y}^{(assy)}(\omega j)$ is therefore condensed into a single scalar variable for which two norm types are used as shown in Figure 5.1.

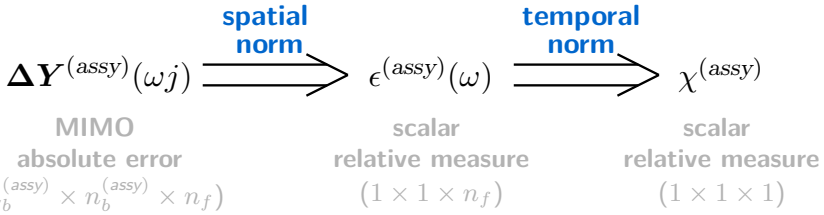

Figure 5.1: *Schematic overview of the procedure to determine the relative error measure by using spatial and temporal norms. Indicated between brackets are the dimensions of each variable/measure.*

First, a spatial (or matrix) norm of $\boldsymbol{\Delta Y}^{(assy)}(\omega j)$ is determined to obtain a 'frequency-dependent error measure' ($\epsilon^{(assy)}(\omega)$) at each evaluated frequency ω. As mentioned in Section 4.3.2, it would be preferred to evaluate a relative measure. This step therefore gives a relative measure instead of an absolute measure for the error. Since this measure is however still a function of the frequency, $\epsilon^{(assy)}(\omega)$ is condensed into a single value by using a temporal norm. This value is denoted by $\chi^{(assy)}$ and is used as the measure for the error, as used to compare the reduction quality of various reduction bases.

To illustrate the condensation from the multi-dimensional error to a single value, Figure 5.1 gives the dimensions of the different variables between parentheses. Here, $n_b^{(assy)}$ equals the number of unique boundary DOFs (which represent the POIs) in the assembly, and n_f is the number of frequencies at which the assembly error is evaluated. It should be noted that, normally, the assembly receptance matrix obtained by the LM FBS method contains the interface-related DOFs twice (once for each component related to a specific interface) [16]. Because of this, the transfers related to the interface DOFs are weighted twice in the calculation of the spatial norm and the size of $\boldsymbol{\Delta Y}^{(assy)}$ would be $n_{sum,b}$. Therefore, these transfers are taken in into account only once, causing the size to be $n_b^{(assy)}$. In the following subsections, the implementation of both norm types are discussed in detail.

5.1.1 Spatial norm

The goal of the spatial norm is to condense the information of the MIMO error to a single value per evaluated frequency. This is done by using matrix norms. For the specific case presented in this thesis, the Frobenius norm is chosen, since this norm takes the information of all elements in the matrix into account with equal weight (see Appendix C.1.3). An other choice for the matrix norm, such as the induced 2-norm, could also have been chosen. Although this norm type does not represent the combined error of all elements, the induced 2-norm and Frobenius norm can be relatively similar, as is explained in Appendix C.1.4.

As is shown in

$$\epsilon^{(assy)}(\omega) = \frac{\left\| \boldsymbol{\Delta Y}^{(assy)}(\omega j) \right\|_F}{\left\| \boldsymbol{Y}^{(assy)}(\omega j) \right\|_F}, \tag{5.1}$$

a relative error measure which compares the matrix norm of the (approximated) error to the matrix norm of the unreduced transfer function, is used. The use of this relative measure is motivated by the fact that comparing absolute errors does not provide a fair comparison over the entire frequency range, as was discussed in Section 4.3.2. The approach to determine a relative measure for a MIMO error as presented here, is adopted from the work of Makhavikou [22].

If some specific transfers are of relatively high importance in a particular assembly, point of interest weighting can be applied. For this, the errors corresponding to these transfer functions are amplified by using the Hadamard product of $\boldsymbol{\Delta Y}^{(assy)}$ and some POI-weighting matrix before calculating the matrix norm. By amplifying the transfers of 'high-interest', the error measure is made more sensitive to errors in these transfers. As a result hereof, the selection procedure will select modes such that the transfers related to these POIs are approximated more accurately compared to transfers related to other POIs. Although the potential for this option is posed here, POI weighting has not been implemented in this research.

Another important remark is that, because of its MIMO nature, the receptance matrix typically contains transfers with fundamentally different units. The demonstrator beam for example, contains both translations and rotations. As a result, the elements in the receptance matrix have different units. Because of this, there can be fundamental differences in the order of magnitude of these transfers, where some transfers (between variables with specific units) are dominant. Although this problem can not be completely circumvented, it can (partly) be solved by using scaling of the individual elements of the receptance matrices, as is discussed in Appendix C.3. A different approach would be to take only one specific type of transfer into account for the error measure (e.g., the force-to-displacement transfers). In this thesis, the former strategy is used however.

With respect to the computational efficiency of the relative error measure, the use of the unreduced assembly receptance in Equation (5.1) is unfavorable. There are however situations in which it is justified to spend more time on finding an improved reduction basis, e.g., time integration applications and acquisition of insight. This issue could however be solved by using some pre-reduced assembly receptance matrix (instead of the unreduced receptance) that is obtained by using a coarse cutoff approach which reduces the system, but leaves plenty modes from which an optimal kept set can be selected. Since this solution is however not as accurate as using the unreduced receptance and $\boldsymbol{Y}^{(assy)}$ is relatively inexpensive to calculate for the (simple) demonstrator beam, the unreduced assembly receptance is used in this thesis.

5.1.2 Error measure

The next step is to condense the frequency-dependent error measure ($\epsilon^{(assy)}(\omega)$) to a single scalar value. For this a temporal norm is used, which is a type of vector norm where the vector contains the frequency-dependent information of $\epsilon^{(assy)}$ along its length. Again, multiple types of vector norms can be used. Since the 2-norm gives some energy measure for the error, this type is used in this thesis. For more information on vector norms, the reader is referred to Appendix C.1.1. The implementation of the 2-norm is shown in

$$\chi^{(asssy)} = \left\| \epsilon^{(assy)}(\omega) \right\|_2 , \tag{5.2}$$

which gives a definition for the assembly error measure $\chi^{(assy)}$:

Similar to the POI-weighting discussed in the previous subsection, weighting for the frequency can be implemented as well. This is done by amplifying $\epsilon^{(assy)}$ at certain frequency ranges. In this thesis, brick wall filtering is used. This simple type of filtering cuts of all frequency signals below or above a user-defined frequency range of interest (FROI). Information outside this range is thus excluded from the computation of the temporal norm. More elaborate weighting options (e.g., using low-pass or notch filters) are also possible, but their implementation is left for further research.

5.2 Selection procedure

Since the goal of this thesis is to find a selection of kept vibration modes that results in improved (Hintz-Herting) component reduction bases, the optimal strategy would be to analyze all possible combinations of vibration modes and choose the combination which induces the lowest measure ($\chi^{(assy)}$) for the approximated assembly error. Due to the large amount of possible combinations,

this is however not computationally feasible. Therefore, the relevance of each individual non-rigid component eigenmode to the assembly is evaluated. For this, similar to Section 4.3.2, approximated assembly errors caused by omitting one component mode from the reduction bases are compared. Here, the approximated assembly error when mode $\boldsymbol{\phi}_k^{(c)}$ is truncated from the component reduction basis, is given by $\boldsymbol{\Delta Y}^{(assy)}_{\boldsymbol{\phi}_k^{(c)}}(\omega j)$. Consequently, the error measure resulting from the truncation of $\boldsymbol{\phi}_k^{(c)}$ is denoted by $\chi^{(assy)}_{\boldsymbol{\phi}_k^{(c)}}$.

Figure 5.2 shows a direct extension of the roadmap in Figure 4.4, where $\boldsymbol{\Delta Y}^{(assy)}$ was determined. This figure presents the steps needed to determine which component eigenmodes should be included in the improved reduction bases. The first step is to determine the error measure for all individual component modes. These corresponding error measures can then be ranked. The resulting arrangement shows which component modes induce the highest assembly errors if these are truncated. Since, in the end, the assembly reduction error should be as small as possible, the first $n_{\mathcal{K}}^{(assy)}$ eigenmodes in this ranking should be kept (such that the relatively high errors induced by the truncation of these modes are not induced in the reduced assembly). Note that since the $n_{\mathcal{K}}^{(assy)}$ kept modes are related to various components, the sets of kept modes are defined per component and denoted by $\boldsymbol{\Phi}^{(c)}_{\mathcal{K},im}$ (where '*im*' stands for 'improved'). These modes are finally used to calculate the condensed vibration modes as used in the improved HH reduction bases (see Equation (2.47)).

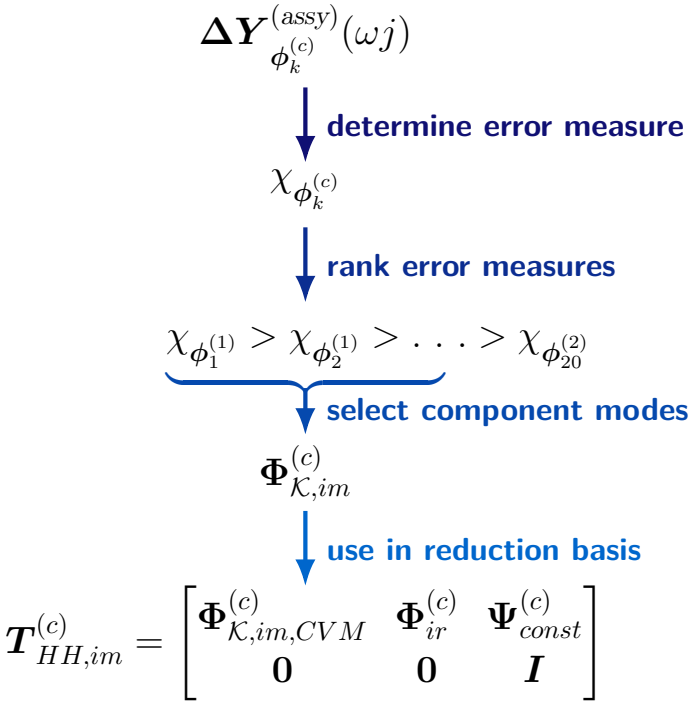

Figure 5.2: *Roadmap for the component mode selection procedure.*

Note that it is possible that the procedure given above suggests that no non-rigid eigenmodes of a specific component should be kept. Although not obvious, this is possible due to the inertia relief and constraint modes used alongside the condensed vibration modes in the Hintz-Herting technique. The reduced component model is thus at least as large as the total number of inertia relief and constraint modes.

Finally, it is (again) stated that the propagated error is approximated. Because of this, the mode selection procedure introduced in this section gives an estimation of an optimal choice of modes.

As is shown in Equation (5.3), the sum of the approximated assembly errors for individually truncated modes (right side of Equation (5.3)) equals the approximated assembly error when both modes are truncated simultaneously (left side):

$$\boldsymbol{\Delta Y}^{(assy)}_{\boldsymbol{\phi}_1^{(1)}+\boldsymbol{\phi}_2^{(1)}}(\omega j) = \boldsymbol{\Delta Y}^{(assy)}_{\boldsymbol{\phi}_1^{(1)}}(\omega j) + \boldsymbol{\Delta Y}^{(assy)}_{\boldsymbol{\phi}_2^{(1)}}(\omega j). \tag{5.3}$$

This linear sum does however not hold for norms of these approximated errors:

$$\epsilon^{(assy)}_{\boldsymbol{\phi}_1^{(1)}+\boldsymbol{\phi}_2^{(1)}}(\omega) \leq \epsilon^{(assy)}_{\boldsymbol{\phi}_1^{(1)}}(\omega) + \epsilon^{(assy)}_{\boldsymbol{\phi}_2^{(1)}}(\omega). \tag{5.4}$$

Proofs for Equations (5.3) and (5.4) are given in Appendix B.6. Now, using Equation (5.2), it is easy to show it holds that:

$$\chi^{(assy)}_{\boldsymbol{\phi}_1^{(1)}+\boldsymbol{\phi}_2^{(1)}} \leq \chi^{(assy)}_{\boldsymbol{\phi}_1^{(1)}} + \chi^{(assy)}_{\boldsymbol{\phi}_2^{(1)}}. \tag{5.5}$$

Since Equation (5.5) shows an inequality rather than an equality, it can not be guaranteed that the modes associated to the lowest possible sum of various error measures for multiple modes (obtained when these modes are omitted individually) also give the minimal error measure if they are all truncated simultaneously. In other words, the selection obtained using the proposed selection procedure does not necessarily lead to the minimal error measure for the reduced assembly.

This is explained by a hypothetical example where, if modes $\boldsymbol{\phi}_1^{(1)}$, $\boldsymbol{\phi}_2^{(1)}$, and $\boldsymbol{\phi}_3^{(1)}$ are left out,

$$\chi_{\boldsymbol{\phi}_1^{(1)}+\boldsymbol{\phi}_2^{(1)}+\boldsymbol{\phi}_3^{(1)}} \leq \chi_{\boldsymbol{\phi}_1^{(1)}} + \chi_{\boldsymbol{\phi}_2^{(1)}} + \chi_{\boldsymbol{\phi}_3^{(1)}}, \tag{5.6}$$

and, when modes $\boldsymbol{\phi}_1^{(1)}$, $\boldsymbol{\phi}_2^{(1)}$, and $\boldsymbol{\phi}_4^{(1)}$ are omitted:

$$\chi_{\boldsymbol{\phi}_1^{(1)}+\boldsymbol{\phi}_2^{(1)}+\boldsymbol{\phi}_4^{(1)}} \ll \chi_{\boldsymbol{\phi}_1^{(1)}} + \chi_{\boldsymbol{\phi}_2^{(1)}} + \chi_{\boldsymbol{\phi}_4^{(1)}}. \tag{5.7}$$

Here, truncating modes $\boldsymbol{\phi}_1^{(1)}$, $\boldsymbol{\phi}_2^{(1)}$, and $\boldsymbol{\phi}_4^{(1)}$ simultaneously results in an error measure which is much lower than when they are truncated individually.

Now, suppose that

$$\chi_{\boldsymbol{\phi}_1^{(1)}} + \chi_{\boldsymbol{\phi}_2^{(1)}} + \chi_{\boldsymbol{\phi}_4^{(1)}} > \chi_{\boldsymbol{\phi}_1^{(1)}} + \chi_{\boldsymbol{\phi}_2^{(1)}} + \chi_{\boldsymbol{\phi}_3^{(1)}}. \tag{5.8}$$

Since the improved selection procedure looks at the error measures when modes are individually truncated, modes $\boldsymbol{\phi}_1^{(1)}$, $\boldsymbol{\phi}_2^{(1)}$, and $\boldsymbol{\phi}_4^{(1)}$ would be selected. However, due to the '$\ll$' sign in Equation (5.7) it can be the case that when the modes are deleted simultaneously

$$\chi_{\boldsymbol{\phi}_1^{(1)}+\boldsymbol{\phi}_2^{(1)}+\boldsymbol{\phi}_4^{(1)}} < \chi_{\boldsymbol{\phi}_1^{(1)}+\boldsymbol{\phi}_2^{(1)}+\boldsymbol{\phi}_3^{(1)}}, \tag{5.9}$$

showing that, in this hypothetical example, keeping mode $\boldsymbol{\phi}_3^{(1)}$ instead of $\boldsymbol{\phi}_4^{(1)}$ would actually have been better. Therefore, even if the assembly errors would not be approximated, the proposed selection method is not guaranteed to provide the optimal set of kept eigenmodes. The hypothetical illustration shown here (and especially the '$\ll$' sign in Equation (5.7)) is however not very likely to be encountered in practice, as is evident from the potential of the improved selection method as presented in Section 5.3.

5.3 Results

In this section, the selection of component modes as discussed in the previous section is implemented for the demonstrator beam. To give some insight in the underlying decision making, in Section 5.3.1, some (frequency-dependent) error measures for a selection of truncated component modes are shown. These presented error measures are then ranked to select the most relevant component modes. Afterwards, in Section 5.3.2, the reduction error of the assembly obtained by using the improved selection is compared to when the traditional selection is used.

The results presented in this section are determined for the specific case where the error measure is defined for the points of interest depicted in Figure 5.3, and a frequency range of interest ranging from 0 to 32 Hz (unless stated otherwise).

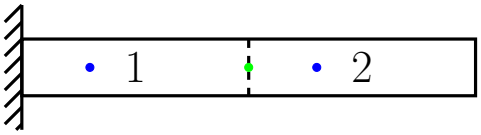

Figure 5.3: *POIs, used for the component mode selection procedure error measure. Here, the specific POIs are given by the retained (blue) and interface (green) nodes.*

5.3.1 Selected modes

Having determined the approximated assembly error of all individual component modes, the error measures caused by individually truncating modes $\boldsymbol{\phi}_1^{(1)}$, $\boldsymbol{\phi}_2^{(1)}$, $\boldsymbol{\phi}_1^{(2)}$, and $\boldsymbol{\phi}_2^{(2)}$ are plotted in Figure 5.4. In this figure, both the frequency-dependent result of the spatial norm ($\epsilon^{(assy)}(\omega)$) and the error measure ($\chi^{(assy)}$) are plotted.

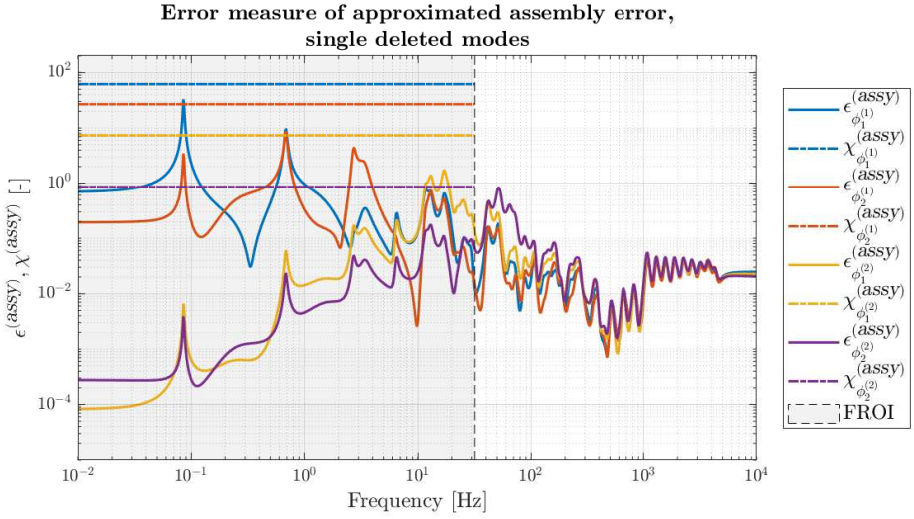

Figure 5.4: *Frequency-dependent results of the spatial norms and error measures ($\epsilon^{(assy)}$ and $\chi^{(assy)}$, respectively) for the approximated assembly errors obtained by deleting single component modes. Here, only the results for the individual deletion of $\boldsymbol{\phi}_1^{(1)}$, $\boldsymbol{\phi}_2^{(1)}$, $\boldsymbol{\phi}_1^{(2)}$, and $\boldsymbol{\phi}_2^{(2)}$ are shown. Also, the FROI ($0 - 32$ Hz) is indicated by the highlighted area.*

The frequency-dependent error measures in Figure 5.4 show that both modes of component 1

induce much larger relative error measures than the modes of component 2 in the frequency range of interest. Furthermore, since the first peak of the first mode of component 1 is higher than any of the peaks of the other modes, based on the comparison of $\epsilon^{(assy)}$ for all modes, mode $\boldsymbol{\phi}_1^{(1)}$ would be the 'most-relevant' mode to keep. Comparison of the error measures ($\chi^{(assy)}$), results in the same conclusion, since the dashed blue line (indicating the error measure for the truncation of $\boldsymbol{\phi}_1^{(1)}$) lies above any of the other dashed lines. The error measures related to the 4 modes shown in Figure 5.4 and all other non-rigid eigenmodes of both components are listed in Table A.5 in Appendix A.2. This table also includes the eigenfrequencies associated to each mode, since these are used for the traditional component mode selection procedure.

The 13 component modes causing the highest error measures are ranked in descending order of 'relevance' in the "improved approach" row in Table 5.1. The modes are also ranked by their associated eigenfrequencies (as would traditionally have been done) as tabulated in the "traditional approach" row in Table 5.1. The strategy for selecting the $n_{\mathcal{K}}^{(assy)}$ most important modes for either approach, is to keep the first $n_{\mathcal{K}}^{(assy)}$ modes in the corresponding row in Table 5.1. For example, if $n_{\mathcal{K}}^{(assy)} = 3$, the traditional method would keep modes $\boldsymbol{\phi}_1^{(1)}$, $\boldsymbol{\phi}_2^{(1)}$, and $\boldsymbol{\phi}_3^{(1)}$, whereas the improved method would keep modes $\boldsymbol{\phi}_1^{(1)}$, $\boldsymbol{\phi}_2^{(1)}$, and $\boldsymbol{\phi}_5^{(1)}$.

Table 5.1 shows a similar trend for the improved and traditional ranking of component modes; eigenmodes with low frequencies are regarded as relatively important. If for example only 6 non-rigid modes are kept ($n_{\mathcal{K}}^{(assy)} = 6$), the sets of kept modes obtained by both approaches are identical. In this specific case, the reduced (assembly) models are thus identical as well. Clear differences between both methods can also be recognized however. For instance, some component modes are deemed more important in the improved approach. An example hereof is mode 5 of component 1, which would be the fifth mode to keep according to the traditional mode, but is the third mode of choice in the improved method. Also, the final mode (mode 20) of component 1 is the 8^{th} mode of choice in the improved method, which is quite remarkable since this mode would be the 27^{th} mode of choice in the traditional approach.

Table 5.1: *Ranking of the 13 most relevant non-rigid eigenmodes of both components, based on the traditional (cutoff) approach and the improved (error measure) approach. The error measures are determined for the POIs depicted in Figure 5.3 and the FROI = 0 − 32 Hz.*

Ranking of component eigenmodes		1	2	3	4	5	6	7	8	9	10	11	12	13	⋯
Traditional method	component	1	1	1	1	1	2	1	1	1	2	1	1	1	
	mode	1	2	3	4	5	1	6	7	8	2	9	10	11	
Improved method	component	1	1	1	1	1	2	1	1	1	1	1	1	1	
	mode	1	2	5	3	4	1	8	20	6	7	11	12	14	

5.3.2 Reduced assembly quality

In this section, the quality of the reduced assembly receptances obtained by using Hintz-Herting reduction bases where different non-rigid eigenmodes are selected by using the traditional and improved selection method, is compared. To assess the reduction quality, the (exact) reduction error of the assembly is given by

$$\boldsymbol{E}^{(assy)} = \boldsymbol{Y}^{(assy)} - \hat{\boldsymbol{Y}}^{(assy)}. \tag{5.10}$$

Since this error is a multidimensional matrix and a function of the frequency, a scalar error measure is again required in order to directly compare all MIMO errors. For this, the same procedure as discussed in Section 5.1 is used, where the (relative) spatial norm is given by

$$\epsilon^{(assy)}(\omega) = \frac{\left\| \boldsymbol{E}^{(assy)}(\omega j) \right\|_F}{\left\| \boldsymbol{Y}^{(assy)}(\omega j) \right\|_F}, \tag{5.11}$$

and the temporal norm is again defined by Equation (5.1). Since the error measures used for the mode selection are specified for a particular FROI and set of POIs, the error measure for the exact assembly error is calculated using the same FROI and POIs.

Now, suppose that an example is investigated where the dynamical assembly behavior is to be approximated accurately up to 32 Hz (FROI $= 0 - 32$ Hz). Traditionally, a rule of thumb is used that all component modes with frequencies up to 2.5 times the maximal frequency of the FROI are kept for the component reduction bases. For the cantilever beam used here (of which the parameters are given in Table A.3), there are 11 component modes with eigenfrequencies lower than $32 \cdot 2.5 = 80$ Hz. Therefore, according to the traditional method, these 11 modes should be kept. However, if the selection is performed by the improved technique, 11 (partly) different modes are chosen (as has already been shown in Table 5.1). In Figure 5.5, $\epsilon^{(assy)}(\omega)$ and $\chi^{(assy)}$, resulting from the implementation of both methods, are compared.

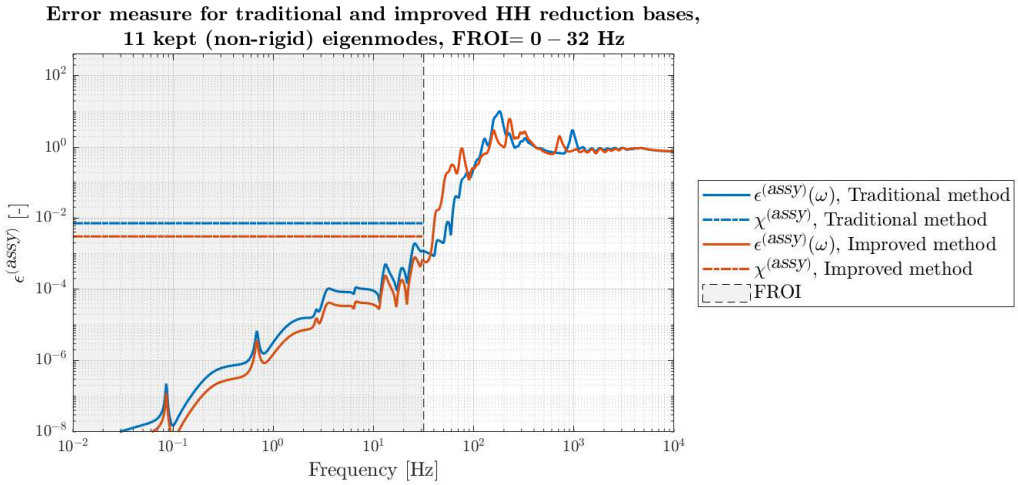

Figure 5.5: *Error measure (where the FROI $= 0 - 32$ Hz) and $\epsilon^{(assy)}$ for the assembly error obtained by using HH reduction bases where 11 non-rigid component eigenmodes are chosen using the traditional method (blue) and the improved method (red).*

This figure shows that the improved selection method indeed results in a lower error measure for the actual assembly reduction, as is apparent from the dashed red line which lies below the blue dashed line. Comparing the frequency-dependent measures ($\epsilon^{(assy)}$) also shows that, for this choice of POIs and FROI, the selection of component modes obtained by using the new selection method is indeed an improvement with respect to the conventional approach.

Inspecting Figure 5.5 shows that $\epsilon^{(assy)}$ increases for higher frequencies. Because of this, the frequency-dependent error measure at the end of the FROI dominates in the calculation of $\chi^{(assy)}$ (given by the 2-norm of $\epsilon^{(assy)}(\omega)$). A method that manages to suppress the assembly reduction error at the end of the FROI will therefore perform well for this definition of the error measure.

It is also interesting to see that, almost directly above the FROI, the improved method actually performs worse than the traditional method. Decreasing the error in the FROI thus comes at a cost of increasing the error outside the FROI. Since the error should be minimized in the FROI only however, this is not an issue. To conclude, the application of the improved method shown in Figure 5.5 demonstrates that the improved method is able to find a more accurate reduction basis than traditionally used component reduction bases, while having the same amount of DOFs.

An alternative use of the improved selection method is to find an improved reduction basis which is equally accurate as the traditional method, but consists of less degrees of freedom, resulting in a more efficient reduced model. An example hereof is shown in Figure 5.6. In this figure, we compare the error measure for the assembly error obtained by using 11 modes which are selected according to the improved method to the error measure obtained using 13 modes which are selected using the traditional approach. Clearly, although using different amounts of modes, very similar error measures are obtained. In fact, the error measure for the improved method is even slightly lower than that of the traditional method. This can be verified by looking at Table A.6, where the values of all reduced assembly error measures shown in this section are tabulated.

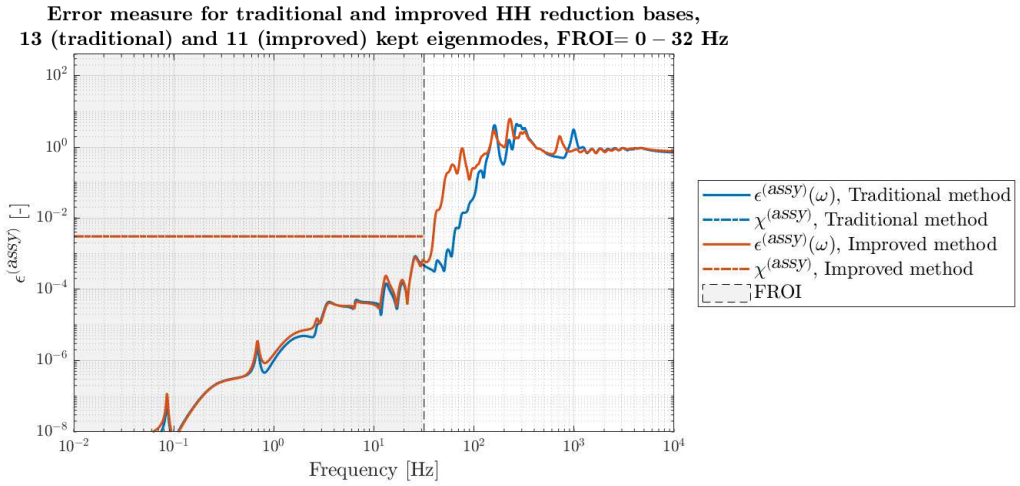

Figure 5.6: *Error measure (where the FROI* $= 0 - 32$ *Hz) and* $\epsilon^{(assy)}$ *for the assembly error obtained by using HH reduction bases where 13 non-rigid component eigenmodes are chosen using the traditional method (blue) and only 11 non-rigid eigenmodes using the improved method (red).*

Since besides the kept modes, also some constraint and inertia relief modes are used in the HH reduction bases, the total number of DOFs in the assembly is the sum of the amount of DOFs caused by these additional modes and the number of kept vibration modes. For the example given in Figure 5.6, the number of DOFs in the assembly are tabulated per mode type in Table 5.2. Here, it can be seen that, by using the improved selection method, the total number of DOFs of the assembly is reduced by 11.8 %, while maintaining the same accuracy.

Table 5.2: *Breakdown of the origin of the number of DOFs in the assembly, caused by specific (Hintz-Herting) mode types in the component reduction bases.*

Mode type	Traditional	Improved
Constraint modes	2	2
Inertia relief modes	2	2
Kept non-rigid eigenmodes	13	11
Total number of degrees of freedom in assembly	17	15

A third application of the improved selection method, which is relatively similar to that mentioned for Figure 5.5, is to choose any user-defined number of kept eigenmodes such that the assembly reduction error is 'minimized'. Figure 5.7 shows this for the case where 3 modes are chosen. Again, the improved method results in the preferred reduction bases.

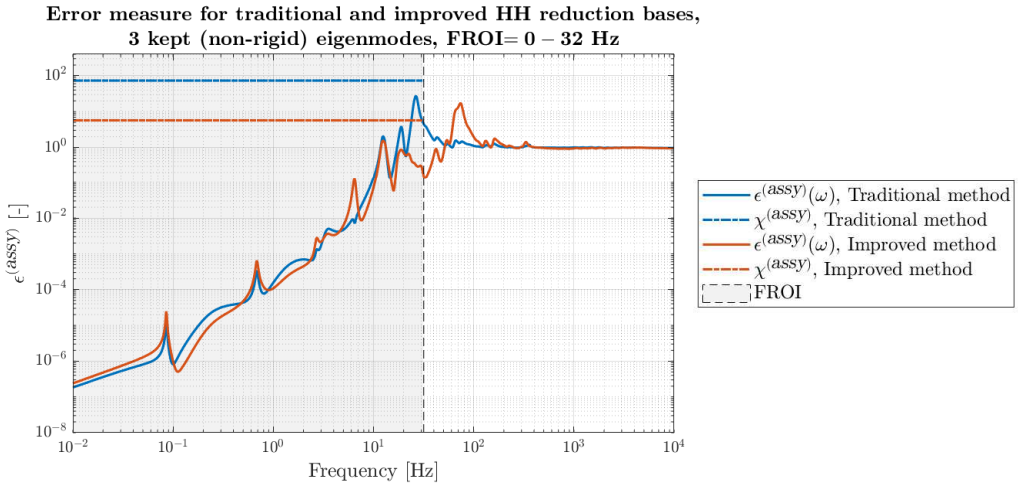

Figure 5.7: *Error measure (where the FROI* $= 0 - 32$ *Hz) and* $\epsilon^{(assy)}$ *for the assembly error obtained by using HH reduction bases where 3 non-rigid component eigenmodes are chosen using the traditional method (blue) and the improved method (red).*

Improved reduction bases can also be found for different FROIs than the FROI used in the above analyses. In order to select modes for a different FROI, the error measures (to be specific, the temporal norms) have to be calculated and ranked again for this new FROI however. Table 5.3 shows the resulting ranked modes if FROI $= 0 - 80$ Hz. Note that, for the improved selection method, there are some subtle differences with respect to what modes were previously chosen and listed in Table 5.1. The traditional ranking does however not change, since this method bases its ranking solely on the eigenfrequencies of the component modes, disregarding any POIs and FROI. Selecting the first 3 modes in Table 5.3 for both methods and analyzing the assembly error in the updated FROI, results in Figure 5.8, where the improved method again gives rise to a lower measure for the assembly reduction error.

Table 5.3: *Ranking of the 13 most relevant non-rigid eigenmodes of both components, based on the traditional (cutoff) approach and the improved (error measure) approach. The error measures are determined for the POIs depicted in Figure 5.3 and the FROI* $= 0 - 80$ *Hz.*

Ranking of component eigenmodes		1	2	3	4	5	6	7	8	9	10	11	12	13	⋯
Traditional approach	component	1	1	1	1	1	2	1	1	1	2	1	1	1	
	mode	1	2	3	4	5	1	6	7	8	2	9	10	11	
Improved approach	component	1	1	1	1	1	1	2	1	1	1	1	2	1	
	mode	1	2	5	3	4	8	1	11	20	7	6	2	9	

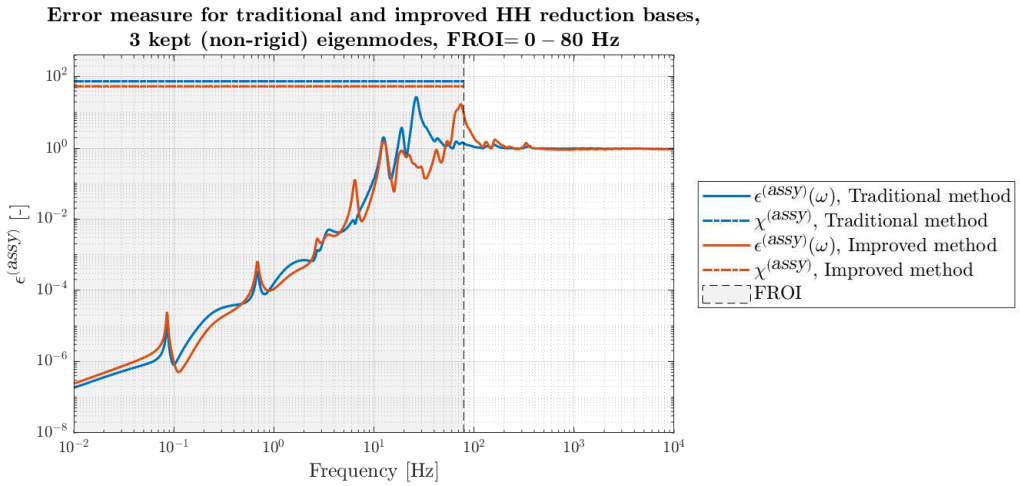

Figure 5.8: *Error measure (where the FROI* $= 0 - 80$ *Hz) and* $\epsilon^{(assy)}$ *for the assembly error obtained by using HH reduction bases where 3 non-rigid component eigenmodes are chosen using the traditional method (blue) and the improved method (red).*

Finally, as discussed at the end of Section 5.2, the proposed approach for selecting component modes is not guaranteed to result in an optimal choice of vibration modes for the reduction bases of the components. This is for example shown in Figure 5.9, where 8 modes are used (with FROI $= 0 - 32$ Hz). For this specific case, the error measure for the reduced assembly obtained using the traditional method is smaller than the measure obtained by using the 'improved' method, showing that the improved method does not always provide a better selection of component modes. This is explained by either one or a combination of the following causes: the approximate nature of the assembly error, the definition/use of the error measure, and the issue discussed in Equations (5.4) and (5.5). The localization of the exact cause is however left for further research.

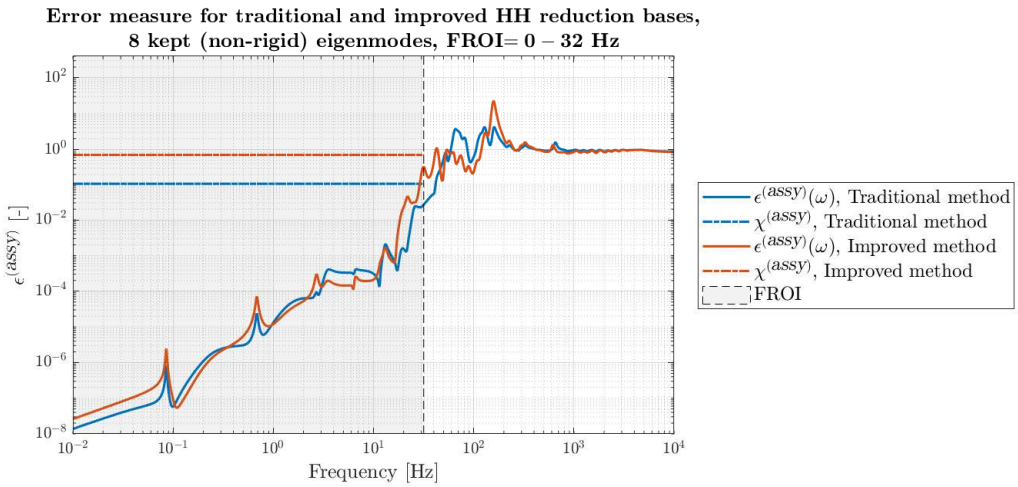

Figure 5.9: *Error measure (where the FROI* $= 0 - 32$ *Hz) and* $\epsilon^{(assy)}$ *for the assembly error obtained by using HH reduction bases where 8 non-rigid component eigenmodes are chosen using the traditional method (blue) and the improved method (red).*

Although good results are obtained, as is illustrated by Figure 5.9, the improved method does not guarantee an improved reduced assembly. Overall however, the differences between $\epsilon^{(assy)}$, resulting from the traditional and improved methods, observed throughout this section are relatively small. It would for this reason be very interesting to implement the improved method for more complex structures, as these are more likely to have modes with local behavior. Such modes can either be very important or almost irrelevant for the dynamical behavior at specific POIs. While the traditional method would heedlessly keep some of these irrelevant modes for the mere reason that they happen to have low associated eigenfrequencies, the improved selection method should be able to recognize the (ir)relevance of local modes. Therefore, it is expected that, for such applications, the improved selection method will outperform the traditional method. It should however also be mentioned that for large systems not all modes can be calculated and hence analyzed for the selection criterion. This can however be solved by using a coarse pre-reduction using a cutoff approach which lowers the amount of modes to an amount that can be calculated (as was already briefly discussed in Section 5.1.1).

Finally, to tackle the reliability issue of the improved component mode selection procedure, a different selection strategy could be adopted. Since the current method chooses all modes at the same time by only evaluating the errors when these modes are deleted individually, the effect modes have on each other is not taken into account. Since this mutual influence can be relevant however, an iterative selection procedure is proposed. This procedure uses $n_{\mathcal{K}}^{(assy)}$ evaluation iterations, where in each iteration only one (additional) mode that should be kept is chosen. In each iteration, the effect of eigenmodes selected in previous iterations is taken into account by evaluating which additional truncated mode induces the largest error if these already selected modes are truncated as well. As an illustration, suppose that, in the first iteration (which is equivalent to the calculation of the assembly reduction error induced by omitting individual component modes as used in the rest of this section), omitting $\boldsymbol{\phi}_1^{(1)}$ causes the highest assembly error. Then, in the next iteration, the assembly errors induced by truncating the combination of $\boldsymbol{\phi}_1^{(1)}$ and a single other component eigenmode are approximated for all remaining eigenmodes. Now, suppose that ranking these assembly errors gives the insight that the combination of modes $\boldsymbol{\phi}_1^{(1)}$ and $\boldsymbol{\phi}_3^{(1)}$ induces the largest. In the next iteration, a similar evaluation is then performed where the third mode is determined. This process is repeated until $n_{\mathcal{K}}^{(assy)}$ modes are selected. Since, in each iteration, the error caused by the simultaneous truncation of multiple

modes is evaluated, this procedure takes the effects modes have on each other into account. A major disadvantage of this method is however that it goes paired with a (very) large increase in computation time for the selection procedure (depending on the number of modes to keep). Although this procedure is not implemented in this thesis, further research on this method is encouraged.

Chapter 6

Conclusions & Recommendations

6.1 Conclusions

In this thesis, the reduction of assembly models is investigated in a dynamic substructuring context. to this end, an assembly is divided in components which are reduced individually. The reduction of components is performed using component mode synthesis, where truncation of the vibration modes lowers the amount of degrees of freedom of a component. Afterwards, the reduced components are coupled such that a reduced assembly model is obtained. Traditionally, for the selection of component modes, eigenmodes are ranked based on their eigenfrequencies. Since, if the behavior of an assembly is to be approximated accurately, this is not expected to be the optimal strategy, this thesis aimed at finding a method with which this selection is optimized. Multiple methods are investigated to achieve this goal.

The error bound propagation method analyzes the propagation of bounds on the errors of the transfer functions of the uncoupled components. Using these component error bounds in combination with a 2-component feedback representation of a system enables to find a bound on the reduction error of an assembly transfer. This bound gives a measure for the quality of the reduced assembly (as obtained using DS) when specific component reduction bases are used to reduce the components. By comparing these bounds for different reduction bases the best bases can potentially be identified. In order to use the expression for the bound on the assembly error however, the small gain condition needs to hold. For mechanical systems, this proves to be difficult due to an inverse relationship between the transfer functions (constituting the feedback loop) of both components. Because of this, the location of the interface is decisive in meeting the small gain condition. Another disadvantage is that writing a system consisting out of more than 2 subsystems in a feedback form (as required for this method) is difficult. Due to this limited applicability, alternative component error propagation methods have been investigated.

A different method to assess the propagation of component errors is to use the LM FBS expression for the assembly receptance. Here, it is attempted to find an expression for the assembly error in terms of the receptance contributions of individual component modes. Due to the explicit coupling at the interface, this is however not possible. Instead, the assembly error is written in terms of error contributors. Analysis of these contributors for the demonstrator beam shows that the errors at the interfaces dominate the assembly error. For an automated component mode selection procedure, writing the assembly error in terms of error contributors is not beneficial however, since this insight does not indicate which specific component eigenmodes should

be retained or truncated, while it does increase the computational effort needed to compute the assembly error.

The third method method, which is also based on the LM FBS method, approximates how component errors propagate through an assembly. The goal of this method is to increase the efficiency of the computation of the assembly error. This approximation is facilitated by using a first-order Taylor approximation for the assembly error. For this, the partial derivative of the LM FBS expression with respect to uncoupled component receptance(s) was utilized.

For the sensitivity-based propagation method, the component errors is estimated in order to improve the efficiency. For this, a technique is used which uses modal receptance contributions of individual component modes. For a modal truncated component, the estimated error is exact. Therefore, these 'estimated' errors are used to determine improved modal truncation reduction bases. Since the Hintz-Herting method (which is used in order to assemble the components) uses the same free-boundary vibration modes as the modal truncation technique, it is assumed that the (non-rigid) eigenmodes found for such an improved MT reduction basis are also the eigenmodes that should be used for an improved HH reduction basis.

Since the influence of distinctive component modes on the assembly is to be investigated, an approach is adopted where the approximated assembly error caused by truncating individual component modes is computed. By using both spatial and temporal norms, (relative) error measures are calculated for transfers between specific points of interest and for a specific frequency range of interest. These measures are then used to rank assembly errors obtained by truncating different eigenmodes. By using this ranking, a set of most relevant eigenmodes is selected per component, which is different from the set of eigenmodes which would traditionally have been retained based on the eigenfrequencies.

Finally, the quality of the reduced assemblies, obtained by using the improved and traditional selection methods, has been compared. In order to compare the quality of the reduced assemblies for specific points of interest and for a specific frequency range of interest, error measures are again used. Although no guarantee can be given that the proposed selection method always improves the reduction quality of the assembly, application of this method to the demonstrator shows the potential of the proposed selection method. For example, applications where this selection method results in lower (measures for the) assembly errors for the selected POIs and FROI are shown. Other applications show that using the improved eigenmode selection enables to reduce the assembly with less DOFs than the traditional approach, while having an equivalent reduction error (measure), hence resulting in a more efficient reduced model of the assembly.

The improved method can thus be used to select a user-defined number of eigenmodes, such that the reduced assembly model is improved in terms of accuracy and/or efficiency (compared to the traditional approach). Besides these applications, the relevance of the individual component modes also gives insight in which component modes have important influences on specific assembly behavior. If, for example, vibrations at specific points of the assembly are to be minimized, the acquired knowledge can pinpoint which modes of the uncoupled components provoke this behavior. By using this information in the design of the individual components, it is expected that the performance of the assembly can be improved.

6.2 Recommendations

In this chapter, some of the challenges which have not yet been tackled in this research are listed. Furthermore, promising ideas, related to the techniques shown in this thesis, which came to mind, are mentioned below. It is encouraged that further research is conducted on these topics.

- **Application of the error bound propagation technique to different system types**
  As discussed in Chapter 3.3, the error bound propagation method can not be used for a large class of mechanical systems since these do not satisfy the small gain condition. The error bound propagation method might however have potential for other types of systems, which are more likely to meet the small gain condition (e.g., thermal systems).

- **Different error measure options and weighting**
  One important aspect of the selection procedure proposed in this thesis is the definition of an error measure to rank multiple reduction errors quickly and efficiently. As mentioned in Section 5.1, it was discussed that multiple types of norms can be used for this definition. Therefore, the question arises if the employed selection method will also be able to improve reduction bases if different definitions of the error measure are used.

  Furthermore, as mentioned in Section 5.1, there is a possibility to implement point of interest and frequency weighting which has not been (fully) explored yet.

- **Implementation of the relative error (measure)**
  As discussed in Section 5.1.1, in order to determine the relative measure for the approximated assembly error, the unreduced receptance matrix of the assembly is required. As an alternative, the relative errors of the components could however also be used. This is allowed since the sensitivity of the assembly receptance matrix, which is used to propagate the (relative) component error, is dimensionless and therefore merely represents a kind of amplification. One advantage of this approach is that the unreduced component receptance is, from a computational point of view, cheaper to use than the unreduced assembly receptance.

  This technique would simultaneously solve the scaling issue; since the component errors are already in a relative form, the assembly error is in relative form as well. Because of this, there is no difference in the order of magnitude between different elements of the receptance matrices when the spatial norm is determined.

- **Cause of relevance of component modes for the assembly**
  In this research, the focus has been on the selection of component modes. The exact cause of the relevance of specific component modes for the assembly has hereby been partly regarded as a black box concept. It would however be very beneficial if the exact characteristics that cause component modes to be relevant for the assembly are known and understood. As a starting point, one could use the knowledge that interface-related contributions are relatively important. It could for example be investigated how specific modes contribute to the behavior at the interfaces and what characteristics these modes have. To improve the mode selection technique these specific characteristics could be inspected, such that the relevant modes can be found in a more accurate and/or efficient fashion. Furthermore, this knowledge can be used to design components such that the assembled system has more favorable specifications.

- **Higher order approximation**
  To approximate the assembly error due to the propagation of component modes, a first-order Taylor approximation has been used in this thesis. Obviously, using higher-order Taylor terms results in more accurate approximations. Calculating these terms however comes at the cost of increased computation times. Therefore, the trade-off between an increase in accuracy and a decrease in efficiency should be investigated.

- **Iterative component mode selection procedure**
  As was discussed in Section 5.3.2, the reliability of the currently proposed selection procedure might be improved by the use of an iterative selection procedure. A description of this method has already been given at the end of Section 5.3.2. Implementing this method increases the computation time for the evaluation of the component mode selection significantly. For some applications this increase in computation time can be justified however (e.g., gaining insight in component influences on assembly level which can be used in the component design).

- **Benefits and limitations of implementation to large systems**
  Since, in this thesis, the formulated selection procedure has only been applied to a relatively simple system, it is advised to apply this technique to complex systems as well. It is namely expected that the selection procedure proposed here will perform particularly well for complex systems. This claim is based on the fact that complex (sub)systems are more likely to have relatively local behavior. Since the method proposed in this research is developed to identify the (ir)relevance of modes at specific POIs, it is expected that this method will perform better for such systems than for relatively simple systems in this regard. A disadvantage is however that, due to the increased size of the (sub)systems, it is much more demanding to evaluate the influence of all eigenmodes of all components, simply because there are too many. Therefore, a possible solution would be to use a pre-reduction step, which comes down to performing a coarse reduction in which a pre-selection of component modes is made. For the actual component mode selection, only modes with eigenfrequencies below some ample cutoff, would then be evaluated and selected.

- **Applicability to different classes of reduction techniques**
  Finally, this research was confined to a class of components which are reduced using component mode synthesis methods. The discussed propagation methods could however also be applied to components which are reduced using different reduction techniques (such as balanced model reduction, moment matching, etc.). It would be interesting to investigate such techniques, since each reduction technique has its own advantages. A disadvantage of which the user should be aware when implementing these techniques, is that the 'engineering insight' (in the form of modes), gained by the use of CMS, is potentially lost.

Bibliography

[1] Besselink, B. (2012). *Model reduction for nonlinear control systems with stability preservation and error bounds* (PhD thesis). Eindhoven University of Technology, Eindhoven, the Netherlands.

[2] Besselink, B., van de Wouw, N., and Nijmeijer, H. (2011). Model reduction of nonlinear systems with bounded incremental L2 gain. *IEEE Conference on Decision and Control and European Control Conference.*

[3] Besselink, B. et al. (2013). A comparison of model reduction techniques from structural dynamics, numerical mathematics and systems and control. *Journal of Sound and Vibration, 332*(19), 4403-4422.

[4] Buckingham, E. (1914). On physically similar systems; illustrations of the use of dimensional equations. *Physical Review, 4*(4), 345376.

[5] Bunatara, S.G. (2018). *An Isogeometric Approach to Beam Structures.* Koriyama, Fukushima, Japan: Springer.

[6] Craig, R., and Bampton, M. (1968). Coupling of Substructures for Dynamic Analysis. *AIAA Journal 6*, 7, 1313-1319.

[7] Dahleh, M. et al. (2011). *Lectures on Dynamic Systems and Control, Matrix Norms and Singular Value Decomposition.* Massachusetts Institute of Technology, Cambridge, United States.

[8] Duncan, W. (1941). The admittance method for obtaining the natural frequencies of systems. *Philosophical Magazine 32*, 401-409.

[9] Fey, R.H.B. (2017). *Structural Dynamics* (Lecture slides). Eindhoven University of Technology, Eindhoven, the Netherlands.

[10] Ford, W. (2015). *Numerical linear algebra with applications: using Matlab.* London, UK: Elsevier/AP.

[11] Gere, J. M., and Timoshenko, S. P. (1997). *Mechanics of Materials.* PWS Publishing Company.

[12] Glover, K. (1989). A Tutorial on Hankel-Norm Approximation. *From Data to Model*, 2648.

[13] Golub, G. H., van Loan, C.F. (1996). *Matrix Computations.* Johns Hopkins.

[14] Hepburn, C.J. (2000). *Britney Spears' Guide to Semiconductor Physics.* Retrieved from *http://britneyspears.ac/lasers.htm.*

[15] Herting, D. (1985). A general purpose, multi-stage, component modal synthesis method. *Finite Elements in Analysis and Design*, 1(2), 153-164.

[16] Klerk, de, D., Rixen, D.J., and de Jong, J. (2006). The Frequency Based Substructuring (FBS) Method reformulated according to the Dual Domain Decomposition Method. *Proceedings of the XXIV International Modal Analysis Conference, St. Louis, Missouri, United States.*

[17] Klerk, de, D., Rixen, D. J., and Voormeeren, S. N. (2008). General Framework for Dynamic Substructuring: History, Review and Classification of Techniques. *AIAA Journal,* 46(5), 1169-1181.

[18] Klerk, de, D., and Voormeren, S. (2010). Uncertainty Propagation in Experimental Dynamic Substructuring. *Mechanical Systems and Signal Processing, volume 24*, 106-18.

[19] Kraker, de, A. (2004). *A numerical-experimental approach in structural dynamics.* Eindhoven University of Technology, Eindhoven, the Netherlands.

[20] Kraker, de, A. (2009). *Mechanical Vibrations.* Eindhoven University of Technology, Eindhoven, the Netherlands.

[21] Liao, L. (2011). A Study of Inertia Relief Analysis. *52nd AIAA/ASME/ASCE/AHS/ASC Structures, Structural Dynamics and Materials Conference.*

[22] Makhavikou, V., Vlasenko, D., and Kasper R. (2014). *Method of model reduction for elastic multibody systems.* 11^{th} world congress on Computational Mechanics.

[23] Megretski, A. (2004). *Model Reduction, L2 gains and system approximation quality* (Lecture notes). Massachusetts Institute of Technology, Cambridge, United States.

[24] Minkowski, H. (1953). *Geometrie der Zahlen.* Chelsea Publishing Company, Vermont, United States.

[25] Neamen, D.A. (2012). *Semiconductor physics and devices: basic principles.* New York: McGaw-hill Higher Education.

[26] Rixen, D. J.(1997). *Substructuring and Dual Methods in Structural Analysis* (PHD thesis). Université de Liège, Liège, Belgium.

[27] Rixen, D. J. (2010). Substructuring using Impulse Response Functions for Impact Analysis. In *Proceedings of the IMAC - XXVIII, Jacksonville, Florida United States.*

[28] Skogestad, S., & Postlethwaite, I. (2010). *Multivariable feedback control: analysis and design.* Chichester: Wiley.

[29] Steenhoek, A. M., and Rixen, D. J. (2011). Truncation error propagation in model order reduction techniques based on substructuring. *Structural Dynamics, Volume 3 Conference Proceedings of the Society for Experimental Mechanics Series,* 663-677.

[30] Voormeren, S.N. (2007). *Coupling Procedure Improvement & Uncertainty Quantification in Experimental Dynamic Substructuring* (Msc thesis). Delft University of Technology, Delft, the Netherlands.

[31] Voormeren, S.N. (2012). *Dynamic Substructuring Methodologies for Integrated Dynamic*

Analysis of Wind Turbines (PhD thesis). Delft University of Technology, Delft, the Netherlands.

[32] Voormeeren, S. N., P. L. C. Van Der Valk, and Rixen, D. J. (2011). Generalized Methodology for Assembly and Reduction of Component Models for Dynamic Substructuring. *AIAA Journal, 49*(5), 1010-1020.

Appendix A

Demonstrator beam

A.1 Description

Below, the cantilever beam that is used throughout this thesis is described in more detail. The beam is divided in two components of equal length, as shown in Figure A.1. Each component is subdivided in 10 identical linear elements, resulting in 11 nodes, which is allocated to a specific node type. Constraint nodes are nodes that are constrained by boundary conditions. Interface nodes are, as the name suggests, located at the interfaces of components and used to ensure the coupling conditions (see Section 2.2.1). Furthermore, points of interest (nodes at which forces are applied or displacements are measured) are referred to as retained nodes. The combination of interface and retained nodes are also referred to as boundary nodes. Finally, all remaining nodes are called internal nodes and are typically the nodes that are reduced. These node-types and their associated color-code, as used in (among others) Figure A.1, are summarized in Table A.1. Also included in this table are the number of nodes in each component, categorized by type.

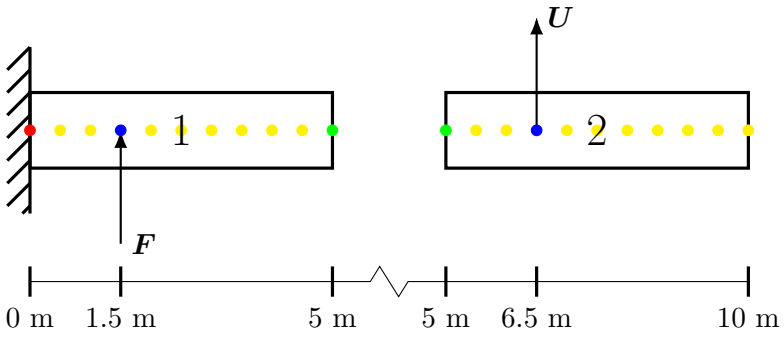

Figure A.1: *Schematic representation of a two-component cantilever beam with input at component 1 and output at component 2. The nodes of each component are indicated by (color-coded) dots.*

Table A.1: *Number of nodes per demonstrator component, sorted by type and including the color code as used in, for example, Figure A.1.*

Node-type	Color-code	Component 1	Component 2
Constraint	red	1	0
Interface	green	1	1
Retained	blue	1	1
Internal	yellow	8	9
Total		11	11

The cantilever beam displayed in Figure A.1 is modeled using 2D Euler beam elements of which the element mass and stiffness matrices are defined in Equations (A.1a) and (A.1b), respectively [5]. In these equations, E, I, ρ, A, and l represent the Young's modulus, area moment of inertia (around the neutral axis), density, cross-sectional area, and length of the beam elements, respectively. Since Euler beam elements are used where elongation of the beam is not taken into account, there are two degrees of freedom per node (displacement in the y-direction and rotation around the z-axis. This is also shown in Figure A.2, where an Euler beam element is shown with sign conventions of the DOFs at both nodes of the element, conform the definitions of $\boldsymbol{K}^{(e)}$ and $\boldsymbol{M}^{(e)}$. The corresponding element displacement/rotation and force/moment vectors ($\boldsymbol{u}^{(e)}$ and $\boldsymbol{F}^{(e)}$ respectively), are given in Equation (A.1c). When a cantilever beam is formed using the element matrices, it should be noted that due to the constraint at the left side of component 1, the degrees of freedom related to this constraint node are omitted from the component mass and stiffness matrices. Therefore, the actual size of the system matrices for component 1 is only 20.

$$\boldsymbol{K}^{(e)} = \frac{EI}{l^3}\begin{bmatrix} 12 & 6l & -12 & 6l \\ 6l & 4l^2 & -6l & 2l^2 \\ -12 & -6l & 12 & -6l \\ 6l & 2l^2 & -6l & 4l^2 \end{bmatrix} \tag{A.1a}$$

$$\boldsymbol{M}^{(e)} = \frac{\rho Al}{420}\begin{bmatrix} 156 & 22l & 54 & -13l \\ 22l & 4l^2 & 13l & -3l^2 \\ 54 & 13l & 156 & -22l \\ -13l & -3l^2 & -22l & 4l^2 \end{bmatrix} \tag{A.1b}$$

$$\boldsymbol{u}^{(e)} = \begin{bmatrix} u_1 \\ \varphi_1 \\ u_2 \\ \varphi_2 \end{bmatrix} \quad \text{and} \quad \boldsymbol{F}^{(e)} = \begin{bmatrix} F_1 \\ M_1 \\ F_2 \\ M_2 \end{bmatrix} \tag{A.1c}$$

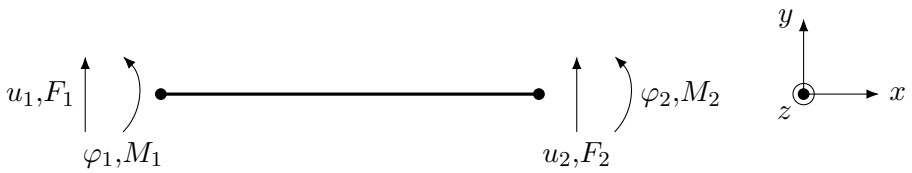

Figure A.2: *Schematic representation of an Euler beam element and its sign conventions.*

The parameters for both components, as used in Equations (A.1a) and (A.1b), are given in Tables A.2 and A.3. Here, Table A.2 gives parameters for the benchmark beam used in Chapter 2,

Chapter 3, and Section 4.2.2, and Table A.3 for the benchmark used in Section 4.3.2 and Chapter 5 (in which component 1 is made somewhat weaker). Here, "component length" represents the total length of the component. The length of a single element (l) is thus obtained by dividing the length given in these tables by the number of elements in the component (10). Furthermore, the length of the beams in Section 3.3 do not correspond to the values in these tables, but rather to the length as indicated in Figures 3.5 and 3.6.

Table A.2: *Used parameters for the standard two-component cantilever beam in Chapter 2, Chapter 3, and Section 4.2.2.*

Parameter	Unit	Component 1	Component 2
Density	kg/m^3	7.850×10^{3}	7.850×10^{3}
Cross-sectional area	m^2	1×10^{-2}	1×10^{-2}
Area moment of intertia	m^4	$1/12\times10^{-4}$	$1/12\times10^{-4}$
Young's modulus	N/m^2	2.1×10^{11}	2.1×10^{11}
Component length	m	5	5

Table A.3: *Used parameters for the standard two-component cantilever beam in Section 4.3.2 and Chapter 5 (where component 1 is less stiff with respect to the definition in Table A.2).*

Parameter	Unit	Component 1	Component 2
Density	kg/m^3	7.850×10^{3}	7.850×10^{3}
Cross-sectional area	m^2	1×10^{-2}	1×10^{-2}
Area moment of intertia	m^4	$1/12\times10^{-4}$	$1/12\times10^{-4}$
Young's modulus	N/m^2	2.1×10^{9}	2.1×10^{11}
Component length	m	5	5

Finally, Table A.4 shows the numbers used to indicate specific nodes and DOFs, as used throughout this thesis. For conciseness, this table is limited to the most important nodes, being the boundary nodes (since only transfer functions between boundary nodes are evaluated in this thesis because these represent the POIs). This numbering is based on a few rules; counting starts from the left-most node of a component/assembly (including the constrained node). When counting degrees of freedom, each displacement DOF of a node is counted first, followed by the rotation DOF, and then the displacement DOF of the next node and so forth. Force/displacements DOFs are thus always indicated by odd numbers, whereas moments and rotation are indicated by even numbers. In an assembly, the shared interface nodes of both components are only counted once, since they are only present once in the assembly.

Table A.4: *Clarification of the numbering of boundary nodes and DOFs.*

Description	Type	Node # Comp 1	Comp 2	DOF # Comp 1	Comp 2	Node # Assy	DOF # Assy
Translation (1.5 m)	Retained	4	-	7	-	4	7
Rotation (1.5 m)	Retained	4	-	8	-	4	8
Translation (5 m)	Interface	11	1	21	1	11	21
Rotation (5 m)	Interface	11	1	22	2	11	22
Translation (6.5 m)	Retained	-	4	-	7	14	27
Rotation (6.5 m)	Retained	-	4	-	8	14	28

A.2 Component eigenfrequencies and component/assembly error measures

In Table A.5, the eigenfrequency of each mode is tabulated for both components. Also, the error measure of the reduced assembly if a single eigenmode is truncated from the component reduction bases is tabulated as well.

Table A.5: *Frequencies of all uncoupled component modes and measures for assembly error when only one component mode is omitted from the reduction bases, listed for every non-rigid eigenmode of both components of the demonstrator beam.*

Component 1			Component 2		
Mode	Frequency [Hz]	$\chi^{(assy)}_{\boldsymbol{\phi}^{(1)}_k}$ [-]	Mode	Frequency [Hz]	$\chi^{(assy)}_{\boldsymbol{\phi}^{(2)}_k}$ [-]
1	0.334	61.793	1	21.267	7.518
2	2.095	23.839	2	58.636	3.219
3	5.866	9.159	3	115.028	0.728
4	11.503	8.993	4	190.428	0.363
5	19.045	12.312	5	285.225	0.169
6	28.532	3.260	6	400.022	0.119
7	40.031	3.619	7	535.536	0.105
8	53.631	8.437	8	691.699	0.066
9	69.344	2.995	9	859.280	0.042
10	86.205	0.923	10	1141.111	0.053
11	114.735	3.788	11	1372.920	0.050
12	138.614	2.062	12	1657.922	0.032
13	168.032	0.785	13	1992.830	0.039
14	202.804	1.804	14	2384.978	0.040
15	243.699	1.872	15	2843.043	0.025
16	291.466	1.330	16	3370.610	0.027
17	345.925	0.678	17	3949.969	0.033
18	403.850	1.451	18	4499.502	0.017
19	454.780	1.593	19	5686.193	0.080
20	569.152	3.698	20	5696.749	0.079

Table A.6 summarizes error measures for the assembly error if either the traditional or improved

method is used to retain a specific number ($n_{\mathcal{K}}^{(assy)}$) of eigenmodes which are to be used in the HH reduction bases of the components. The tabulated FROIs and the POIs (as defined by Figure 5.3) are used to calculate the error measures. Which specific modes are kept in both methods is tabulated in Tables 5.1 and 5.3, where FROI $= 0 - 32$ and FROI $= 0 - 80$, respectively.

Table A.6: *Error measures obtained for the error when the assembly is reduced by using $n_{\mathcal{K}}^{(assy)}$ non-rigid component modes for HH reduction bases, where the mode selection is performed by the traditional and improved method. Here, the error measure is determined for the FROI indicated in the first column and for the POIs depicted in Figure 5.3.*

FROI [Hz]	$n_{\mathcal{K}}^{(assy)}$	Error measure [-] Traditional	Improved
$0 - 32$	3	7.3343×10^{1}	5.7036×10^{0}
	8	1.0345×10^{-1}	7.0222×10^{-1}
	11	7.0686×10^{-3}	3.0286×10^{-3}
	13	3.0401×10^{-3}	1.5924×10^{-3}
$0 - 80$	3	7.4946×10^{1}	5.4331×10^{1}
	8	1.3115×10^{1}	4.8496×10^{0}
	11	3.1290×10^{-1}	2.4879×10^{0}
	13	3.6575×10^{-2}	1.0011×10^{-1}

Appendix B

Derivations and proofs

B.1 Derivation of small gain condition

As was discussed in Section 3.1.1, a feedback loop is present in the system depicted in Figure 3.1. Below, the derivation of the small gain condition based on this feedback loop and presented in Equation (3.1) will be given.

According to Skogestad and Postlethwaite [28], a closed-loop system is stable if, for a given stable loop transfer function matrix $\boldsymbol{H}(s)$,

$$\|\boldsymbol{H}(\omega j)\| < 1 \qquad \forall \omega, \tag{B.1}$$

where $\|\cdot\|$ denotes any matrix norm satisfying $\|\boldsymbol{H}_1\boldsymbol{H}_2\| \leq \|\boldsymbol{H}_1\|\|\boldsymbol{H}_2\|$ (submultiplicative property). Translation of this condition to the context of the feedback system introduced in Section 2.2.4, gives

$$\|\boldsymbol{H}_{wv}^{(1)}(\omega j)\boldsymbol{H}_{vw}^{(2)}(\omega j)\| < 1 \qquad \forall \omega. \tag{B.2}$$

Since the induced 2-norm satisfies the submultiplicative property (as mentioned in Appendix C.1.2), the following inequality is satisfied:

$$\|\boldsymbol{H}_{wv}^{(1)}(\omega j)\|_2\|\boldsymbol{H}_{vw}^{(2)}(\omega j)\|_2 < 1 \qquad \forall \omega. \tag{B.3}$$

As explained in [7], the induced 2-norm of a matrix equals the largest singular value (σ_{max}) of that matrix. Therefore, Equation (B.3) is equivalent to

$$\sigma_{max}\left(\boldsymbol{H}_{wv}^{(1)}(\omega j)\right) \cdot \sigma_{max}\left(\boldsymbol{H}_{vw}^{(2)}(\omega j)\right) < 1 \qquad \forall \omega. \tag{B.4}$$

Now, it is opted to use the maximal values of the highest singular value (evaluated over the frequency). Since this is done for both components individually, the value found before the inequality sign can never exceed the value in Equation (B.4) at any frequency.

$$\sup_{\omega} \sigma_{max}\left(\boldsymbol{H}_{wv}^{(1)}(\omega j)\right) \cdot \sup_{\omega} \sigma_{max}\left(\boldsymbol{H}_{vw}^{(2)}(\omega j)\right) < 1 \tag{B.5}$$

Since

$$\|\boldsymbol{H}(s)\|_\infty = \sup_{\omega} \sigma_{max}\left(\boldsymbol{H}(\omega j)\right), \tag{B.6}$$

Equation (B.5) is written as

$$\left\|\boldsymbol{H}_{wv}^{(1)}(\omega j)\right\|_\infty \cdot \left\|\boldsymbol{H}_{vw}^{(2)}(\omega j)\right\|_\infty < 1, \tag{B.7}$$

which, using a more compact notation, is written as

$$\gamma_{wv}^{(1)}\gamma_{vw}^{(2)} < 1, \tag{B.8}$$

which is recognized as the as the small gain condition as presented in Chapter 3.

B.2 Derivation of upper bound on assembly error

In this section, the derivation of Equation (3.3) as given in Section 3.1.2 is given. For this, the theory provided by Besselink [2, 1] is used as a guideline. In this derivation, for clarity sake, the most important equations are highlighted by a box, non-highlighted equations typically give intermediate steps in the derivation.

First, Figure B.1 shows a variant of Figure 3.1, but uses a function notation instead of explicit transfer function notation. In this figure, all outputs of a component are denoted as a function $G^{(c)}$ of the input(s) of that component, where the subscript of $G^{(c)}$ denotes the output.

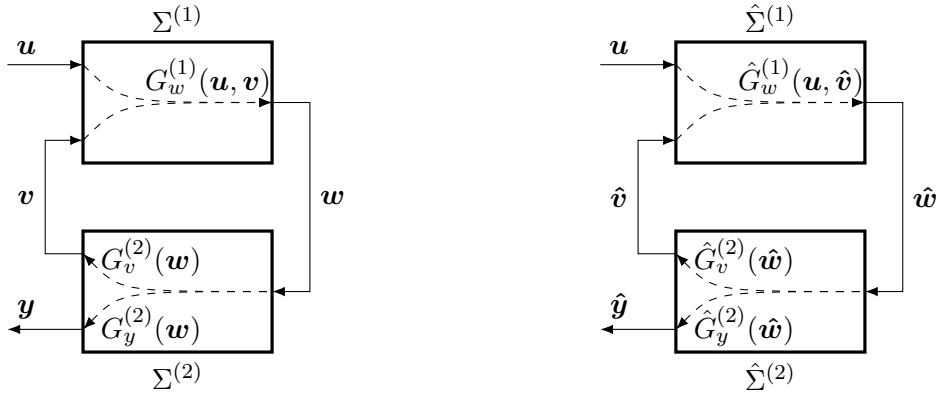

(a) *Subsystems 1 & 2 unreduced.* **(b)** *Subsystems 1 & 2 reduced.*

Figure B.1: *System representations of two coupled subsystems ($\Sigma^{(1)}$ and $\Sigma^{(2)}$) in a feedback form with function notation and non-colocated the input and output.*

Using the different functions introduced in this figure, the outputs of both unreduced subsystems are given by

$$\boldsymbol{y} = G_y^{(2)}(\boldsymbol{w}) \quad = \boldsymbol{H}_{yw}^{(2)}\boldsymbol{w}, \tag{B.9a}$$
$$\boldsymbol{v} = G_v^{(2)}(\boldsymbol{w}) \quad = \boldsymbol{H}_{vw}^{(2)}\boldsymbol{w}, \tag{B.9b}$$
$$\boldsymbol{w} = G_w^{(1)}(\boldsymbol{u},\boldsymbol{v}) = \boldsymbol{H}_{wu}^{(1)}\boldsymbol{u} + \boldsymbol{H}_{wv}^{(1)}\boldsymbol{v}, \tag{B.9c}$$

and the outputs of the reduced subsystems by

$$\hat{\boldsymbol{y}} = \hat{G}_y^{(2)}(\hat{\boldsymbol{w}}) \quad = \hat{\boldsymbol{H}}_{yw}^{(2)}\hat{\boldsymbol{w}}, \tag{B.10a}$$
$$\hat{\boldsymbol{v}} = \hat{G}_v^{(2)}(\hat{\boldsymbol{w}}) \quad = \hat{\boldsymbol{H}}_{vw}^{(2)}\hat{\boldsymbol{w}}, \tag{B.10b}$$
$$\hat{\boldsymbol{w}} = \hat{G}_w^{(1)}(\boldsymbol{u},\hat{\boldsymbol{v}}) = \hat{\boldsymbol{H}}_{wu}^{(1)}\boldsymbol{u} + \hat{\boldsymbol{H}}_{wv}^{(1)}\hat{\boldsymbol{v}}. \tag{B.10c}$$

These equation are used throughout this derivation for $\bar{\varepsilon}_{yu}^{(assy)}$.

Since the goal is to find a bound on the $\mathcal{L}_2$-norm of the error of the output for a given $\mathcal{L}_2$-norm of the input (Equation (3.2)), an expression for this error is defined as the difference of $\boldsymbol{y}$ and $\hat{\boldsymbol{y}}$:

$$\begin{aligned}\boldsymbol{\delta y} &= \boldsymbol{y} - \hat{\boldsymbol{y}} \\ &= G_y^{(2)}(\boldsymbol{w}) - \hat{G}_y^{(2)}(\hat{\boldsymbol{w}}) \\ &= G_y^{(2)}(\boldsymbol{w}) - \hat{G}_y^{(2)}(\boldsymbol{w}) + \hat{G}_y^{(2)}(\boldsymbol{w}) - \hat{G}_y^{(2)}(\hat{\boldsymbol{w}}).\end{aligned} \tag{B.11}$$

Here, for the second line, Equations (B.9a) and (B.10a) were used. To arrive at the last line, a mathematical trick (which is explained in more detail in Appendix C.2.3) is used which both adds and subtracts $\hat{G}_y^{(2)}(\boldsymbol{w})$. This term represents the output $\boldsymbol{y}$ when the unreduced signal $\boldsymbol{w}$ is used as an input for the reduced (second sub-)system.

Since Equation (3.2) uses $\mathcal{L}_2$-norms on the reduction error, the $\mathcal{L}_2$-norm of both sides of Equation (B.11) is taken, giving

$$\|\boldsymbol{\delta y}\|_2 = \|G_y^{(2)}(\boldsymbol{w}) - \hat{G}_y^{(2)}(\boldsymbol{w}) + \hat{G}_y^{(2)}(\boldsymbol{w}) - \hat{G}_y^{(2)}(\hat{\boldsymbol{w}})\|_2. \tag{B.12}$$

Using the triangle inequality, defined in Appendix C.2.1, this can be rewritten to

$$\|\boldsymbol{\delta y}\|_2 \leq \|G_y^{(2)}(\boldsymbol{w}) - \hat{G}_y^{(2)}(\boldsymbol{w})\|_2 + \|\hat{G}_y^{(2)}(\boldsymbol{w}) - \hat{G}_y^{(2)}(\hat{\boldsymbol{w}})\|_2. \tag{B.13}$$

Here, it can be used that

$$G_y^{(2)}(\boldsymbol{w}) - \hat{G}_y^{(2)}(\boldsymbol{w}) = \boldsymbol{H}_{yw}^{(2)}\boldsymbol{w} - \hat{\boldsymbol{H}}_{yw}^{(2)}\boldsymbol{w} \tag{B.14}$$

$$= (\boldsymbol{H}_{yw}^{(2)} - \hat{\boldsymbol{H}}_{yw}^{(2)})\boldsymbol{w}. \tag{B.15}$$

Taking the norms on both sides results in

$$\|G_y^{(2)}(\boldsymbol{w}) - \hat{G}_y^{(2)}(\boldsymbol{w})\|_2 = \|(\boldsymbol{H}_{yw}^{(2)} - \hat{\boldsymbol{H}}_{yw}^{(2)})\boldsymbol{w}\|_2 \leq \|\boldsymbol{H}_{yw}^{(2)} - \hat{\boldsymbol{H}}_{yw}^{(2)}\|_\infty \|\boldsymbol{w}\|_2 = \varepsilon_{yw}^{(2)}\|\boldsymbol{w}\|_2, \tag{B.16}$$

where the $\mathcal{H}_\infty$-norm gives the maximal amplification of the transfer function (matrix) and thus defines a maximal bound on the norm, as is explained in Appendix C.2.2. $\varepsilon_{yw}^{(2)}$ is thus an upper bound on the reduction error of $\hat{\boldsymbol{H}}_{yw}^{(2)}$. Similarly, an expression for $\|\hat{G}_y^{(2)}(\boldsymbol{w}) - \hat{G}_y^{(2)}(\hat{\boldsymbol{w}})\|_2$ is determined:

$$\hat{G}_y^{(2)}(\boldsymbol{w}) - \hat{G}_y^{(2)}(\hat{\boldsymbol{w}}) = \hat{\boldsymbol{H}}_{yw}^{(2)}\boldsymbol{w} - \hat{\boldsymbol{H}}_{yw}^{(2)}\hat{\boldsymbol{w}} \tag{B.17}$$

$$= \hat{\boldsymbol{H}}_{yw}^{(2)}(\boldsymbol{w} - \hat{\boldsymbol{w}}). \tag{B.18}$$

Again, taking the norms and using Appendix C.2.2 results in

$$\|\hat{G}_y^{(2)}(\boldsymbol{w}) - \hat{G}_y^{(2)}(\hat{\boldsymbol{w}})\|_2 = \|\hat{\boldsymbol{H}}_{yw}^{(2)}(\boldsymbol{w} - \hat{\boldsymbol{w}})\|_2 \leq \|\hat{\boldsymbol{H}}_{yw}^{(2)}\|_\infty \|\boldsymbol{w} - \hat{\boldsymbol{w}}\|_2 = \hat{\gamma}_{yw}^{(2)}\|\boldsymbol{\delta w}\|_2. \tag{B.19}$$

Combining the results of Equations (B.11), (B.16), and (B.19), results in

$$\boxed{\|\boldsymbol{\delta y}\|_2 \leq \varepsilon_{yw}^{(2)}\|\boldsymbol{w}\|_2 + \hat{\gamma}_{yw}^{(2)}\|\boldsymbol{\delta w}\|_2,} \tag{B.20}$$

in which the two unknown norms ($\|\boldsymbol{w}\|_2$ and $\|\boldsymbol{\delta w}\|_2$) should be expressed in term of $\|\boldsymbol{u}\|_2$ in order to conform to the form of Equation (3.2). Starting with $\|\boldsymbol{w}\|_2$, the expression for the signal $\boldsymbol{w}$ is repeated:

$$\boldsymbol{w} = G_w^{(1)}(\boldsymbol{u}, \boldsymbol{v}) = \boldsymbol{H}_{wu}^{(1)}\boldsymbol{u} + \boldsymbol{H}_{wv}^{(1)}\boldsymbol{v}. \tag{B.21}$$

Taking the norms in a similar manner as previously done (using the triangle inequality and $\mathcal{H}_\infty$-norm), results in the following expression for $\|\boldsymbol{w}\|_2$:

$$\boxed{\|\boldsymbol{w}\|_2 \leq \|\boldsymbol{H}_{wu}^{(1)}\|_\infty \|\boldsymbol{u}\|_2 + \|\boldsymbol{H}_{wv}^{(1)}\|_\infty \|\boldsymbol{v}\|_2 = \gamma_{wu}^{(1)}\|\boldsymbol{u}\|_2 + \gamma_{wv}^{(1)}\|\boldsymbol{v}\|_2.} \tag{B.22}$$

Since another unknown (norm of a) variable ($\|\boldsymbol{v}\|_2$) appears, an expression for this variable is determined. Using the definition for $\boldsymbol{v}$, Equation (B.9b) gives

$$\boldsymbol{v} = G_v^{(2)}(\boldsymbol{w}) = \boldsymbol{H}_{vw}^{(2)}\boldsymbol{w}. \tag{B.23}$$

Again, taking the norms on both sides and using Appendix C.2.2, results in

$$\boxed{\|\boldsymbol{v}\|_2 \leq \|\boldsymbol{H}_{vw}^{(2)}\|_\infty \|\boldsymbol{w}\|_2 = \gamma_{vw}^{(2)}\|\boldsymbol{w}\|_2.} \tag{B.24}$$

Recalling (B.22) and substituting (B.24) then results in an expression for $\|\boldsymbol{w}\|_2$ in terms of some bounds and the $\mathcal{L}_2$-norm on $\boldsymbol{u}$:

$$\|\boldsymbol{w}\|_2 \leq \gamma_{wu}^{(1)}\|\boldsymbol{u}\|_2 + \gamma_{wv}^{(1)}\|\boldsymbol{v}\|_2 \leq \gamma_{wu}^{(1)}\|\boldsymbol{u}\|_2 + \gamma_{wv}^{(1)}\gamma_{vw}^{(2)}\|\boldsymbol{w}\|_2. \tag{B.25}$$

Now, looking at the left and right hand side, the terms with $\|\boldsymbol{w}\|_2$ can be collected at the left side of the inequality sign:

$$(1 - \gamma_{wv}^{(1)}\gamma_{vw}^{(2)})\|\boldsymbol{w}\|_2 \leq \gamma_{wu}^{(1)}\|\boldsymbol{u}\|_2 \tag{B.26}$$

And thus

$$\boxed{\|\boldsymbol{w}\|_2 \leq \left(1 - \gamma_{wv}^{(1)}\gamma_{vw}^{(2)}\right)^{-1} \gamma_{wu}^{(1)}\|\boldsymbol{u}\|_2.} \tag{B.27}$$

By having an expression for $\|\boldsymbol{w}\|_2$ in terms of $\|\boldsymbol{u}\|_2$, one important unknown variable in Equation (B.20) is obtained.

An expression for the resulting unknown norm $\|\boldsymbol{\delta w}\|_2$ (in Equation (B.20)) in terms of $\|\boldsymbol{u}\|_2$ is derived in the following. Therefore, first, the definition of $\boldsymbol{\delta w}$ is given, where the mathematical trick explained in Appendix C.2.3 is exploited again:

$$\begin{aligned}
\boldsymbol{\delta w} &= \boldsymbol{w} - \hat{\boldsymbol{w}} && \text{(B.28)}\\
&= G_w^{(1)}(\boldsymbol{u}, \boldsymbol{v}) - \hat{G}_w^{(1)}(\boldsymbol{u}, \hat{\boldsymbol{v}}) && \text{(B.29)}\\
&= G_w^{(1)}(\boldsymbol{u}, \boldsymbol{v}) - \hat{G}_w^{(1)}(\boldsymbol{u}, \boldsymbol{v}) + \hat{G}_w^{(1)}(\boldsymbol{u}, \boldsymbol{v}) - \hat{G}_w^{(1)}(\boldsymbol{u}, \hat{\boldsymbol{v}}). && \text{(B.30)}
\end{aligned}$$

By taking the norms and using the triangle inequality (like in the derivation of Equation (B.20)), this results in

$$\|\boldsymbol{\delta w}\|_2 \leq \|G_w^{(1)}(\boldsymbol{u}, \boldsymbol{v}) - \hat{G}_w^{(1)}(\boldsymbol{u}, \boldsymbol{v})\|_2 + \|\hat{G}_w^{(1)}(\boldsymbol{u}, \boldsymbol{v}) - \hat{G}_w^{(1)}(\boldsymbol{u}, \hat{\boldsymbol{v}})\|_2. \tag{B.31}$$

First, $\|G_w^{(1)}(\boldsymbol{u}, \boldsymbol{v}) - \hat{G}_w^{(1)}(\boldsymbol{u}, \boldsymbol{v})\|_2$ can be written as

$$\begin{aligned}
\|G_w^{(1)}(\boldsymbol{u}, \boldsymbol{v}) - \hat{G}_w^{(1)}(\boldsymbol{u}, \boldsymbol{v})\|_2 &= \|\boldsymbol{H}_{wu}^{(1)}\boldsymbol{u} + \boldsymbol{H}_{wv}^{(1)}\boldsymbol{v} - \hat{\boldsymbol{H}}_{wu}^{(1)}\boldsymbol{u} - \hat{\boldsymbol{H}}_{wv}^{(1)}\boldsymbol{v}\|_2 && \text{(B.32)}\\
&= (\|\boldsymbol{H}_{wu}^{(1)} - \hat{\boldsymbol{H}}_{wu}^{(1)})\boldsymbol{u} + (\boldsymbol{H}_{wv}^{(1)} - \hat{\boldsymbol{H}}_{wv}^{(1)})\boldsymbol{v}\|_2. && \text{(B.33)}
\end{aligned}$$

Then, according to the triangle inequality and bound by the $\mathcal{H}_\infty$-norm:

$$\begin{aligned}
\|G_w^{(1)}(\boldsymbol{u}, \boldsymbol{v}) - \hat{G}_w^{(1)}(\boldsymbol{u}, \boldsymbol{v})\|_2 &\leq \|(\boldsymbol{H}_{wu}^{(1)} - \hat{\boldsymbol{H}}_{wu}^{(1)})\boldsymbol{u}\|_2 + \|(\boldsymbol{H}_{wv}^{(1)} - \hat{\boldsymbol{H}}_{wv}^{(1)})\boldsymbol{v}\|_2 && \text{(B.34)}\\
&\leq \|\boldsymbol{H}_{wu}^{(1)} - \hat{\boldsymbol{H}}_{wu}^{(1)}\|_\infty \|\boldsymbol{u}\|_2 + \|\boldsymbol{H}_{wv}^{(1)} - \hat{\boldsymbol{H}}_{wv}^{(1)}\|_\infty \|\boldsymbol{v}\|_2 && \text{(B.35)}\\
\Rightarrow \|G_w^{(1)}(\boldsymbol{u}, \boldsymbol{v}) - \hat{G}_w^{(1)}(\boldsymbol{u}, \boldsymbol{v})\|_2 &\leq \varepsilon_{wu}^{(1)}\|\boldsymbol{u}\|_2 + \varepsilon_{wv}^{(1)}\|\boldsymbol{v}\|_2. && \text{(B.36)}
\end{aligned}$$

Using similar steps, $\|\hat{G}_w^{(1)}(\boldsymbol{u}, \boldsymbol{v}) - \hat{G}_w^{(1)}(\boldsymbol{u}, \hat{\boldsymbol{v}})\|_2$ is written as

$$\begin{aligned}
\|\hat{G}_w^{(1)}(\boldsymbol{u}, \boldsymbol{v}) - \hat{G}_w^{(1)}(\boldsymbol{u}, \hat{\boldsymbol{v}})\|_2 &= \|\hat{\boldsymbol{H}}_{wu}^{(1)}\boldsymbol{u} + \hat{\boldsymbol{H}}_{wv}^{(1)}\boldsymbol{v} - \hat{\boldsymbol{H}}_{wu}^{(1)}\boldsymbol{u} - \hat{\boldsymbol{H}}_{wv}^{(1)}\hat{\boldsymbol{v}}\|_2 && \text{(B.37)}\\
&= \|(\hat{\boldsymbol{H}}_{wu}^{(1)} - \hat{\boldsymbol{H}}_{wu}^{(1)})\boldsymbol{u} + \hat{\boldsymbol{H}}_{wv}^{(1)}(\boldsymbol{v} - \hat{\boldsymbol{v}})\|_2, && \text{(B.38)}
\end{aligned}$$

which now gives

$$\|\hat{G}_w^{(1)}(\boldsymbol{u},\boldsymbol{v}) - \hat{G}_w^{(1)}(\boldsymbol{u},\hat{\boldsymbol{v}})\|_2 \leq \|(\hat{\boldsymbol{H}}_{wu}^{(1)} - \hat{\boldsymbol{H}}_{wu}^{(1)})\boldsymbol{u}\|_2 + \|\hat{\boldsymbol{H}}_{wv}^{(1)}(\boldsymbol{v}-\hat{\boldsymbol{v}})\|_2 \tag{B.39}$$

$$\leq 0\|\boldsymbol{u}\|_2 + \|\hat{\boldsymbol{H}}_{wv}^{(1)}\|_\infty \|\boldsymbol{v}-\hat{\boldsymbol{v}}\|_2 = \hat{\gamma}_{wv}^{(1)}\|\boldsymbol{\delta v}\|_2. \tag{B.40}$$

Substituting Equations (B.36) and (B.40) in Equation (B.31) then results in:

$$\boxed{\|\boldsymbol{\delta w}\|_2 \leq \varepsilon_{wu}^{(1)}\|\boldsymbol{u}\|_2 + \varepsilon_{wv}^{(1)}\|\boldsymbol{v}\|_2 + \hat{\gamma}_{wv}^{(1)}\|\boldsymbol{\delta v}\|_2.} \tag{B.41}$$

For this equation, $\|\boldsymbol{v}\|_2$ is given in terms of $\|\boldsymbol{u}\|_2$ by combining Equations (B.24) and (B.27):

$$\boxed{\|\boldsymbol{v}\|_2 = \gamma_{vw}^{(2)}\left(1-\gamma_{wv}^{(1)}\gamma_{vw}^{(2)}\right)^{-1}\gamma_{wu}^{(1)}\|\boldsymbol{u}\|_2.} \tag{B.42}$$

Therefore, Equation (B.41) can largely be written in terms of $\|\boldsymbol{u}\|_2$, except for the term with $\|\boldsymbol{\delta v}\|_2$. An expression for this variable in terms of $\|\boldsymbol{u}\|_2$ is therefore determined in the following, starting with the definition of $\boldsymbol{\delta v}$:

$$\boldsymbol{\delta v} = \boldsymbol{v} - \hat{\boldsymbol{v}} \tag{B.43}$$

$$= G_v^{(2)}(\boldsymbol{w}) - \hat{G}_v^{(2)}(\hat{\boldsymbol{w}}) \tag{B.44}$$

$$= G_v^{(2)}(\boldsymbol{w}) - \hat{G}_v^{(2)}(\boldsymbol{w}) + \hat{G}_v^{(2)}(\boldsymbol{w}) - \hat{G}_v^{(2)}(\hat{\boldsymbol{w}}). \tag{B.45}$$

Once more, taking the norms on both sides and using the triangle inequality:

$$\|\boldsymbol{\delta v}\|_2 \leq \|G_v^{(2)}(\boldsymbol{w}) - \hat{G}_v^{(2)}(\boldsymbol{w})\|_2 + \|\hat{G}_v^{(2)}(\boldsymbol{w}) - \hat{G}_v^{(2)}(\hat{\boldsymbol{w}})\|_2. \tag{B.46}$$

Finding an expression for $\|G_v^{(2)}(\boldsymbol{w}) - \hat{G}_v^{(2)}(\boldsymbol{w})\|_2$ gives

$$\|G_v^{(2)}(\boldsymbol{w}) - \hat{G}_v^{(2)}(\boldsymbol{w})\|_2 = \|(\boldsymbol{H}_{vw}^{(2)} - \hat{\boldsymbol{H}}_{vw}^{(2)})\boldsymbol{w}\|_2 \tag{B.47}$$

$$\|G_v^{(2)}(\boldsymbol{w}) - \hat{G}_v^{(2)}(\boldsymbol{w})\|_2 \leq \|\boldsymbol{H}_{vw}^{(2)} - \hat{\boldsymbol{H}}_{vw}^{(2)}\|_\infty \|\boldsymbol{w}\|_2 = \varepsilon_{vw}^{(2)}\|\boldsymbol{w}\|_2. \tag{B.48}$$

Similarly,

$$\|\hat{G}_v^{(2)}(\boldsymbol{w}) - \hat{G}_v^{(2)}(\hat{\boldsymbol{w}})\|_2 = \|\hat{\boldsymbol{H}}_{vw}^{(2)}(\boldsymbol{w}-\hat{\boldsymbol{w}})\|_2 \tag{B.49}$$

$$\|\hat{G}_v^{(2)}(\boldsymbol{w}) - \hat{G}_v^{(2)}(\hat{\boldsymbol{w}})\|_2 \leq \|\hat{\boldsymbol{H}}_{vw}^{(2)}\|_\infty \|\boldsymbol{w}-\hat{\boldsymbol{w}}\|_2 = \hat{\gamma}_{vw}^{(2)}\|\boldsymbol{\delta w}\|_2. \tag{B.50}$$

Note here the similarity to the derivations of Equations (B.20) and (B.41). Substituting Equations (B.48) and (B.50) in Equation (B.46), results in

$$\|\boldsymbol{\delta v}\|_2 \leq \varepsilon_{vw}^{(2)}\|\boldsymbol{w}\|_2 + \hat{\gamma}_{vw}^{(2)}\|\boldsymbol{\delta w}\|_2, \tag{B.51}$$

where $\|\boldsymbol{w}\|_2$ can be substituted by Equation (B.27). Subsequently substituting this result in (B.51), gives $\|\boldsymbol{\delta v}\|_2$ as a function of $\|\boldsymbol{u}\|_2$ and $\|\boldsymbol{\delta w}\|_2$:

$$\boxed{\|\boldsymbol{\delta v}\|_2 \leq \varepsilon_{vw}^{(2)}\left(1-\gamma_{wv}^{(1)}\gamma_{vw}^{(2)}\right)^{-1}\gamma_{wu}^{(1)}\|\boldsymbol{u}\|_2 + \hat{\gamma}_{vw}^{(2)}\|\boldsymbol{\delta w}\|_2.} \tag{B.52}$$

Going back to the expression for $\|\boldsymbol{\delta w}\|_2$ in Equation (B.41), and filling in Equations (B.42) and (B.52) for $\|\boldsymbol{v}\|_2$ and $\|\boldsymbol{\delta v}\|_2$, respectively, gives

$$\begin{aligned}\|\boldsymbol{\delta w}\|_2 \leq{}& \varepsilon_{wu}^{(1)}\|\boldsymbol{u}\|_2 + \varepsilon_{wv}^{(1)}\gamma_{vw}^{(2)}\left(1-\gamma_{wv}^{(1)}\gamma_{vw}^{(2)}\right)^{-1}\gamma_{wu}^{(1)}\|\boldsymbol{u}\|_2 \ldots \\ &+ \hat{\gamma}_{wv}^{(1)}\left(\varepsilon_{vw}^{(2)}\left(1-\gamma_{wv}^{(1)}\gamma_{vw}^{(2)}\right)^{-1}\gamma_{wu}^{(1)}\|\boldsymbol{u}\|_2 + \hat{\gamma}_{vw}^{(2)}\|\boldsymbol{\delta w}\|_2\right)\end{aligned} \tag{B.53}$$

$$\begin{aligned}\Rightarrow \left(1-\hat{\gamma}_{wv}^{(1)}\hat{\gamma}_{vw}^{(2)}\right)\|\boldsymbol{\delta w}\|_2 \leq{}& \left(\varepsilon_{wu}^{(1)} + \varepsilon_{wv}^{(1)}\gamma_{vw}^{(2)}\left(1-\gamma_{wv}^{(1)}\gamma_{vw}^{(2)}\right)^{-1}\gamma_{wu}^{(1)} \ldots \right. \\ &\left. + \hat{\gamma}_{wv}^{(1)}\varepsilon_{vw}^{(2)}\left(1-\gamma_{wv}^{(1)}\gamma_{vw}^{(2)}\right)^{-1}\gamma_{wu}^{(1)}\right)\|\boldsymbol{u}\|_2.\end{aligned} \tag{B.54}$$

Since here the only norms are $\|\boldsymbol{\delta w}\|_2$ and $\|\boldsymbol{u}\|_2$, the former can be expressed in terms of the latter:

$$\boxed{\begin{aligned}\|\boldsymbol{\delta w}\|_2 \leq \left(1-\hat{\gamma}_{wv}^{(1)}\hat{\gamma}_{vw}^{(2)}\right)^{-1}\Bigg(&\varepsilon_{wu}^{(1)}+\varepsilon_{wv}^{(1)}\gamma_{vw}^{(2)}\left(1-\gamma_{wv}^{(1)}\gamma_{vw}^{(2)}\right)^{-1}\gamma_{wu}^{(1)}\dots\\&+\hat{\gamma}_{wv}^{(1)}\varepsilon_{vw}^{(2)}\left(1-\gamma_{wv}^{(1)}\gamma_{vw}^{(2)}\right)^{-1}\gamma_{wu}^{(1)}\Bigg)\|\boldsymbol{u}\|_2.\end{aligned}} \tag{B.55}$$

By this, both unknown variables in Equation (B.20) have been defined (see Equations (B.27) and (B.55)). Substituting these in Equation (B.20), results in the required expression for the $\mathcal{L}_2$-norm of $\boldsymbol{\delta y}$ in terms of $\|\boldsymbol{u}\|_2$:

$$\begin{aligned}\|\boldsymbol{\delta y}\|_2 \leq\ &\varepsilon_{yw}^{(2)}\left(1-\gamma_{wv}^{(1)}\gamma_{vw}^{(2)}\right)^{-1}\gamma_{wu}^{(1)}\|\boldsymbol{u}\|_2\dots\\&+\hat{\gamma}_{yw}^{(2)}\left(1-\hat{\gamma}_{wv}^{(1)}\hat{\gamma}_{vw}^{(2)}\right)^{-1}\Bigg(\varepsilon_{wu}^{(1)}+\varepsilon_{wv}^{(1)}\gamma_{vw}^{(2)}\left(1-\gamma_{wv}^{(1)}\gamma_{vw}^{(2)}\right)^{-1}\gamma_{wu}^{(1)}\dots\\&+\hat{\gamma}_{wv}^{(1)}\varepsilon_{vw}^{(2)}\left(1-\gamma_{wv}^{(1)}\gamma_{vw}^{(2)}\right)^{-1}\gamma_{wu}^{(1)}\Bigg)\|\boldsymbol{u}\|_2.\end{aligned} \tag{B.56}$$

Rewriting then results in

$$\boxed{\begin{aligned}\|\boldsymbol{\delta y}\|_2 \leq \Bigg(&\varepsilon_{yw}^{(2)}\left(1-\gamma_{wv}^{(1)}\gamma_{vw}^{(2)}\right)^{-1}\gamma_{wu}^{(1)}+\hat{\gamma}_{yw}^{(2)}\left(1-\hat{\gamma}_{wv}^{(1)}\hat{\gamma}_{vw}^{(2)}\right)^{-1}\dots\\&\cdot\left(\varepsilon_{wu}^{(1)}+\varepsilon_{wv}^{(1)}\gamma_{vw}^{(2)}\left(1-\gamma_{wv}^{(1)}\gamma_{vw}^{(2)}\right)^{-1}\gamma_{wu}^{(1)}+\hat{\gamma}_{wv}^{(1)}\varepsilon_{vw}^{(2)}\left(1-\gamma_{wv}^{(1)}\gamma_{vw}^{(2)}\right)^{-1}\gamma_{wu}^{(1)}\right)\Bigg)\|\boldsymbol{u}\|_2.\end{aligned}} \tag{B.57}$$

Since the bound $\bar{\varepsilon}_{yu}^{(assy)}$ is defined in

$$\|\boldsymbol{\delta y}\|_2 \leq \bar{\varepsilon}_{yu}^{(assy)}\|\boldsymbol{u}\|_2, \tag{B.58}$$

the upper bound of the error gain $\bar{\varepsilon}_{yu}^{(assy)}$ is given by Equation (B.59).

$$\boxed{\begin{aligned}\bar{\varepsilon}_{yu}^{(assy)} = \varepsilon_{yw}^{(2)}&\left(1-\gamma_{wv}^{(1)}\gamma_{vw}^{(2)}\right)^{-1}\gamma_{wu}^{(1)}+\hat{\gamma}_{yw}^{(2)}\left(1-\hat{\gamma}_{wv}^{(1)}\hat{\gamma}_{vw}^{(2)}\right)^{-1}\dots\\&\cdot\left(\varepsilon_{wu}^{(1)}+\varepsilon_{wv}^{(1)}\gamma_{vw}^{(2)}\left(1-\gamma_{wv}^{(1)}\gamma_{vw}^{(2)}\right)^{-1}\gamma_{wu}^{(1)}+\hat{\gamma}_{wv}^{(1)}\varepsilon_{vw}^{(2)}\left(1-\gamma_{wv}^{(1)}\gamma_{vw}^{(2)}\right)^{-1}\gamma_{wu}^{(1)}\right).\end{aligned}} \tag{B.59}$$

This final equation thus gives the error gain bound as a function of different contributions. Here, four different error bounds, $\varepsilon_{yw}^{(2)}$, $\varepsilon_{wu}^{(1)}$, $\varepsilon_{wv}^{(1)}$, and $\varepsilon_{vw}^{(2)}$ are recognized. The terms with which these variables are multiplied, can be regarded as bounds on the control, process, and complementary sensitivities. This again relates to the feedback character of these equations.

An interesting observation that can be made in Equation (B.59) (but also holds for all equations used in the derivation given above), is that, given any concatenation of γ's (e.g., $\gamma_{ij}\gamma_{kl}\gamma_{mn} = \alpha_{in}$), for the indexes it should hold that $j = k$ and $l = m$. Furthermore, the first index in the concatenation refers to the left index of the result (the output) and the last index in the concatenation refers to the variable to the right (the input).

Finally, as can be seen in Equation (B.59), $1-\gamma_{wv}^{(1)}\gamma_{vw}^{(2)}$ and/or $1-\hat{\gamma}_{wv}^{(1)}\hat{\gamma}_{vw}^{(2)}$ could become (approximately) one. Therefore, two conditions are needed which need to hold in order to be able to determine a valid finite error bound using Equation (B.59):

$$\gamma_{wv}^{(1)}\gamma_{vw}^{(2)} \neq 1 \tag{B.60}$$

and

$$\hat{\gamma}_{wv}^{(1)}\hat{\gamma}_{vw}^{(2)} \neq 1. \tag{B.61}$$

This condition is related to the small gain condition discussed in Section 3.1.1. Note here that the small gain condition also does not allow this product to be larger than 1, since otherwise closed-loop stability of the loop can not be guaranteed and errors could potentially explode within the loop.

B.3 Derivation of feedback representation

In this appendix, Equations (2.30a), (2.30b), and (2.30c), as given in the main text, are derived. For this derivation, the compatibility and force equilibrium conditions as discussed in Section 2.2.1 and given for the specific demonstrator by Equations (B.62) and (B.63) are used.

$$\boldsymbol{U}_f^{(1)} = \boldsymbol{U}_f^{(2)} \tag{B.62}$$

$$\boldsymbol{F}_f^{(1)} = -\boldsymbol{F}_f^{(2)} \tag{B.63}$$

Now, using the schematic two-component beam in Figure 2.3, the displacements $\boldsymbol{U}_f^{(1)}$, $\boldsymbol{U}_f^{(2)}$, and $\boldsymbol{U}_{out}$ are written in terms of the forces acting on the components and the transfer functions within each component:

$$\boldsymbol{U}_f^{(1)} = \boldsymbol{H}_{fF}^{(1)}\boldsymbol{F}_{in} + \boldsymbol{H}_{ff}^{(1)}\boldsymbol{F}_f^{(1)} \tag{B.64}$$

$$\boldsymbol{U}_f^{(2)} = \boldsymbol{H}_{ff}^{(2)}\boldsymbol{F}_f^{(2)} \tag{B.65}$$

$$\boldsymbol{U}_{out} = \boldsymbol{H}_{Uf}^{(2)}\boldsymbol{F}_f^{(2)}. \tag{B.66}$$

Rearranging (B.65) to obtain an expression of $\boldsymbol{F}_f^{(2)}$, and substituting this in the equation for $\boldsymbol{U}_{out}$, gives an equation which satisfies requirement (2.29c):

$$\boldsymbol{U}_{out} = \boldsymbol{H}_{Uf}^{(2)}{\boldsymbol{H}_{ff}^{(2)}}^{-1}\boldsymbol{U}_f^{(2)}. \tag{B.67}$$

Simply using the compatibility requirement in Equation (B.64) gives

$$\boldsymbol{U}_f^{(2)} = \boldsymbol{H}_{fF}^{(1)}\boldsymbol{F}_{in} + \boldsymbol{H}_{ff}^{(1)}\boldsymbol{F}_f^{(1)}, \tag{B.68}$$

which satisfies requirement (2.29a). Finally, in order to meet requirement (2.29b), the equilibrium condition is used after Equation (B.65) has been rearranged, resulting in

$$\boldsymbol{F}_f^{(1)} = -{\boldsymbol{H}_{ff}^{(2)}}^{-1}\boldsymbol{U}_f^{(2)}. \tag{B.69}$$

B.4 Spectral decomposition of HH-reduced receptance

In this appendix, the spectral decomposition of a reduced component receptance matrix (obtained by using Hintz-Herting) as shown in Equation (4.9) is derived. This derivation is partly based on the derivation for the receptance of a modal truncated system as given in de Kraker [20].

Starting with the expression for the unreduced dynamic stiffness (which equals the inverse of the receptance):

$$\boldsymbol{Z}(\omega j) = \boldsymbol{Y}^{-1}(\omega j) = \boldsymbol{K} - \omega^2\boldsymbol{M}, \tag{B.70}$$

and pre-multiplying and post-multiplying with the reduction matrix $\boldsymbol{T}_{HH,o}$ gives the reduced dynamic stiffness

$$\hat{\boldsymbol{Y}}^{-1}(\omega j) = \boldsymbol{T}_{HH,o}^T \boldsymbol{Y}^{-1}(\omega j) \boldsymbol{T}_{HH,o} = \boldsymbol{T}_{HH,o}^T \left(\boldsymbol{K} - \omega^2 \boldsymbol{M}\right) \boldsymbol{T}_{HH,o} \tag{B.71}$$

$$= \boldsymbol{T}_{HH,o}^T \boldsymbol{K} \boldsymbol{T}_{HH,o} - \omega^2 \boldsymbol{T}_{HH,o}^T \boldsymbol{M} \boldsymbol{T}_{HH,o} \tag{B.72}$$

$$= \hat{\boldsymbol{K}}_{HH,o} - \omega^2 \hat{\boldsymbol{M}}_{HH,o}. \tag{B.73}$$

Now, using the fact that since

$$\boldsymbol{T}_{HH,o} = \begin{bmatrix} \boldsymbol{\Phi}_{\mathcal{K}} & \boldsymbol{X}_o \end{bmatrix}, \tag{B.74}$$

and $\boldsymbol{X}_o$ is orthogonal to $\boldsymbol{\Phi}_{\mathcal{K}}$ (which itself is mass orthonormal), it holds that

$$\hat{\boldsymbol{M}}_{HH,o} = \boldsymbol{T}_{HH,o}^T \boldsymbol{M} \boldsymbol{T}_{HH,o} = \begin{bmatrix} \boldsymbol{I} & \boldsymbol{0} \\ \boldsymbol{0} & {\boldsymbol{X}_o}^T \boldsymbol{M} \boldsymbol{X}_o \end{bmatrix} \tag{B.75}$$

and

$$\hat{\boldsymbol{K}}_{HH,o} = \boldsymbol{T}_{HH,o}^T \boldsymbol{K} \boldsymbol{T}_{HH,o} = \begin{bmatrix} \mathrm{diag}(\omega_k^2) & \boldsymbol{0} \\ \boldsymbol{0} & {\boldsymbol{X}_o}^T \boldsymbol{K} \boldsymbol{X}_o \end{bmatrix}, \tag{B.76}$$

Equation (B.73) is rewritten to

$$\boldsymbol{T}_{HH,o}^T \boldsymbol{Y}^{-1}(\omega j) \boldsymbol{T}_{HH,o} = \begin{bmatrix} \mathrm{diag}(\omega_k^2) & \boldsymbol{0} \\ \boldsymbol{0} & {\boldsymbol{X}_o}^T \boldsymbol{K} \boldsymbol{X}_o \end{bmatrix} - \omega^2 \begin{bmatrix} \boldsymbol{I} & \boldsymbol{0} \\ \boldsymbol{0} & {\boldsymbol{X}_o}^T \boldsymbol{M} \boldsymbol{X}_o \end{bmatrix}. \tag{B.77}$$

Inverting the whole relationship and using $\mathrm{diag}(\omega_k^2) = \boldsymbol{\Omega}_k^2$, we obtain

$$\boldsymbol{T}_{HH,o}^{-1} \boldsymbol{Y}(\omega j) \boldsymbol{T}_{HH,o}^{-T} = \left(\begin{bmatrix} \boldsymbol{\Omega}_k^2 & \boldsymbol{0} \\ \boldsymbol{0} & {\boldsymbol{X}_o}^T \boldsymbol{K} \boldsymbol{X}_o \end{bmatrix} - \omega^2 \begin{bmatrix} \boldsymbol{I} & \boldsymbol{0} \\ \boldsymbol{0} & {\boldsymbol{X}_o}^T \boldsymbol{M} \boldsymbol{X}_o \end{bmatrix} \right)^{-1} \tag{B.78}$$

$$= \begin{bmatrix} \left(\boldsymbol{\Omega}_k^2 - \omega^2 \boldsymbol{I}\right)^{-1} & \boldsymbol{0} \\ \boldsymbol{0} & \left({\boldsymbol{X}_o}^T \boldsymbol{K} \boldsymbol{X}_o - \omega^2 {\boldsymbol{X}_o}^T \boldsymbol{M} \boldsymbol{X}_o\right)^{-1} \end{bmatrix}. \tag{B.79}$$

Now, by pre-multiplication with $\boldsymbol{T}_{HH,o}$ and post-multiplication with $\boldsymbol{T}_{HH,o}^T$, we obtain:

$$\hat{\boldsymbol{Y}}_{HH}(\omega j) = \begin{bmatrix} \boldsymbol{\Phi}_{\mathcal{K}} & \boldsymbol{X}_o \end{bmatrix} \begin{bmatrix} \left(\boldsymbol{\Omega}_k^2 - \omega^2 \boldsymbol{I}\right)^{-1} & \boldsymbol{0} \\ \boldsymbol{0} & \left({\boldsymbol{X}_o}^T \boldsymbol{K} \boldsymbol{X}_o - \omega^2 {\boldsymbol{X}_o}^T \boldsymbol{M} \boldsymbol{X}_o\right)^{-1} \end{bmatrix} \begin{bmatrix} \boldsymbol{\Phi}_{\mathcal{K}}^T \\ \boldsymbol{X}_o^T \end{bmatrix} \tag{B.80}$$

$$= \begin{bmatrix} \boldsymbol{\Phi}_{\mathcal{K}} \left(\boldsymbol{\Omega}_k^2 - \omega^2 \boldsymbol{I}\right)^{-1} & \boldsymbol{\Phi}_{\mathcal{K}} \left({\boldsymbol{X}_o}^T \boldsymbol{K} \boldsymbol{X}_o - \omega^2 {\boldsymbol{X}_o}^T \boldsymbol{M} \boldsymbol{X}_o\right)^{-1} \end{bmatrix} \begin{bmatrix} \boldsymbol{\Phi}_{\mathcal{K}}^T \\ \boldsymbol{X}_o^T \end{bmatrix} \tag{B.81}$$

$$= \boldsymbol{\Phi}_{\mathcal{K}} \left(\boldsymbol{\Omega}_k^2 - \omega^2 \boldsymbol{I}\right)^{-1} \boldsymbol{\Phi}_{\mathcal{K}}^T + \boldsymbol{X}_o \left({\boldsymbol{X}_o}^T \boldsymbol{K} \boldsymbol{X}_o - \omega^2 {\boldsymbol{X}_o}^T \boldsymbol{M} \boldsymbol{X}_o\right)^{-1} \boldsymbol{X}_o^T. \tag{B.82}$$

Since, according to de Kraker [20],

$$\hat{\boldsymbol{Y}}_{MT}(\omega j) = \boldsymbol{\Phi}_{\mathcal{K}} \left(\boldsymbol{\Omega}_k^2 - \omega^2 \boldsymbol{I}\right)^{-1} \boldsymbol{\Phi}_{\mathcal{K}}^T = \sum_{k \in \mathcal{K}} \frac{\boldsymbol{\phi}_k \boldsymbol{\phi}_k^T}{\omega_k^2 - \omega^2}, \tag{B.83}$$

Equation (B.82) is written as

$$\hat{\boldsymbol{Y}}_{HH}(\omega j) = \sum_{k \in \mathcal{K}} \frac{\boldsymbol{\phi}_k \boldsymbol{\phi}_k^T}{\omega_k^2 - \omega^2} + \boldsymbol{X}_o \left({\boldsymbol{X}_o}^T \boldsymbol{K} \boldsymbol{X}_o - \omega^2 {\boldsymbol{X}_o}^T \boldsymbol{M} \boldsymbol{X}_o\right)^{-1} \boldsymbol{X}_o^T \tag{B.84}$$

$$= \sum_{k \in \mathcal{K}} \frac{\boldsymbol{\phi}_k \boldsymbol{\phi}_k^T}{\omega_k^2 - \omega^2} + \boldsymbol{X}_o \left(\hat{\boldsymbol{K}}_{\boldsymbol{X}_o} - \omega^2 \hat{\boldsymbol{M}}_{\boldsymbol{X}_o}\right)^{-1} \boldsymbol{X}_o^T. \tag{B.85}$$

Although for this derivation an undamped system is regarded, this also holds for damped systems. In this case, the reduced receptance is given by

$$\hat{\boldsymbol{Y}}_{HH}(\omega j) = \sum_{k\in\mathcal{K}} \frac{\boldsymbol{\phi}_k \boldsymbol{\phi}_k^T}{\omega_k^2 - 2j\xi_k\omega_k\omega - \omega^2} + \boldsymbol{X}_o \left(\hat{\boldsymbol{K}}_{\boldsymbol{X}_o} + \omega j \hat{\boldsymbol{D}}_{\boldsymbol{X}_o} - \omega^2 \hat{\boldsymbol{M}}_{\boldsymbol{X}_o}\right)^{-1} \boldsymbol{X}_o^T, \tag{B.86}$$

instead of Equation (B.85).

Note that this procedure holds for any reduction matrix where the first part contains the free-boundary eigenmodes and the second part ($\boldsymbol{X}_o$) is orthogonal to these eigenmodes.

B.5 Derivation of error contributors expression

As mentioned in Section 4.2.1, the LM FBS expression for the unreduced receptance of an assembly $\boldsymbol{Y}^{(assy)}$ is given by

$$\boldsymbol{Y}^{(assy)} = \boldsymbol{Y} - \underbrace{\underbrace{\boldsymbol{Y}\boldsymbol{B}_f^T \underbrace{(\boldsymbol{B}_f \boldsymbol{Y} \boldsymbol{B}_f^T)^{-1}}_{\boldsymbol{W}_1} \underbrace{\boldsymbol{B}_f \boldsymbol{Y}}_{\boldsymbol{W}_2}}_{\boldsymbol{W}_3}}, \tag{B.87}$$

where (parts of) the right-hand side are defined as $\boldsymbol{W}_1$, $\boldsymbol{W}_2$, and $\boldsymbol{W}_3$ which are used throughout this derivation. Since the boolean matrix $\boldsymbol{B}_f$ is not affected by the reduction, the reduced variant hereof is simply defined as

$$\hat{\boldsymbol{Y}}^{(assy)} = \hat{\boldsymbol{Y}} - \underbrace{\underbrace{\hat{\boldsymbol{Y}}\boldsymbol{B}_f^T \underbrace{(\boldsymbol{B}_f \hat{\boldsymbol{Y}} \boldsymbol{B}_f^T)^{-1}}_{\hat{\boldsymbol{W}}_1} \underbrace{\boldsymbol{B}_f \hat{\boldsymbol{Y}}}_{\hat{\boldsymbol{W}}_2}}_{\hat{\boldsymbol{W}}_3}}. \tag{B.88}$$

The reduction error of the assembly, $\boldsymbol{E}_Y^{(assy)} = \boldsymbol{Y}^{(assy)} - \hat{\boldsymbol{Y}}^{(assy)}$, is now written in terms of $\boldsymbol{E}_Y = \boldsymbol{Y} - \hat{\boldsymbol{Y}}$ and the reduction error of $\boldsymbol{W}_3$ ($\boldsymbol{E}_{W_3} = \boldsymbol{W}_3 - \hat{\boldsymbol{W}}_3$):

$$\begin{aligned} \boldsymbol{E}_Y^{(assy)} &= \boldsymbol{Y} - \hat{\boldsymbol{Y}} - \boldsymbol{Y}\boldsymbol{B}_f^T(\boldsymbol{B}_f\boldsymbol{Y}\boldsymbol{B}_f^T)^{-1}\boldsymbol{B}_f\boldsymbol{Y} + \hat{\boldsymbol{Y}}\boldsymbol{B}_f^T(\boldsymbol{B}_f\hat{\boldsymbol{Y}}\boldsymbol{B}_f^T)^{-1}\boldsymbol{B}_f\hat{\boldsymbol{Y}} && \text{(B.89)} \\ &= \boldsymbol{E}_Y - \boldsymbol{E}_{W_3}. && \text{(B.90)} \end{aligned}$$

Since $\boldsymbol{W}_3 = \boldsymbol{Y}\boldsymbol{B}_f^T\boldsymbol{W}_2$, the reduction error of $\boldsymbol{W}_3$ is written as

$$\boldsymbol{E}_{W_3} = \boldsymbol{Y}\boldsymbol{B}_f^T\boldsymbol{W}_2 - \hat{\boldsymbol{Y}}\boldsymbol{B}_f^T\hat{\boldsymbol{W}}_2. \tag{B.91}$$

By using a small trick, similar to that used in the derivation for the small gain error bound (which is described in Appendix C.2.3), this error can be split in a term related to the error in $\boldsymbol{Y}$ and a term related to the error in $\boldsymbol{W}_2$:

$$\begin{aligned} \boldsymbol{E}_{W_3} &= \boldsymbol{Y}\boldsymbol{B}_f^T\boldsymbol{W}_2 - \hat{\boldsymbol{Y}}\boldsymbol{B}_f^T\boldsymbol{W}_2 + \hat{\boldsymbol{Y}}\boldsymbol{B}_f^T\boldsymbol{W}_2 - \hat{\boldsymbol{Y}}\boldsymbol{B}_f^T\hat{\boldsymbol{W}}_2 && \text{(B.92)} \\ &= \boldsymbol{E}_Y\boldsymbol{B}_f^T\boldsymbol{W}_2 + \hat{\boldsymbol{Y}}\boldsymbol{B}_f^T\boldsymbol{E}_{W_2}. && \text{(B.93)} \end{aligned}$$

Now, similar steps can be taken to determine $\boldsymbol{E}_{W_2}$. For this, we use that $\boldsymbol{W}_2 = \left(\boldsymbol{B}_f \boldsymbol{Y} \boldsymbol{B}_f^T\right)^{-1} \boldsymbol{W}_1$:

$$\begin{aligned}
\boldsymbol{E}_{W_2} &= \boldsymbol{W}_2 - \hat{\boldsymbol{W}}_2 && \text{(B.94)}\\
&= \left(\boldsymbol{B}_f \boldsymbol{Y} \boldsymbol{B}_f^T\right)^{-1} \boldsymbol{W}_1 - \left(\boldsymbol{B}_f \hat{\boldsymbol{Y}} \boldsymbol{B}_f^T\right)^{-1} \hat{\boldsymbol{W}}_1 && \text{(B.95)}\\
&= \left(\boldsymbol{B}_f \boldsymbol{Y} \boldsymbol{B}_f^T\right)^{-1} \boldsymbol{W}_1 - \left(\boldsymbol{B}_f \hat{\boldsymbol{Y}} \boldsymbol{B}_f^T\right)^{-1} \boldsymbol{W}_1 + \left(\boldsymbol{B}_f \hat{\boldsymbol{Y}} \boldsymbol{B}_f^T\right)^{-1} \boldsymbol{W}_1 - \left(\boldsymbol{B}_f \hat{\boldsymbol{Y}} \boldsymbol{B}_f^T\right)^{-1} \hat{\boldsymbol{W}}_1 && \text{(B.96)}\\
&= \underbrace{\left(\left(\boldsymbol{B}_f \boldsymbol{Y} \boldsymbol{B}_f^T\right)^{-1} - \left(\boldsymbol{B}_f \hat{\boldsymbol{Y}} \boldsymbol{B}_f^T\right)^{-1}\right)}_{\boldsymbol{E}_{BYB^T}} \boldsymbol{W}_1 + \left(\boldsymbol{B}_f \hat{\boldsymbol{Y}} \boldsymbol{B}_f^T\right)^{-1} \boldsymbol{E}_{W_1}. && \text{(B.97)}
\end{aligned}$$

Finally, $\boldsymbol{E}_{W_1}$ is given by

$$\begin{aligned}
\boldsymbol{E}_{W_1} &= \boldsymbol{B}_f \boldsymbol{Y} - \hat{\boldsymbol{B}} \hat{\boldsymbol{Y}} && \text{(B.98)}\\
&= \boldsymbol{B}_f \boldsymbol{E}_Y. && \text{(B.99)}
\end{aligned}$$

Substitution of Equations (B.93), (B.97), and (B.99) in Equation (B.90) gives an expression for the total error:

$$\begin{aligned}
\boldsymbol{E}_Y^{(assy)} =& \boldsymbol{E}_Y - \boldsymbol{E}_Y \boldsymbol{B}_f^T \left(\boldsymbol{B}_f \boldsymbol{Y} \boldsymbol{B}_f^T\right)^{-1} \boldsymbol{B}_f \boldsymbol{Y} - \hat{\boldsymbol{Y}} \boldsymbol{B}_f^T \boldsymbol{E}_{BYB^T} \boldsymbol{B}_f \boldsymbol{Y} \ldots \\
&- \hat{\boldsymbol{Y}} \boldsymbol{B}_f^T \left(\boldsymbol{B}_f \hat{\boldsymbol{Y}} \boldsymbol{B}_f^T\right)^{-1} \boldsymbol{B}_f \boldsymbol{E}_Y.
\end{aligned} \tag{B.100}$$

Using the fact that the signed boolean matrix $\boldsymbol{B}_f$ selects partitions of the receptance matrix related to the interface DOFs, Equation (B.100) is written as

$$\boldsymbol{E}_{Y,bb}^{(assy)} = \underbrace{\boldsymbol{E}_{Y,bb}}_{\bar{\boldsymbol{E}}_{bb}} \underbrace{- \boldsymbol{E}_{Y,bf} \boldsymbol{Y}_{ff}^{-1} \boldsymbol{Y}_{fb}}_{\bar{\boldsymbol{E}}_{bf}} \underbrace{- \hat{\boldsymbol{Y}}_{bf} \overbrace{\left(\boldsymbol{Y}_{ff}^{-1} - \hat{\boldsymbol{Y}}_{ff}^{-1}\right)}^{\boldsymbol{E}_{BYB^T}} \boldsymbol{Y}_{fb}}_{\bar{\boldsymbol{E}}_{ff}} \underbrace{- \hat{\boldsymbol{Y}}_{bf} \hat{\boldsymbol{Y}}_{ff}^{-1} \boldsymbol{E}_{Y,fb}}_{\bar{\boldsymbol{E}}_{fb}}. \tag{B.101}$$

Here, specific (interface DOF and boundary DOF related) partitions of the receptance matrices are used. Since, in a CMS context, static behavior is only exact at the boundary degrees of freedom, only these DOFs are of interest. Therefore, only the boundary related partition of the receptances and error matrices are used. As a result, $\boldsymbol{Y}_{bf}$ represents the partition of the receptance matrix with the transfer functions from interface DOFs to boundary DOFs. Furthermore, this equation introduces the error contributors. Here, the subscript of each error contributor indicates which error is propagated for this specific contributor. For example, $\bar{\boldsymbol{E}}_{bf}$ denotes the propagated error (matrix) of the transfers going from the interface DOFs to the boundary DOFs.

B.6 Proof for comparison of simultaneous and individual truncation of modes

In this section, a proof is given for Equations (5.3) and (5.4), which compare the approximated assembly error and frequency-dependent error measure thereof, respectively, if two modes are either individually or simultaneously truncated. For brevity, the explicit frequency-dependence is omitted from the equations given in this appendix.

B.6.1 Approximated assembly error

Using Equation (4.23) for the approximated assembly error, the approximated assembly errors if modes $\boldsymbol{\phi}_2^{(1)}$ and $\boldsymbol{\phi}_2^{(1)}$ are omitted individually or a selection of two modes $\boldsymbol{\phi}_{k_1}^{(c)} + \boldsymbol{\phi}_{k_2}^{(c)}$ is omitted simultaneously from the component reduction bases are shown in Equations (B.102), (B.103) and (B.104), respectively:

$$\boldsymbol{\Delta Y}^{(assy)}_{\boldsymbol{\phi}_1^{(1)}} = \sum_k^{n_b^{(assy)}} \sum_l^{n_b^{(assy)}} \frac{\partial \boldsymbol{Y}^{(assy)}}{\partial \boldsymbol{Y}[k,l]} \boldsymbol{\Delta Y}_{\boldsymbol{\phi}_1^{(1)}}[k,l], \tag{B.102}$$

$$\boldsymbol{\Delta Y}^{(assy)}_{\boldsymbol{\phi}_2^{(1)}} = \sum_k^{n_b^{(assy)}} \sum_l^{n_b^{(assy)}} \frac{\partial \boldsymbol{Y}^{(assy)}}{\partial \boldsymbol{Y}[k,l]} \boldsymbol{\Delta Y}_{\boldsymbol{\phi}_2^{(1)}}[k,l], \tag{B.103}$$

$$\boldsymbol{\Delta Y}^{(assy)}_{\boldsymbol{\phi}_1^{(1)}+\boldsymbol{\phi}_2^{(1)}} = \sum_k^{n_b^{(assy)}} \sum_l^{n_b^{(assy)}} \frac{\partial \boldsymbol{Y}^{(assy)}}{\partial \boldsymbol{Y}[k,l]} \boldsymbol{\Delta Y}_{\boldsymbol{\phi}_1^{(1)}+\boldsymbol{\phi}_2^{(1)}}[k,l]. \tag{B.104}$$

Here, the subscript $\boldsymbol{\phi}_1^{(1)} + \boldsymbol{\phi}_2^{(1)}$ denotes the situation where both modes $\boldsymbol{\phi}_1^{(1)}$ and $\boldsymbol{\phi}_2^{(1)}$ are omitted from the reduction bases simultaneously. Now, since according to Equation (4.35), for the error of a specific component, it holds that

$$\boldsymbol{\Delta Y}^{(c)}_{\boldsymbol{\phi}_1^{(1)}+\boldsymbol{\phi}_2^{(1)}} = \boldsymbol{\Delta Y}^{(c)}_{\boldsymbol{\phi}_1^{(1)}} + \boldsymbol{\Delta Y}^{(c)}_{\boldsymbol{\phi}_2^{(1)}}, \tag{B.105}$$

Equation (B.104) can be written as

$$\begin{aligned} \boldsymbol{\Delta Y}^{(assy)}_{\boldsymbol{\phi}_1^{(1)}+\boldsymbol{\phi}_2^{(1)}} &= \sum_k^{n_b^{(assy)}} \sum_l^{n_b^{(assy)}} \left(\frac{\partial \boldsymbol{Y}^{(assy)}}{\partial \boldsymbol{Y}[k,l]} \left(\boldsymbol{\Delta Y}_{\boldsymbol{\phi}_1^{(1)}}[k,l] + \boldsymbol{\Delta Y}_{\boldsymbol{\phi}_2^{(1)}}[k,l] \right) \right) \\ &= \boldsymbol{\Delta Y}^{(assy)}_{\boldsymbol{\phi}_1^{(1)}} + \boldsymbol{\Delta Y}^{(assy)}_{\boldsymbol{\phi}_2^{(1)}}. \end{aligned} \tag{B.106}$$

Here, it is thus shown that the approximated error caused by simultaneously leaving out multiple component modes from the reduction bases equals the sum of the approximated errors if these modes are left out individually. Remember that this only holds for the approximated assembly error or if a modal truncation reduction technique is used. As is proven in Section B.6.2, this does not hold anymore if these MIMO errors are condensed to a scalar (frequency-dependent) measure $\epsilon^{(assy)}$ by using spatial norms.

B.6.2 Frequency-dependent error measure

In this section it is investigated if

$$\epsilon^{(assy)}_{\boldsymbol{\phi}_1^{(1)}+\boldsymbol{\phi}_2^{(1)}} \stackrel{?}{=} \epsilon^{(assy)}_{\boldsymbol{\phi}_1^{(1)}} + \epsilon^{(assy)}_{\boldsymbol{\phi}_2^{(1)}}. \tag{B.107}$$

Since the definition of $\epsilon^{(assy)}$ is given by Equation (5.1), Equation (B.107) is written as

$$\frac{\left\| \boldsymbol{\Delta Y}^{(assy)}_{\boldsymbol{\phi}_1^{(1)}+\boldsymbol{\phi}_2^{(1)}} \right\|_F}{\left\| \boldsymbol{Y}^{(assy)} \right\|_F} \stackrel{?}{=} \frac{\left\| \boldsymbol{\Delta Y}^{(assy)}_{\boldsymbol{\phi}_1^{(1)}} \right\|_F}{\left\| \boldsymbol{Y}^{(assy)} \right\|_F} + \frac{\left\| \boldsymbol{\Delta Y}^{(assy)}_{\boldsymbol{\phi}_2^{(1)}} \right\|_F}{\left\| \boldsymbol{Y}^{(assy)} \right\|_F}, \tag{B.108}$$

where the denominators at both sides of the equation can be eliminated:

$$\left\| \boldsymbol{\Delta Y}^{(assy)}_{\boldsymbol{\phi}_1^{(1)}+\boldsymbol{\phi}_2^{(1)}} \right\|_F \stackrel{?}{=} \left\| \boldsymbol{\Delta Y}^{(assy)}_{\boldsymbol{\phi}_1^{(1)}} \right\|_F + \left\| \boldsymbol{\Delta Y}^{(assy)}_{\boldsymbol{\phi}_2^{(1)}} \right\|_F . \tag{B.109}$$

Focusing on the left part, we can write:

$$\left\| \boldsymbol{\Delta Y}^{(assy)}_{\boldsymbol{\phi}_1^{(1)}+\boldsymbol{\phi}_2^{(1)}} \right\|_F = \left\| \sum_k^{n_b^{(assy)}} \sum_l^{n_b^{(assy)}} \frac{\partial \boldsymbol{Y}^{(assy)}}{\partial \boldsymbol{Y}[k,l]} \boldsymbol{\Delta Y}_{\boldsymbol{\phi}_1^{(1)}+\boldsymbol{\phi}_2^{(1)}}[k,l] \right\|_F \tag{B.110}$$

$$= \left\| \sum_k^{n_b^{(assy)}} \sum_l^{n_b^{(assy)}} \frac{\partial \boldsymbol{Y}^{(assy)}}{\partial \boldsymbol{Y}[k,l]} \left(\boldsymbol{\Delta Y}_{\boldsymbol{\phi}_1^{(1)}}[k,l] + \boldsymbol{\Delta Y}_{\boldsymbol{\phi}_2^{(1)}}[k,l] \right) \right\|_F \tag{B.111}$$

$$= \left\| \sum_k^{n_b^{(assy)}} \sum_l^{n_b^{(assy)}} \frac{\partial \boldsymbol{Y}^{(assy)}}{\partial \boldsymbol{Y}[k,l]} \left(\boldsymbol{\Delta Y}_{\boldsymbol{\phi}_1^{(1)}}[k,l] \right) + \sum_k^{n_b^{(assy)}} \sum_l^{n_b^{(assy)}} \frac{\partial \boldsymbol{Y}^{(assy)}}{\partial \boldsymbol{Y}[k,l]} \left(\boldsymbol{\Delta Y}_{\boldsymbol{\phi}_2^{(1)}}[k,l] \right) \right\|_F \tag{B.112}$$

$$\begin{aligned} \leq & \left\| \sum_k^{n_b^{(assy)}} \sum_l^{n_b^{(assy)}} \frac{\partial \boldsymbol{Y}^{(assy)}}{\partial \boldsymbol{Y}[k,l]} \left(\boldsymbol{\Delta Y}_{\boldsymbol{\phi}_1^{(1)}}[k,l] \right) \right\|_F + \dots \\ & + \left\| \sum_k^{n_b^{(assy)}} \sum_l^{n_b^{(assy)}} \frac{\partial \boldsymbol{Y}^{(assy)}}{\partial \boldsymbol{Y}[k,l]} \left(\boldsymbol{\Delta Y}_{\boldsymbol{\phi}_2^{(1)}}[k,l] \right) \right\|_F \end{aligned} . \tag{B.113}$$

Where, in order to obtain Equation (B.111), it was used that, according to Equation (B.105), the component error due to deleting two eigenmodes is equal to the sum of the component errors where the eigenmodes are deleted individually (for a MT reduction basis). Furthermore, Equation (B.113) follows from the triangle inequality. Based on Equation (B.113), we can thus write

$$\epsilon^{(assy)}_{\boldsymbol{\phi}_1^{(1)}+\boldsymbol{\phi}_2^{(1)}} \leq \epsilon^{(assy)}_{\boldsymbol{\phi}_1^{(1)}} + \epsilon^{(assy)}_{\boldsymbol{\phi}_2^{(1)}}, \tag{B.114}$$

indicating that the equalilty sign in Equation (B.107) should actually be an inequality sign instead. Note that, although here the error due to deleting two component modes is calculated, the findings given above hold for any combination of any number of truncated modes.

Appendix C

Mathematical background

In this appendix, some mathematical background are provided. First, some basic notions with respect to vector and matrix norms are given. Afterwards, a few mathematical operations used for, for example, the derivation of the small gain condition and error bound are given. Finally, scaling of inputs, outputs, and transfer functions is discussed.

C.1 Norms

Here, some standard definitions for vector/matrix norms are given, as these are used throughout this thesis.

C.1.1 Vector norm

Suppose $\boldsymbol{x} \in \mathbb{C}^{n\times 1}$, then, its p-norm is defined as

$$\|\boldsymbol{x}\|_p = \left(\sum_{i=1}^{n} |x_i|^p\right)^{1/p}. \tag{C.1}$$

As can be seen, for $p = 1$ this norm simply gives the sum of the absolute values of all entries in the vector. The norm when $p = 2$ is given by the square root of the summed squares of all entries in $\boldsymbol{x}$ and is often related to energy. The case where $p = \infty$ is somewhat more difficult to understand from Equation (C.1), but simply comes down to

$$\|\boldsymbol{x}\|_\infty = \sup_i |x_i|, \tag{C.2}$$

and thus gives the largest absolute entry in $\boldsymbol{x}$.

C.1.2 Induced matrix norm

The induced matrix norm is a measure for the amplification of vectors on the unit sphere (with dimension n), caused by $\boldsymbol{A} \in \mathbb{C}^{m\times n}$. The matrix norm thus gives a kind of gain of a matrix [7]. The formal definition of the induced norm of a matrix is given by

$$\|\boldsymbol{A}\|_p = \max_{\|\boldsymbol{x}\|_p=1} \|\boldsymbol{A}\boldsymbol{x}\|_p. \tag{C.3}$$

An important property of the matrix norm, which is exploited in thesis, is the submultiplicative property:

$$\|\boldsymbol{AB}\|_p \leq \|\boldsymbol{A}\|_p \|\boldsymbol{B}\|_p. \tag{C.4}$$

In case $p = 2$, the induced 2-norm can be calculated is by using the singular values of $\boldsymbol{A}$, the 2-norm is namely given by the maximal singular value σ_{max} (as also mentioned in Appendix B.1):

$$\|\boldsymbol{A}\|_2 = \sigma_{max}(\boldsymbol{A}). \tag{C.5}$$

C.1.3 Frobenius norm

A different type of matrix norm is the Frobenius norm, which is a type of "entrywise" norm [31]. This matrix norm does not give a kind of matrix gain, but uses all elements of the matrix. Suppose $\boldsymbol{A} \in \mathbb{C}^{m \times n}$, then the Frobenius norm is given by

$$\|\boldsymbol{A}\|_F = \sqrt{\sum_{i=1}^{m}\sum_{j=1}^{n} |A_{ij}|^2} = \sqrt{\text{trace}\,(\boldsymbol{A}^*\boldsymbol{A})} = \sqrt{\sum_{i=1}^{\min(m,n)} \sigma_i^2(\boldsymbol{A})}, \tag{C.6}$$

where $\boldsymbol{A}^*$ is the complex conjugate of $\boldsymbol{A}$ and $\sigma_i(\boldsymbol{A})$ denotes the i^{th} singular value of $\boldsymbol{A}$. As proven by Ford [10], both the triangle inequality and submultiplicative property hold for this type of norm.

C.1.4 Comparison of matrix norms

Here, a short comparison between the Frobenius norm and induced 2-norm is given. As is explained in the section above, the Frobenius norm is given by the square root of the squares of all singular values (Equation (C.6), and the induced-2 norm by the maximal singular value (Equation (C.5)). Therefore we can write that

$$\|\boldsymbol{A}\|_F = \sqrt{\sum_{i=1}^{\min(m,n)} \sigma_i^2(\boldsymbol{A})} \geq \sigma_{max}(\boldsymbol{A}) = \|\boldsymbol{A}\|_2. \tag{C.7}$$

Furthermore, if the singular values of $\boldsymbol{A}$ are relatively separated, the contribution of the highest singular value will dominate the Frobenius norm, due to the square in Equation (C.6). Because of this, the Frobenius norm is approximately equal to the induced 2-norm if the first singular value is relatively large with respect to the second singular value.

C.2 Mathematical operations

Here, some mathematical steps/operations which are used in the derivation of the small gain error bound (Section B.2) are explained in more detail.

C.2.1 Triangle inequality

Given a variable $\boldsymbol{z}$ which is given by

$$\boldsymbol{z} = \boldsymbol{x} + \boldsymbol{y}, \tag{C.8}$$

and taking the p-norm of both sides of this equation gives

$$\|\boldsymbol{z}\|_p = \|\boldsymbol{x} + \boldsymbol{y}\|_p. \tag{C.9}$$

In case the norm of $\boldsymbol{z}$ has to be expressed in terms of the individual norms of $\boldsymbol{x}$ and $\boldsymbol{y}$, Equation (C.9) may be written as

$$\|\boldsymbol{z}\|_p \leq \|\boldsymbol{x}\|_p + \|\boldsymbol{y}\|_p. \tag{C.10}$$

Here, Minkowski's inequality (Equation (C.11) [24]) is used. This inequality is often also referred to as the triangle inequality, since it denotes that the sum of the lengths of two vectors is always greater or equal to the length of the sum of these vectors. In other words; the shortest distance between two points on a triangle is the edge connecting them directly, not the sum of the other two edges.

$$\|\boldsymbol{z}\|_p = \|\boldsymbol{x} + \boldsymbol{y}\|_p \leq \|\boldsymbol{x}\|_p + \|\boldsymbol{y}\|_p, \qquad 1 \leq p \leq \infty \tag{C.11}$$

Note that, according to Minkowski, Equations (C.10) and (C.11) only hold for $1 \leq p \leq \infty$. Since, typically, p-norms are defined in this specific range, this explicit condition is not repeated in the rest of this thesis. Note that the triangle inequality also holds for matrix norms.

C.2.2 Boundedness by $\mathcal{H}_\infty$-norm

Suppose some transfer function $\boldsymbol{H}_{yx}$ is given which returns, for a given input-variable $\boldsymbol{x}$, the variable $\boldsymbol{y}$ (where, as an optional intermediate step, the variable $\boldsymbol{y}$ is expressed as a function G_y):

$$\boldsymbol{y}(s) = G_y(\boldsymbol{x}(\boldsymbol{s})) = \boldsymbol{H}_{yx}(s)\boldsymbol{x}(s). \tag{C.12}$$

Then, it can be stated that the maximal value for the $\mathcal{L}_2$-norm of $\boldsymbol{y}$ for some $\mathcal{L}_2$-norm of $\boldsymbol{x}$, is upper bounded by the $\mathcal{H}_\infty$-norm of the transfer function matrix relating $\boldsymbol{x}$ and $\boldsymbol{y}$. Here, the $\mathcal{L}_2$-norm of the time signal is, by Parseval's theorem, linked to the energy equivalent in the frequency-domain. The fact that the $\mathcal{L}_2$ norm of $\boldsymbol{Y}$ is upper bounded by the $\mathcal{H}_\infty$-norm is based on the fact that the $\mathcal{H}_\infty$-norm gives the maximal 'gain' of the transfer function, and thus denotes the highest amplification possible from $\|\boldsymbol{x}\|_2$ to $\|\boldsymbol{y}\|_2$. The $\mathcal{H}_\infty$-norm thus gives an upper bound on a transfer function (matrix) and is substituted by a constant scalar γ_{yx}:

$$\|\boldsymbol{y}\|_2 \leq \|\boldsymbol{H}_{yx}(s)\|_\infty \|\boldsymbol{x}\|_2 = \gamma_{yx}\|\boldsymbol{x}\|_2. \tag{C.13}$$

Here, γ_{yx} is calculated by using the highest singular value (σ_{max}) and finding the maximum hereof over the frequency [28]:

$$\gamma = \|\boldsymbol{H}(s)\|_\infty = \sup_\omega \sigma_{max}\left(\boldsymbol{H}(\omega j)\right). \tag{C.14}$$

For a SISO system, the $\mathcal{H}_\infty$-norm simply gives the amplitude of the highest peak of the transfer function.

C.2.3 Splitting of norms

Given an expression of a variable $\boldsymbol{\delta i} = \boldsymbol{i} - \hat{\boldsymbol{i}}$, which represents the error and can be described in function form as

$$\boldsymbol{\delta i} = G_i(\boldsymbol{k}) - \hat{G}_i(\hat{\boldsymbol{k}}), \tag{C.15}$$

the p-norm of the right hand side proves rather difficult to determine. The reason for this is that the term $\|G_i(\boldsymbol{k}) - \hat{G}_i(\hat{\boldsymbol{k}})\|_p$ can not be directly expressed by the individual norms on errors

of the relevant transfer functions and inputs which are known. Therefore, a mathematical 'trick' is used to obtain terms of which the norms are known. For this trick, the term $\hat{G}_i(\boldsymbol{k})$ is both added and subtracted from the right side of (C.15), which results in

$$\boldsymbol{\delta i} = G_i(\boldsymbol{k}) - \hat{G}_i(\boldsymbol{k}) + \hat{G}_i(\boldsymbol{k}) - \hat{G}_i(\hat{\boldsymbol{k}}). \tag{C.16}$$

As is obvious, due to the simultaneous addition and subtraction, the expression is mathematically equivalent to the original. The advantage of this trick is that it allows to split the p-norm of $\boldsymbol{\delta i}$ in a part related to the error introduced by using a reduced transfer $\hat{G}_i$, and a second part related to the error introduced by having a reduced input $\hat{\boldsymbol{k}}$, which are given by the first and second term in Equation (C.18), respectively. Note that, in order to obtain Equation (C.18), the triangle inequality as introduced in Appendix C.2.1 is used.

$$\begin{aligned} \|\boldsymbol{\delta i}\|_p &= \|G_i(\boldsymbol{k}) - \hat{G}_i(\boldsymbol{k}) + \hat{G}_i^{(1)}(\boldsymbol{k}) - \hat{G}_i(\hat{\boldsymbol{k}})\|_p && \text{(C.17)} \\ &\leq \|G_i(\boldsymbol{k}) - \hat{G}_i(\boldsymbol{k})\|_p + \|\hat{G}_i(\boldsymbol{k}) - \hat{G}_i(\hat{\boldsymbol{k}})\|_p && \text{(C.18)} \end{aligned}$$

C.3 Scaling

This section will explain the scaling which is implemented to scale receptance matrices for the calculation of the spatial norm in Section 5.1.1. The goal of the scaling is to make the receptance matrices dimensionless and (roughly) of the same order of magnitude. Below, the scaling procedure is explained.

Suppose we only look at the part of a receptance matrix $\boldsymbol{Y}$ related to the transfer from any degree of freedom of one node to any of the DOFs of this same node. Such a partition is a square matrix, with as many rows/columns as there are DOFs per node (so for the demonstrator 2). The in- and output are then given by

$$\boldsymbol{F} = \begin{bmatrix} F \\ M \end{bmatrix} \tag{C.19}$$

and

$$\boldsymbol{u} = \begin{bmatrix} u \\ \varphi \end{bmatrix}, \tag{C.20}$$

respectively, resulting in

$$\boldsymbol{u} = \boldsymbol{Y}\boldsymbol{F}. \tag{C.21}$$

Now, suppose the scaled system is indicated by a tilde. Equation (C.21) then becomes

$$\tilde{\boldsymbol{u}} = \tilde{\boldsymbol{Y}}\tilde{\boldsymbol{F}}, \tag{C.22}$$

where the scaled in- and output variables are defined as

$$\begin{aligned} \begin{bmatrix} \tilde{u} \\ \tilde{\varphi} \end{bmatrix} &= \begin{bmatrix} \frac{1}{u_{char}} u \\ \frac{1}{\varphi_{char}} \varphi \end{bmatrix} && \text{(C.23)} \\ &= \underbrace{\begin{bmatrix} \frac{1}{u_{char}} & 0 \\ 0 & \frac{1}{\varphi_{char}} \end{bmatrix}}_{\boldsymbol{S}_{out}} \begin{bmatrix} u \\ \varphi \end{bmatrix}, && \text{(C.24)} \end{aligned}$$

and

$$\begin{bmatrix} \tilde{F} \\ \tilde{M} \end{bmatrix} = \begin{bmatrix} \frac{1}{F_{char}} F \\ \frac{1}{M_{char}} M \end{bmatrix} \tag{C.25}$$

$$= \underbrace{\begin{bmatrix} \frac{1}{F_{char}} & 0 \\ 0 & \frac{1}{M_{char}} \end{bmatrix}}_{\boldsymbol{S}_{in}} \begin{bmatrix} F \\ M \end{bmatrix}. \tag{C.26}$$

Here, u_{char}, F_{char}, and M_{char} represent constant characteristic values, which are used to make the system dimensionless.

The relations given in Equations (C.23)-(C.26) can also be given as

$$\tilde{\boldsymbol{u}} = \boldsymbol{S}_{out} \boldsymbol{u} \tag{C.27}$$

and

$$\tilde{\boldsymbol{F}} = \boldsymbol{S}_{in} \boldsymbol{F} \tag{C.28}$$

$$\implies \boldsymbol{F} = \boldsymbol{S}_{in}^{-1} \tilde{\boldsymbol{F}}. \tag{C.29}$$

Using Equations (C.27) and (C.29) in Equation (C.21) gives

$$\tilde{\boldsymbol{u}} = \underbrace{\boldsymbol{S}_{out} \boldsymbol{Y} \boldsymbol{S}_{in}^{-1}}_{\tilde{\boldsymbol{Y}}} \tilde{\boldsymbol{F}}, \tag{C.30}$$

where a definition for the scaled receptance matrix is given. Note here that, due to the diagonal nature of $\boldsymbol{S}_{in}$, the inverse is simply defined as a diagonal matrix with the inverses of the original scalar entries along the diagonal.

The units of the variables corresponding to the variables in Equation (C.30) are

$$\begin{bmatrix} [-] \\ [-] \end{bmatrix} = \underbrace{\begin{bmatrix} [\frac{1}{\mathrm{m}}] & [-] \\ [-] & [-] \end{bmatrix} \begin{bmatrix} [\frac{\mathrm{m}}{\mathrm{N}}] & [\frac{\mathrm{m}}{\mathrm{Nm}}] \\ [\frac{1}{\mathrm{N}}] & [\frac{1}{\mathrm{Nm}}] \end{bmatrix} \begin{bmatrix} [\mathrm{N}] & [-] \\ [-] & [\mathrm{Nm}] \end{bmatrix}}_{= \begin{bmatrix} [-] & [-] \\ [-] & [-] \end{bmatrix}} \begin{bmatrix} [-] \\ [-] \end{bmatrix}, \tag{C.31}$$

where the bracket notation denotes the units of the entries and "$[-]$" indicates that a variable is dimensionless. In this equation, it is shown that the units of the scaling matrices indeed make the scaled receptance matrix dimensionless.

By choosing characteristic values for the displacement, force, and moment, the individual receptances can be scaled. Since the dimension of M_{char} ([Nm]) consists out of the dimensions of u_{char} ([m]) and F_{char} ([N]) however, the system can be made properly dimensionless by only using a characteristic value for each distinct dimension, as discussed by Buckingham [4]. Therefore, the only characteristic values that really need to be chosen are u_{char} and F_{char}, where

$$M_{char} = u_{char} F_{char}. \tag{C.32}$$

Since the demonstrator cantilever beam (with the specified dimensions and material parameters) can be imagined to have a supporting function of, for example, a load hanging at the end, such an example is used to determine a characteristic length for a given characteristic force. For example, having a load of 20000 N ($\approx$ 2000 kg), would result in a maximal static deflection at the end of the beam of about 0.48 m (approximately 10 % of its total length) [11]. Although these are not the most realistic values for this example, this combination of u_{char} and F_{char} results in transfer function matrices for which the order of magnitude of the different elements are relatively comparable.

Appendix D

Code of conduct

On the following page, the declaration of the TU/e Code of Scientific Conduct for the Master thesis is included.

TU/e Technische Universiteit Eindhoven University of Technology

Declaration concerning the TU/e Code of Scientific Conduct for the Master's thesis

I have read the TU/e Code of Scientific Conduct[i].

I hereby declare that my Master's thesis has been carried out in accordance with the rules of the TU/e Code of Scientific Conduct

Date

11/11/2019

Name

Bas Kessels

ID-number

0893597

Signature

Submit the signed declaration to the student administration of your department.

[i] See: http://www.tue.nl/en/university/about-the-university/integrity/scientific-integrity/
The Netherlands Code of Conduct for Academic Practice of the VSNU can be found here also.
More information about scientific integrity is published on the websites of TU/e and VSNU

January 15 2016